



UNIVERSIDADE ESTADUAL DE CAMPINAS  
Instituto de Física “Gleb Wataghin”

LEONARDO DA SILVA GARCIA LEITE

## **Two-dimensional correlated Chern and topological insulators**

Isolantes topológico e de Chern correlacionados  
bidimensionais

Campinas  
2022

LEONARDO DA SILVA GARCIA LEITE

# **Two-dimensional correlated Chern and topological insulators**

Isolantes topológico e de Chern correlacionados  
bidimensionais

Thesis presented to the Institute of Physics “Gleb Wataghin” of the University of Campinas in partial fulfillment of the requirements for the degree of Doctor of Sciences, in the area of Physics.

Tese apresentada ao Instituto de Física “Gleb Wataghin” da Universidade Estadual de Campinas como parte dos requisitos exigidos para a obtenção do título de Doutor em Ciências, na área de Física.

Orientador: Prof. Dr. Ricardo Luís Doretto

ESTE EXEMPLAR CORRESPONDE À VERSÃO FINAL DA TESE DE DOUTORADO DEFENDIDA PELO ALUNO LEONARDO DA SILVA GARCIA LEITE E ORIENTADO PELO PROF. DR. RICARDO LUÍS DORETTO.

Campinas  
2022

Ficha catalográfica  
Universidade Estadual de Campinas  
Biblioteca do Instituto de Física Gleb Wataghin  
Lucimeire de Oliveira Silva da Rocha - CRB 8/9174

L536t Leite, Leonardo da Silva Garcia, 1987-  
Two-dimensional correlated Chern and topological insulators / Leonardo da Silva Garcia Leite. – Campinas, SP : [s.n.], 2022.

Orientador: Ricardo Luís Doretto.  
Tese (doutorado) – Universidade Estadual de Campinas, Instituto de Física Gleb Wataghin.

1. Sistemas eletrônicos fortemente correlacionados. 2. Isolantes topológicos. 3. Isolantes de Chern. 4. Modelo de Haldane-Hubbard. 5. Ferromagnetismo. I. Doretto, Ricardo Luís, 1976-. II. Universidade Estadual de Campinas. Instituto de Física Gleb Wataghin. III. Título.

Informações para Biblioteca Digital

**Título em outro idioma:** Isolantes topológico e de Chern correlacionados bidimensionais

**Palavras-chave em inglês:**

Strongly correlated electron systems

Topological insulators

Chern insulators

Haldane-Hubbard model

Ferromagnetism

**Área de concentração:** Física

**Titulação:** Doutor em Ciências

**Banca examinadora:**

Ricardo Luís Doretto [Orientador]

Eduardo Miranda

Amir Ordacgi Caldeira

Cristiane de Moraes Smith Lehner

George Balster Martins

**Data de defesa:** 29-04-2022

**Programa de Pós-Graduação:** Física

**Identificação e informações acadêmicas do(a) aluno(a)**

- ORCID do autor: <https://orcid.org/0000-0002-4611-9010>

- Currículo Lattes do autor: <http://lattes.cnpq.br/4033577031203954>



MEMBROS DA COMISSÃO JULGADORA DA TESE DE DOUTORADO DO ALUNO LEONARDO DA SILVA GARCIA LEITE - RA 180523 APRESENTADA E APROVADA AO INSTITUTO DE FÍSICA “GLEB WATAGHIN”, DA UNIVERSIDADE ESTADUAL DE CAMPINAS, EM 29/04/2022.

COMISSÃO JULGADORA:

- Prof. Dr. Ricardo Luís Doretto - Presidente e Orientador (IFGW/UNICAMP)
- Prof. Dr. Eduardo Miranda (IFGW/UNICAMP)
- Prof. Dr. Amir Ordacgi Caldeira (IFGW/UNICAMP)
- Dra. Cristiane de Moraes Smith Lehner (Utrecht University)
- Dr. George Balster Martins (Universidade Federal de Uberlândia)

**OBS.:** Ata da defesa com as respectivas assinaturas dos membros encontra-se no SIGA/Sistema de Fluxo de Dissertação/Tese e na Secretaria do Programa da Unidade.

CAMPINAS

2022

Dedico este trabalho aos meus pais, Alzira e Lair, que sempre me deram todo o apoio para que eu pudesse seguir meus sonhos. E a minha esposa Ingrid de Almeida Ribeiro pelo apoio, carinho e conselhos nesta jornada.

# Acknowledgments

I would like to thank,

Prof. Ricardo Luís Doretto, for the orientation, patience and all needed support to the realization of this thesis;

Unicamp and IFGW for the welcoming and supporting environment for the students; the university structure that makes my work not only possible but extremely comfortable;

all IFGW staff, specially for CPG and DFMC for the excellent support;

CNPq for the given opportunity of this Ph.D. scholarship;

my wife Ingrid for all her support and inspiration;

and to my family and friends, near and distant, who have always supported me in my journey.

## Abstract

In this thesis, we study the flat-band ferromagnetic phase of the Haldane-Hubbard model on a honeycomb lattice within a bosonization scheme for both Chern and  $Z_2$  topological insulators, focusing on the calculation of the spin-wave excitation spectrum. We consider a spinfull Haldane-Hubbard model with the noninteracting lower bands in a nearly flat band limit, previously determined for the spinless Haldane model, and at 1/4-filling of its corresponding noninteracting limit. Two configurations of the Haldane-Hubbard model, one that breaks time-reversal symmetry (correlated Chern insulator) and a second one that preserves time-reversal symmetry (correlated  $Z_2$  topological insulator), are discussed. Within the bosonization scheme, the Haldane-Hubbard model is mapped into an effective interacting boson model, whose quadratic term allows us to determine the spin-wave spectrum at the harmonic approximation. For the correlated Chern insulator, we show that the excitation spectrum has two branches with a Goldstone mode and Dirac points at center and at the  $K$  and  $K'$  points of the first Brillouin zone, respectively. In contrast, for the correlated  $Z_2$  topological insulator, the excitation spectrum also has two branches, but both of them are gapped and there is no Dirac points. Indeed, for the correlated  $Z_2$  topological insulator, we found that it is possible to define boson operators associated with two distinct spin-flip excitations, one that changes (mixed-lattice excitations) and a second one that preserves (same-lattice excitations) the index related with the two sublattices. We also consider the effects on the spin-wave spectrum due to an energy offset in the on-site Hubbard repulsion energies and due to the presence of an staggered on-site energy term (mass term), both quantities associated with the two triangular sublattices. For both perturbations, we found that an energy gap opens at the  $K$  and  $K'$  points, dissolving the Dirac points found in the spin-wave spectrum of the correlated Chern insulator. For the correlated  $Z_2$  topological insulator, a mild modification of the gap at the same points were found, with the overall spectrum retaining its shape. Moreover, for the Chern insulator, we also found some evidences for an instability of the flat-band ferromagnetic phase in the presence of the staggered on-site energy term. Finally, we comment on the differences between the bosonization scheme implementation for the correlated Chern and  $Z_2$  topological insulators on both square and honeycomb lattices.

**Keywords:** Strong correlated electron systems, topological insulators, Chern insulators, Haldane-Hubbard model, flat-band ferromagnetism, bosonization of two-dimensional electronic systems

## Resumo

Nesse trabalho, estudamos uma fase ferromagnética de banda plana do modelo de Haldane-Hubbard na rede hexagonal através de um método de bosonização desenvolvido recentemente para isolantes de Chern e isolantes topológicos  $Z_2$ . Em particular, procuramos determinar o espectro de excitação das ondas de spin. Consideramos configurações do modelo de Haldane-Hubbard onde as bandas eletrônicas (limite não-interagente) de mais baixa energia são quase-planas e com fator de preenchimento (limite não-interagente) igual a  $1/4$ . Duas versões distintas do modelo de Haldane-Hubbard foram estudadas, uma que quebra a simetria de inversão temporal (isolante de Chern correlacionado) e uma segunda que preserva a simetria de inversão temporal (isolante topológico correlacionado). Através do método de bosonização, mostramos que o modelo de Haldane-Hubbard é mapeado em um modelo bosônico efetivo e interagente, cujo termo quadrático nos permite determinar o espectro de excitação das ondas de spin em uma aproximação harmônica. Para o isolante de Chern correlacionado, encontramos que o espectro de excitação é constituído por dois ramos, apresentando um modo de Goldstone e pontos Dirac no centro e nos pontos  $K$  e  $K'$  da primeira zona de Brillouin, respectivamente. Para o isolante topológico correlacionado, verificamos que o espectro de excitação também é formado por dois ramos, porém ambos apresentam energia de gap finita e ausência de pontos de Dirac. De fato, para o isolante topológico, verificamos que é possível definir operadores bosônicos associados a dois tipos diferentes de excitações de spin, isto é, excitações que alteram (*mixed-lattice excitations*) e que preservam (*same-lattice excitations*) os índices de sub-rede dos operadores de spin. Além disso, consideramos os efeitos no espectro das ondas de spin associados (i) a uma diferença nos valores das energias de repulsão locais e (ii) à presença de um termo de energia de um corpo local alternado (termo de massa), ambas as quantidades relacionadas com as duas subredes triangulares. Para ambas as perturbações, encontramos que o espectro das ondas de spin do isolante de Chern correlacionado apresenta um gap de energia nos pontos  $K$  e  $K'$ , em contraste com o caso homogêneo que apresenta pontos de Dirac nessa região do espectro. Para o isolante topológico correlacionado, verificamos pequenas modificações no gap de energia dos pontos  $K$  e  $K'$ , sendo que o espectro mantém sua forma quando comparada com o caso não-perturbado. Importante, para o isolante de Chern, também encontramos algumas evidências de uma instabilidade da fase ferromagnética de banda plana na presença do termo de massa. Finalmente, comentamos sobre as diferenças na aplicação do método de bosonização para

os isolantes de Chern e topológicos correlacionados para modelos de Hubbard topológicos nas redes quadrada e hexagonal.

**Palavras-chave:** Sistemas eletrônicos fortemente correlacionados, isolantes topológicos, isolantes de Chern, modelo de Haldane-Hubbard, ferromagnetismo de banda plana, bosonização de sistemas eletrônicos bidimensionais.

# List of Figures

2.1	Schematic representations of the electronic band structure of (a) an insulator, (b) a metal, and (c) a semiconductor. The blue (red) lines symbolizes the filled (empty) bands, with the Fermi energy symbolized by $E_f$ . . . . .	24
2.2	In panel (a), schematics of the experimental set up of the classical Hall effect in a two dimensional system. When a transverse magnetic field $B$ is applied, it alters the movement of the charges of the current $I_X$ , leading to the measurement of a finite transverse voltage $V_H$ . Panel (b), representation of the measurements of the quantum Hall effect [4], with the longitudinal and transverse (Hall) resistivity given by $\rho_{xx}$ and $\rho_{xy}$ , respectively, as a function of the magnetic field $B$ . Figures adapted from Ref. [39]. . . . .	25
2.3	In panel (a), the schematic representation of the honeycomb lattice with its two sublattices A and B. The energy parameters of the Hamiltonian (2.8) are shown as $t_1$ , $t_2$ and $M$ . The complex phase of the second neighbor hopping will be positive (negative) for clockwise (counter-clockwise) motion. The first Brillouin zone is represented in panel (b) with some symmetrical points labeled. . . . .	27
2.4	Electronic band structure of Haldane model (2.8) along particular directions within the Brillouin zone [Fig. 2.3(b)], for different configurations at half-filling. (a) A metallic phase for $t_2 = 0$ and $M = 0$ , (b) a topological nontrivial phase for $t_2 \neq 0$ and $M = 0$ , and (c) a trivial insulating phase with $t_2 = 0$ and $M \neq 0$ . All curves were calculated for $\phi = \pi/3$ . . . . .	28
2.5	Phase diagram of the model (2.8), characterizing the trivial phases ( $\nu = 0$ ) and the topological phases ( $\nu = \pm 1$ ) as a function of the model parameters. The solid lines are delimited by Eq. (2.10). Figure extracted from Ref.[5].	29
2.6	Numerically calculated electronic spectrum for a finite zigzag graphene sheet ( $\sim 400$ sites ) using model (2.11). In the left panel, the bands for the topological phase and in the right panel for the trivial insulator. A small phase diagram showing the extent of the topological (quantum spin Hall) phase is drawn at the center. Extracted from Ref.[3]. . . . .	30

2.7	Evolution of the gap $\Delta_g$ between the valence (blue) and conduction (red) bands as a function of a set of parameter $\lambda = \lambda_1, \lambda_2, \dots$ that modifies a Hamiltonian $H(\mathbf{k}, \lambda_1, \lambda_2, \dots)$ . A quantum phase transition occurs at the gap closure, allowing the topological invariant to change its value. . . . .	31
2.8	In panel (a), a schematic representation of the Hamiltonian (2.13) on a checkerboard lattice. The electronic spectrum with a flat band is shown in (b), while a projection of the same spectrum calculated for a finite size system is shown in panel (c), with the red and green lines representing the chiral (counter-propagating) edge states. Figure adapted from Ref. [19]. . . . .	33
2.9	Free electronic band structure for (a) the Haldane model (2.8) on a honeycomb lattice and (b) for the $\pi$ -flux model on a square lattice discussed in Ref. [18], both corresponding to the nearly flat band limit. Figure adapted from Ref. [18]. . . . .	34
2.10	In (a), a schematic representation of the Hamiltonian (2.20) on a square lattice is shown. Solid black lines and its directions indicate the positive $t_1 \exp(i\pi/4)$ hopping (for spin- $\uparrow$ electrons). The dashed red and solid blue connections indicates that the next-nearest-neighbor hopping amplitude is equal to $+t_2$ and $-t_2$ respectively. The lattice vectors are represented in (b), where $\mathbf{a}_1 = a\hat{x}$ and $\mathbf{a}_2 = a\hat{y}$ . In (c), we have the first Brillouin zone with its high symmetry points. Figure from Ref. [24]. . . . .	35
2.11	Electronic spectrum of the free Hamiltonian (2.20) for different values of $t_2$ in paths along the first Brillouin zone [Fig. 2.10(c)]. As $t_2$ is increased, a band gap develops and the band dispersion modifies becoming almost flat for $t_2 = 1/\sqrt{2}t_1$ . Figure adapted from Ref.[24]. . . . .	36
3.1	(a) Schematic representation of the Haldane model (3.1) on the honeycomb lattice, indicating the nearest-neighbor $t_1$ and next-nearest-neighbor $t_2 e^{\pm i\phi}$ hoppings. An on-site Hubbard repulsion energy $U_a$ that will be added to the model latter is also shown. Blue and red circles indicate the sites of the (triangular) sublattices $A$ and $B$ , respectively. $\boldsymbol{\delta}_i$ and $\boldsymbol{\tau}_i$ are the nearest-neighbor (3.2) and next-nearest-neighbor (3.3) vectors, respectively. (b) The first Brillouin zone and its highly symmetric points: $\mathbf{K} = (4\pi/3\sqrt{3}, 0)$ , $\mathbf{K}' = (2\pi/3\sqrt{3}, 2\pi/3)$ , $\mathbf{M}_1 = (\pi/\sqrt{3}, \pi/3)$ , and $\mathbf{M}_2 = (0, 2\pi/3)$ . The nearest-neighbor distance of the honeycomb lattice $a = 1$ . . . . .	39

3.2	Band structure (3.14) of the noninteracting hopping term (3.1) (in units of the nearest-neighbor hopping amplitude $t_1$ ) along paths in the first Brillouin zone [Fig. 3.1(b)] for different values of the next-nearest-neighbor hopping amplitude $t_2$ and phase $\phi$ : (a) $t_2 = 0.3155 t_1$ , $\phi = 0$ (green) and $t_2 = 0.3155 t_1$ , $\phi = 0.656$ (magenta); (b) $\phi = 0.4$ (blue), $\phi = 0.5$ (green), and $\phi = 0.656$ (magenta), with $t_2$ given by the relation $\cos(\phi) = t_1/(4t_2)$ ; and (c) $\phi = 0.656$ (magenta) $\phi = 0.75$ (green), and $\phi = 0.85$ (blue), with $t_2$ given by the relation $\cos(\phi) = t_1/(4t_2)$ . . . . .	41
3.3	Contour plot of the Berry curvature (3.16) of the (a) lower and (b) upper electronic bands (3.14) of the Hamiltonian (3.1) at the nearly flat band limit (3.18). . . . .	42
3.4	Band structure (3.14) of the noninteracting hopping term (3.1) with the additional staggered on-site energy term (3.19) (in units of the nearest-neighbor hopping amplitude $t_1$ ) along paths in the first Brillouin zone for the next-nearest-neighbor hopping amplitude $t_2 = 0.3155 t_1$ , phase $\phi = 0.656$ , and staggered on-site energy $M = 0$ (magenta), 0.1 (green), 0.2 (blue), and $0.3 t_1$ (orange). . . . .	44
3.5	Electronic spectrum (3.14) with modification (3.20) at the nearly flat band limit (3.18) for (a) $M = 0.05 t_1$ and (b) $M = 0.1 t_1$ . A finite $M$ lifts the degeneracy between the spin- $\uparrow$ (green) and the spin- $\downarrow$ (magenta) bands as compared to the Chern insulator [Fig. 3.4]. The path chosen in momentum space follows the highly symmetric points in the first Brillouin zone [Fig. 3.1(b)]. . . . .	47
3.6	Schematic representation of the ground state (3.31) of the noninteracting term (3.1) in the nearly flat limit (3.18) of the lower band $c$ at 1/4-filling. Although the free bands $c$ and $d$ are doubly degenerated with respect to the spin degree of freedom, an offset between the $\sigma = \uparrow$ and $\downarrow$ bands are introduced for clarity. . . . .	48
4.1	Schematic representation of a particle-hole pair excitation above the ground state (3.31). Although the free bands $c$ and $d$ are doubly degenerated with respect to the spin degree of freedom, an offset between the $\sigma = \uparrow$ and $\downarrow$ bands are introduced for clarity. . . . .	51
4.2	The real (solid magenta line) and imaginary (dashed green line) parts of (a) the coefficient $\bar{\omega}_{\mathbf{q}}^{01}$ [Eq. (4.21)] and (b) the coefficient $\epsilon_{\mathbf{q}}^{01}$ [Eq. (4.25)] along paths in the first Brillouin zone [Fig. 3.1(b)] for the Haldane-Hubbard model (3.1) in the nearly-flat band limit (3.18) of the lower noninteracting band $c$ . . . . .	54

- 4.3 The elementary excitation (spin-wave) energies of the effective boson model (4.28) in the harmonic approximation for the nearly-flat band limit (3.18): dispersion relations (4.34) (real part, solid green line) and (4.35) (solid magenta line) along paths in the first Brillouin zone [Fig. 3.1(b)]. The dashed blue line indicates the imaginary part of  $\Omega_{+,\mathbf{q}} = -\Omega_{-,\mathbf{q}}$  [see Eq. (4.34)], which is multiplied by a factor of 50 for clarity. On-site repulsion energies: (a)  $U_A = U_B = U$ ; (b)  $U_B = 0.8 U_A = 0.8 U$ ; and (c)  $U_B = 0.6 U_A = 0.6 U$ . . . . . 56
- 4.4 The spin-wave energies (solid lines) and the Stoke spectrum (gray) of the Haldane-Hubbard model (4.1) at the nearly flat band limit (3.18) calculated via exact diagonalization of the Hamiltonian for a finite system [29] along paths in the first Brillouin zone [Fig. 3.1(b)]. On-site repulsion energies: (a<sub>1</sub>)  $U_A = U_B = U$ ; (b<sub>1</sub>)  $U_B = 1.0688$  and  $U_A = 1.2$ ;  $C = 0$  is the Chern number of the lower band. Figure adapted from Ref. [29] . . . . . 58
- 4.5 The real part of the dispersion relation (4.34) (solid line) along paths in the first Brillouin zone [Fig. 3.1(b)] for on-site repulsion energies  $U_A = U_B = U$  and  $t_2$  given by the relation  $\cos(\phi) = t_1/(4t_2)$ . (a)  $\phi = 0.4$  (blue),  $\phi = 0.5$  (green),  $\phi = 0.656$  (magenta) and (b)  $\phi = 0.656$  (magenta),  $\phi = 0.75$  (green),  $\phi = 0.85$  (blue). The corresponding dashed line indicates the imaginary part of  $\Omega_{+,\mathbf{q}} = -\Omega_{-,\mathbf{q}}$  [see Eq. (4.34)], which is multiplied by a factor of 50 for clarity. . . . . 59
- 4.6 The real part of the dispersion relation (4.34) (solid line) along paths in the first Brillouin zone [Fig. 3.1(b)] for the optimal parameters (3.18), on-site Hubbard energies  $U_A = U_B = U = t_1$ , and staggered on-site energy  $M = 0.1$  (magenta) and  $0.2t_1$  (green). (b) Similar results for the spin-wave spectrum (4.34), but with the replacement (4.41). The corresponding dashed line indicates the imaginary part of  $\Omega_{+,\mathbf{q}} = -\Omega_{-,\mathbf{q}}$  [see Eq. (4.34)], which is multiplied by a factor of 50 for clarity. . . . . 61
- 5.1 Spin-wave spectrum (5.16) of the **mixed lattice** excitations (5.4), calculated from the effective bosonic Hamiltonian within the harmonic approximation (5.14) and at the nearly flat band limit (3.18). Solid and dashed lines represent the spectrum real and imaginary parts, respectively, with a multiplicative factor 20 is employed for the imaginary part. The on-site repulsion energies are (a)  $U_A = U_B = U$ ; (b)  $U_B = 0.8 U_A = 0.8 U$  and (c)  $U_B = 0.6 U_A = 0.6 U$ . The path chosen in momentum space follows the highly symmetric points in the first Brillouin zone [Fig. 3.1(b)]. . . . . 67

- 5.2 Spin-wave spectrum (5.16) of the **mixed lattice** excitations (5.4), calculated from the effective bosonic Hamiltonian at the harmonic approximation (5.14). Solid and dashed lines represent the spectrum real and imaginary parts, respectively, with a multiplicative factor 15 is present for the imaginary part. We have (a) descending and (b) ascending values of  $\phi$ , given by the sets  $\phi = 0.4, 0.5, 0.656$  and  $\phi = 0.656, 0.7, 0.8$ . The phase  $\phi = 0.655$  is represented by the solid magenta line in both panels, solid green line represents  $\phi = 0.5$  in panel (a) and  $\phi = 0.7$  in panel (b), and solid blue line represents  $\phi = 0.4$  in panel (a) and  $\phi = 0.8$  in panel (b), respectively. In both cases  $t_2$  is given by the relation  $\cos(\phi) = t_1/(4t_2)$ . The on-site repulsion energies is  $U_A = U_B = U$  in all cases and the path chosen in momentum space follows the highly symmetric points in the first Brillouin zone [Fig. 3.1(b)]. . . . . 69
- 5.3 Spin-wave spectrum (5.16) of the **same lattice** excitations (5.9), calculated from the effective bosonic Hamiltonian harmonic approximation (5.14) at the nearly flat band limit (3.18). On-site repulsion energies (a)  $U_A = U_B = U$ ; (b)  $U_B = 0.8 U_A = 0.8 U$  and (c)  $U_B = 0.6 U_A = 0.6 U$ . The path chosen follows the highly symmetric points in the first Brillouin zone [Fig. 3.1(b)]. The imaginary part of the spectrum (dashed lines) is zero, but is shown for completeness. . . . . 70
- 5.4 Spin wave spectrum (5.16) of the **same lattice** excitations (5.9), calculated from the effective bosonic Hamiltonian harmonic approximation (5.14). We have (a) descending and (b) ascending values of  $\phi$ , given by the sets  $\phi = 0.4, 0.5, 0.656$  and  $\phi = 0.656, 0.7, 0.8$ . The phase  $\phi = 0.655$  is represented by the solid magenta line in both panels, solid green line represents  $\phi = 0.5$  in panel (a) and  $\phi = 0.7$  in panel (b), and solid blue lines represents  $\phi = 0.4$  in panel (a) and  $\phi = 0.8$  in panel (b), respectively. In both cases  $t_2$  is given by the relation  $\cos(\phi) = t_1/(4t_2)$ . The on-site repulsion energies is  $U_A = U_B = U$  in all cases and the path chosen in momentum space follows the highly symmetric points in the first Brillouin zone [Fig. 3.1(b)]. The imaginary part of the spectrum (dashed lines) is zero, but is shown for completeness. . . . . 72

5.5	Spin-wave spectrum (5.16) of the (a) <b>mixed lattice</b> excitations (5.4) and of the (b) <b>same lattice</b> excitations (5.9), calculated from the effective bosonic Hamiltonian (4.28) at the harmonic approximation. With the parameters $M = 0.05$ (solid green line) and $M = 0.1$ (solid magenta line) and $t_2$ and $\phi$ given by the nearly-flat band limit (3.18). Solid and dashed lines represent the spectrum real and imaginary parts, respectively. The on-site repulsion energies are $U_A = U_B = U$ in all cases and the path chosen in momentum space follows the highly symmetric points in the first Brillouin zone [Fig. 3.1(b)]. . . . .	73
C.1	The real (solid line) and imaginary (dashed line) parts of the $F_{\alpha\beta,\mathbf{q}}^2$ function [Eq. (4.15)] for the Haldane-Hubbard model (4.1) in the nearly-flat band limit (3.18): (a) $F_{00,\mathbf{q}}^2$ and $F_{11,\mathbf{q}}^2$ (b) $F_{01,\mathbf{q}}^2$ and $F_{10,\mathbf{q}}^2$ for staggered on-site energy $M = 0$ ; (c) $F_{01,\mathbf{q}}^2$ for staggered on-site energy $M = 0.2 t_1$ . . . . .	95
D.1	The real (solid line) and imaginary (dashed line) parts of the $F_{\alpha\beta,\mathbf{q}}^2$ function [Eq. (5.6), ML excitations] for the Haldane model (3.1) in the nearly-flat band limit (3.18) along paths in the first Brillouin zone: (a) $F_{00,\mathbf{q}}^2$ and $F_{11,\mathbf{q}}^2$ and (b) $F_{01,\mathbf{q}}^2$ and $F_{10,\mathbf{q}}^2$ . . . . .	98
D.2	The real (solid magenta line) and imaginary (dashed green line) parts of the kinetic coefficients (a) $\bar{\omega}_{\mathbf{q}}^{00}$ and (b) $\bar{\omega}_{\mathbf{q}}^{11}$ [Eq. (4.21), ML excitations] along paths in the first Brillouin zone for the Haldane model (3.1) in the nearly-flat band limit (3.18). (c) The real (solid line) and imaginary (dashed line) parts of the coefficients $\epsilon_{\mathbf{q}}^{01}$ and $\epsilon_{\mathbf{q}}^{10}$ [Eq. (4.25), ML excitations] for the topological Hubbard model in the nearly-flat band limit (3.18) and on-site repulsion energies $U_A = U_B = U$ . . . . .	99
D.3	SL excitations (5.9). The real (solid line) and imaginary (dashed line) parts of the $F_{\alpha\beta,\mathbf{q}}^2$ function [Eq. (D.8) for the Haldane model (3.1) in the nearly-flat band limit (3.18) along paths in the first Brillouin zone: (a) $F_{00,\mathbf{q}}^2$ and $F_{11,\mathbf{q}}^2$ and (b) $F_{01,\mathbf{q}}^2$ and $F_{10,\mathbf{q}}^2$ . (c) The real (solid line) and imaginary (dashed line) parts of the coefficients $\epsilon_{\mathbf{q}}^{01}$ and $\epsilon_{\mathbf{q}}^{10}$ [Eq. (4.25)] for the topological Hubbard model in the nearly-flat band limit (3.18) and on-site repulsion energies $U_A = U_B = U$ . . . . .	100

E.1	Spin-wave excitation spectra (4.34) for the flat-band ferromagnetic phase of the square lattice $\pi$ -flux model (see Ref. [24] for details): (a) Next-nearest-neighbor hopping amplitudes $t_2 = 1/\sqrt{2}$ and on-site repulsion energy $U_B = 0.8U_A = 0.8U$ (magenta) and $U_B = 0.6U_A = 0.6U$ (green); (b) $U_A = U_B = U$ and $t_2 = 1/\sqrt{2}$ (magenta), 0.4 (green), and $0.3t_1$ (blue); (c) $t_2 = 1/\sqrt{2}$ , $U_A = U_B = U$ , and staggered on-site energy $M = 0.1$ (magenta) and $0.2t_1$ (green). . . . .	103
E.2	(a) The energy of the Goldstone mode for the square lattice $\pi$ -flux model with one-site staggered energy $M = 0.2t_1$ in terms of $\Delta\eta = \eta - \pi/4$ determined with the dispersion relations (4.34) (solid green line) and (4.35) (solid magenta line). (b) Dispersion relation (4.35) for $\Delta\eta = 0$ (dashed blue line) and $\Delta\eta = 0.258$ (solid magenta line). . . . .	104
F.1	Contour plot of the Berry curvature functions of the lower spin-wave band for the (a) ML and (b) SL excitations, at nearly flat-band limit and on-site Hubbard repulsion energies $U = U_A = U_B$ . . . . .	105

# Contents

<b>1</b>	<b>Introduction</b>	<b>19</b>
<b>2</b>	<b>Theoretical background</b>	<b>23</b>
2.1	Metals, insulators, and semiconductors . . . . .	23
2.2	Quantum Hall effects . . . . .	24
2.3	Topological band theory . . . . .	26
2.3.1	Haldane model: the first Chern insulator . . . . .	26
2.3.2	Kane and Mele model: $Z_2$ topological insulator . . . . .	29
2.3.3	General concepts of topological band theory . . . . .	30
2.4	Tight-binding models with topologically nontrivial flat bands . . . . .	32
2.4.1	Spinless models . . . . .	32
2.4.2	Spinfull models . . . . .	34
<b>3</b>	<b>Topological flat-band ferromagnetism</b>	<b>38</b>
3.1	Spinfull Haldane model : Chern insulator . . . . .	38
3.1.1	Electronic bands and the nearly flat-band limit . . . . .	38
3.1.2	Mass term . . . . .	43
3.2	Spinfull Haldane model with TRS : $Z_2$ topological insulator . . . . .	44
3.2.1	Time-reversal-symmetric Hamiltonian . . . . .	44
3.2.2	Mass term . . . . .	46
3.3	Itinerant ferromagnetism . . . . .	47
<b>4</b>	<b>Correlated Chern insulator</b>	<b>49</b>
4.1	Haldane-Hubbard model for the Chern insulator . . . . .	49
4.2	Bosonization scheme . . . . .	50
4.2.1	Effective bosonic Hamiltonian . . . . .	52
4.2.2	Spin-wave spectrum in the nearly flat band limit . . . . .	53
4.2.3	Spin-wave spectrum away from the nearly flat band limit . . . . .	59

<b>5</b>	<b>Correlated <math>Z_2</math> topological insulator</b>	<b>63</b>
5.1	Time-reversal-symmetric Haldane Hubbard model for the $Z_2$ topological insulator . . . . .	63
5.2	Bosonization scheme for the $Z_2$ topological insulator . . . . .	64
5.3	ML excitations . . . . .	66
5.3.1	Spin waves at the flat band limit . . . . .	66
5.3.2	Spin waves away from the flat band limit . . . . .	68
5.4	SL excitations . . . . .	70
5.4.1	Spin waves at the flat-band limit . . . . .	70
5.5	Spin waves away from the flat band limit . . . . .	71
5.6	Mass term . . . . .	72
5.7	Chern numbers of the spin-wave bands . . . . .	73
<b>6</b>	<b>Summary and conclusion</b>	<b>76</b>
	<b>Bibliography</b>	<b>79</b>
	<b>Appendix</b>	<b>85</b>
<b>A</b>	<b>Spin symmetry of the noninteracting topological model</b>	<b>86</b>
<b>B</b>	<b>Details about the bosonization scheme</b>	<b>88</b>
B.1	About the condition (4.29) . . . . .	88
B.2	The bosonic representation of the fermionic operators . . . . .	90
<b>C</b>	<b>Details of the bosonization scheme: Chern insulator</b>	<b>94</b>
C.1	Function definitions : $F_{\alpha\beta,\mathbf{q}}$ and $\mathcal{G}_{\alpha\beta\alpha\sigma}(\mathbf{k}, \mathbf{q})$ . . . . .	94
<b>D</b>	<b>Details of the bosonization scheme: <math>Z_2</math> topological insulator</b>	<b>97</b>
D.1	Function definitions for the ML excitations . . . . .	97
D.2	Function definitions for the SL excitations . . . . .	100
<b>E</b>	<b>Square lattice <math>\pi</math>-flux model</b>	<b>102</b>
<b>F</b>	<b>Chern number of the magnon bands</b>	<b>105</b>

# Introduction

This thesis consists on theoretical modeling of electronic and magnetic properties of a recently discovered class of materials. These recently discovered materials, the so-called Chern and topological insulators, are usually compounds of the elements Bismuth, Selenium, Tellurium and Antimony [1, 2]. What makes these compounds special is the fact that they conduct electricity only through the material edge [border in two dimensions (2D) and surface in three dimensions (3D)] while the material core remains a complete insulator. This opposes how electrons move in a common metal, as they are allowed to move throughout the whole material. Also, they oppose how insulators work as no type of conduction should exist. Another characteristic of these new materials is that the conducting surface electronic states are protected by time-reversal symmetry, i.e., they persist even when there are mechanical or chemical alterations that modifies the material properties, as long as the bulk insulating electronic band gap still remains [2]. Because this quantum states persist as long as the bulk gap is finite, these materials are dubbed "topologically protected". Moreover, these special quantum states are robust against both weak disorder and non-magnetic back scattering (scattering that reverses the direction of motion), which allows for energy transportation without dissipation [1, 2, 3]. All the properties described above may remind the reader of the quantum Hall effect [4] properties and, as we are going to see in the following, this is somehow the driving mechanism for the existence of these quantum surface states.

Interestingly, the first theoretical prediction of a Chern insulator came from the study of graphene: a two-dimensional zero gap semiconductor that is composed by carbon atoms ordered in a hexagonal lattice structure [5]. In this paper, Haldane proposed a tight-binding model that displays two insulating phases at half-filling, depending on the model parameters and symmetries. The phase that maintains time-reversal symmetry but breaks inversion symmetry yield a (trivial) insulator, while the phase with broken time-reversal symmetry was also an insulator, but it exhibited a quantized Hall conductance even without the need of an external magnetic field. Indeed, such an effect, the so-called

anomalous quantum Hall effect [5], is generated by quantum surface states related to the fact that the electronic band structure of the model proposed by Haldane is topologically nontrivial [6], i.e., the corresponding Chern number of each band is finite [7, 8]. The arguments that led to this conclusion followed the work of Thouless, Kohmoto, Nightingale and den Nijs (TKNN) [9], whom showed that the quantized Hall conductivity in quantum Hall systems are related to the integral of some derivatives of the wave function, a quantity known as the TKNN invariant. Later, the TKNN invariant was shown to be the Chern number of the electronic bands [10], a topological invariant that could indicate whether an integer quantum Hall effect could be present or not. Although Haldane model started as a theoretical concept, it was later experimentally implemented in a system with ultracold fermions in an optical honeycomb lattice [11] (see also the reviews [12, 13]).

The prediction of another type of topological insulator, the so-called  $Z_2$  topological insulator, followed years later after Haldane paper, when Kane and Mele [3, 14] proposed a model where time-reversal symmetry is preserved. The model included a first neighbor hopping term, a spin-orbit term that gives rise to imaginary hoppings, a Rashba term, and a mass term. They showed that a minimal model, i.e., when the Rashba and mass terms are not include, could be split into two distinct copies of Haldane original model, one for each spin sector and, in this way, preserving time-reversal symmetry. In this new system, counter-propagating electronic surface modes cancel out, leaving a zero net electronic current, and therefore, not realizing the anomalous quantum Hall effect. Instead, a net surface spin current exist, producing a quantized spin Hall effect [3] for the total spin component  $S_z$  conserved Hamiltonian. Similarly to the Chern insulator, the quantized spin Hall effect was directly associated with another topological number, in this case, the  $Z_2$  invariant [3, 14]. This new invariant assumes only two possible integer values 0 and 1, pinning the presence of the spin Hall effect to one particular number. In particular, if the total spin component  $S_z$  is conserved in the Hamiltonian, the  $Z_2$  invariant is proportional to the spin Chern number, defined as half of the difference between the Chern numbers of the filled spin- $\uparrow$  and spin- $\downarrow$  bands [3]. Later, the  $Z_2$  topological insulator was realized in a true material, namely the HgTe/(Hg,Cd)Te quantum wells [1].

Interestingly, experimental evidences for this type of materials were found. For the  $Z_2$  topological insulators, some measurements of Hall resistivity  $R_{xy}$  and Landau Levels dispersion on samples of HgTe/(Hg,Cd)Te quantum wells [1, 15] indicate the presence of the quantum spin Hall effect. Transport measurements in the HgTe quantum wells were also probed by two-point and four-point Hall terminals [16], and the computed conductivity for the helical edge states were shown to differs from ones of the usual quantum Hall effect and diffusive transport. For the Chern insulators, experimental data is still limited to cold atoms systems [11], where the Haldane model can be realized with all its features. Moreover, for three-dimensional topological insulators, progress was made with several experiments using angle-resolved photoemission spectroscopy (ARPES) for

a class of materials:  $Bi_2Se_3$ ,  $Bi_2Te_3$  and  $Sb_2Te_3$ . References to these experiments can be found in some reviews of the area [2, 6].

One fundamental concept of the topological and Chern insulators is that the topological invariant can only change its value if the bulk insulating gap is closed and opened again. Therefore, the topological invariant defines a topological class of Hamiltonians [17] with different electronic spectra that can be slowly deformed into one another without losing their topological properties. This fact allowed for the development of topological tight-binding models, specially in two dimensions, with fine tuned parameters that would yield flat electronic bands [18, 19, 20, 21, 22]. In these systems, several lattices are considered, being the checkerboard and the honeycomb lattice the most common. A standard feature of all of these models is the appearance of complex hopping amplitudes that are related to spin-orbit interactions. A fine adjustment of these model parameters can give rise to topologically nontrivial bands. Furthermore, some of these flat-band topological models also include a Hubbard term to account for electron-electron interaction, which is a still developing field (see reviews [8, 23]). In particular, one topological Hubbard model that displays nearly flat free-electronic bands and that is the basis of this thesis was discussed by Doretto and Goerbig [24]. Indeed, they have studied a spinfull model on a square lattice, that describes both correlated Chern insulator and correlated  $Z_2$  topological insulator. As showed by Neupert *et al.* [18], the noninteracting part of the model supports topological flat bands. At the noninteracting limit and at quarter filling of the bands, a spin-polarized phase develops for both the time-reversal symmetric case ( $Z_2$  topological insulator) and when time-reversal symmetry is broken (Chern insulator). To describe this flat-band phase, they used a bosonization scheme that was previously used to describe quantum Hall systems [24, 25, 26, 27]. Within the bosonization scheme, they were able to map the original fermionic interacting Hamiltonian into an effective interacting bosonic Hamiltonian that describes the magnetic excitations above the ferromagnetic ground state. Employing a harmonic approximation for this effective bosonic Hamiltonian, the spin-wave excitation spectrum was calculated at the nearly flat band limit, which showed a characteristic ferromagnetic quadratic dispersion near the center of the first Brillouin zone for the correlated Chern insulator. Later, it was verified that this analytical results are in very good qualitative agreement with numerical results [28] for the nearly flat band limit. Indeed, as presented in other interacting topological models [29, 30, 31, 32, 33], a ferromagnetic ground state seems to be stabilized by a finite Hubbard energy  $U > U_c$ .

Inspired by Ref. [24], we explored whether a flat-band ferromagnetic phase would be possible in a Haldane-Hubbard model on a honeycomb lattice at 1/4-filling of its noninteracting limit. We also investigated how the bosonization scheme behaves in this lattice and modified it appropriately. In this way, we were able to describe both correlated Chern and  $Z_2$  topological insulators on a honeycomb lattice [34]. More specifically, the

noninteracting part of the model has four electronic bands, two lower and two upper degenerated bands. The lower bands can be made nearly flat by the fine tuning of the model parameters [18]. Each band have a nonzero Chern number and, at 1/4-filling, a ferromagnetic ground state was also found. Using the ferromagnetic state as the reference state for the bosonization scheme, we defined bosonic operators that correspond to the low energy spin excitations above the ground state. Then, at the harmonic approximation, we were able to calculate the spin-wave excitation spectrum. By slightly changing the model parameters, we probed the stability of the ferromagnetic phase by looking at some features in the spin-wave spectrum. We showed that such a ferromagnetic phase is stable at the nearly flat band limit for both correlated Chern and  $Z_2$  topological insulators. Away from this limit, the spin wave spectrum change slightly but do not affect the general ferromagnetic behavior. As far as we know, our result correspond to the first determination of the spin-wave spectrum for the correlated  $Z_2$  topological insulator at 1/4-filling.

This thesis is organized as follows: We begin with a theoretical background review in Chapter 2, discussing briefly some concepts of electronic band theory and giving a topological view of the quantum Hall effect. Furthermore, we comment on Haldane model, which led to the discovery of Chern insulators, and the Kane-Mele model, which led to the discovery of the  $Z_2$  topological insulators. Some topological models containing electronic flat bands are also introduced in the same chapter. Chapter 3 is devoted to the introduction of the spinfull Haldane model on a honeycomb lattice, where we calculate the free-electronic spectrum and discuss the nearly flat band limit. Also, the differences between the Chern and  $Z_2$  topological insulator modeling are discussed. In Chapter 4, interactions are included and the bosonization scheme for the honeycomb lattice is developed for the Chern insulator; also commenting on the differences between its description in the square lattice [24]. Furthermore, we also show the calculated spin-wave spectrum at the flat band limit and away from it. The bosonization scheme discussion is extended to the correlated  $Z_2$  topological insulator in Chapter 5, where the spin-wave spectra are calculated for the limits cited above, with the interpretation of the results. Finally, Chapter 6 has an additional discussion of the results and the conclusions of the work. Some additional results and further details about the bosonization formalism are left to the six Appendices.

The results of this thesis are condensed into two articles, one published in 2021, Ref. [34], and a second one that is in preparation, Ref. [35].

# Chapter 2

## Theoretical background

In this chapter, some aspects of the theoretical background needed to understand the physics of topological insulators are reviewed. We start by reviewing the band theory [36, 37, 38]. Next, the quantum Hall effect [4] is discussed using a topological band paradigm [9]. We then introduce the first model used to describe a Chern insulator [5] and the first model to describe a  $Z_2$  topological insulator [3], with the general topological band theory [2] discussed in the sequence. By the end of this chapter, the concept of flat-band ferromagnetism with topologically nontrivial free-electronic bands will be presented in a tight-binding model [18, 24], which will be the basis for the main calculations of this thesis.

### 2.1 Metals, insulators, and semiconductors

This section is meant to recall some basic concepts of electronic bands and it should be treated as an introductory material for the thesis. For more details, we refer the reader to condensed matter books [37, 38].

One important property of solid-state materials is how they behave when subjected to an electric field. There are two possible responses at zero temperature: (i) either the material does not respond at all or (ii) the material starts conducting electricity. The first type of material is called an insulator, while the later is referred as a conductor. Such distinct behaviors can be explained by how strong the electrons are bound to the individual atoms. Materials that have loosely bound electrons start conducting when small electric fields are applied, while very large fields are required to overcome the electronic binding energy in insulators.

Another way to further classify these materials is by looking at their electronic bands and their respective fillings. For an insulator at zero temperature, the filled electronic band (valence band) is separated from the the next electronic band (conduction band) by a large energy gap (several electron-Volts). Therefore, high electric fields are necessary

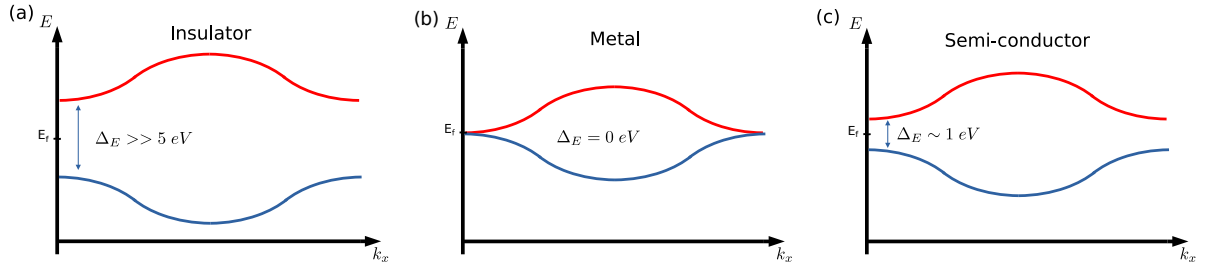


**Figure 2.1:** Schematic representations of the electronic band structure of (a) an insulator, (b) a metal, and (c) a semiconductor. The blue (red) lines symbolizes the filled (empty) bands, with the Fermi energy symbolized by  $E_f$ .

to move an electron to the next accessible state, as the neighboring states of the valence band are completely filled. Figure 2.1(a) pictorially represents the electronic bands of an one-dimensional (1D) insulator, with the valence band in blue and the conduction one in red. For crystalline periodic solids, the (quasi-)momentum is a good quantum number to label the states, and therefore, each momentum in the  $k$ -axis represents a state. On the other hand, in metallic materials, the valence and conduction bands touch each other giving rise to a bigger connected band which is filled (partially) up to the Fermi energy  $E_f$ . A schematic representation of such metallic band is shown in Figure 2.1(b). We can see that the (high energy) available electronic states (red) are energetically very close to the filled states (blue). In contrast, Figure 2.1(c) shows a generic band structure of a semiconductor. Semiconductors are characterized by very small band gaps ( $\sim 1 \text{ eV}$ ) separating the valence and conducting bands, thus having insulating behavior for small external electric fields while showing conducting behavior for moderate to high fields. It is possible to show that the Fermi energy of a semiconductor lays midway of the energy gap. Another interesting property of semiconductors is that they can be doped, that is, chemical impurities can be added and it can increase or reduce the number of unbound electrons, and therefore, changing the electronic conductivity.

As will be seen in later sections, the form of the electronic bands depends on both the geometry of the solid as well as how the electrons move throughout the lattice.

## 2.2 Quantum Hall effects

Before discussing the quantum Hall effect, we start by remembering the classical Hall effect [37]. Let's consider a two-dimensional conductor under the influence of an electric and a magnetic field as illustrated in Fig. 2.2(a). Due to the conducting nature of the material, an electric field drives the electrons to move in the direction of the field, giving rise to an electric current  $I_X$ . If a magnetic field is applied perpendicular to the sample, a secondary effect will be seen: a voltage drop  $V_H$  perpendicular to the direction of the electric and the magnetic fields, i.e., the classical Hall effect is observed. In mathematical

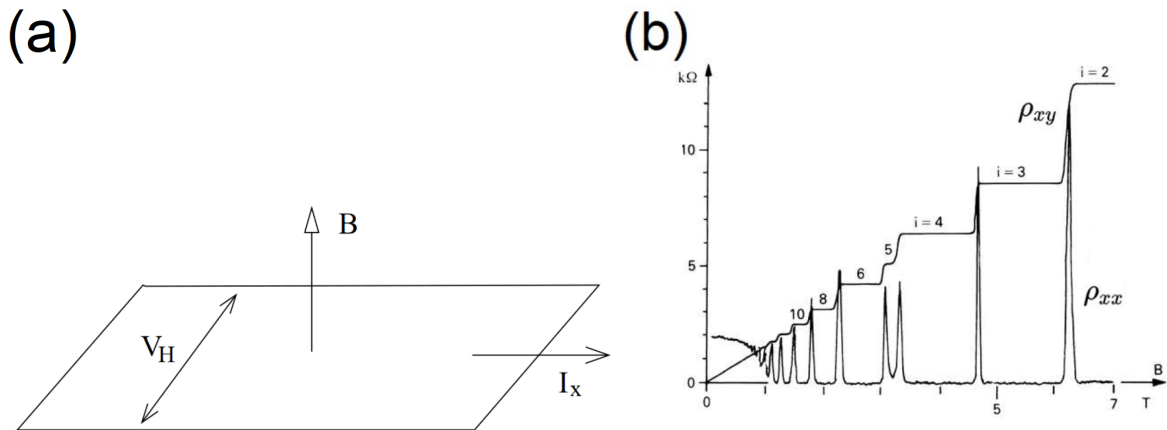


**Figure 2.2:** In panel (a), schematics of the experimental set up of the classical Hall effect in a two dimensional system. When a transverse magnetic field  $B$  is applied, it alters the movement of the charges of the current  $I_X$ , leading to the measurement of a finite transverse voltage  $V_H$ . Panel (b), representation of the measurements of the quantum Hall effect [4], with the longitudinal and transverse (Hall) resistivity given by  $\rho_{xx}$  and  $\rho_{xy}$ , respectively, as a function of the magnetic field  $B$ . Figures adapted from Ref. [39].

language, we can use a generalization of Ohm's law to quantify this effect: The relation between the driving electric field and the current density is given by

$$\mathbf{J} = \begin{pmatrix} \sigma_{xx} & \sigma_{xy} \\ \sigma_{yx} & \sigma_{yy} \end{pmatrix} \mathbf{E} = \hat{\sigma} \cdot \mathbf{E}, \quad (2.1)$$

where  $\hat{\sigma}$  is the conductivity tensor. The off-diagonal terms of the  $\hat{\sigma}$  tensor measure how strong is the transverse response due to the applied electric field and it is known as the **Hall conductivity**. Of course, the Hall conductivity should somehow depends on the applied magnetic field and, just to give an example of such relation, the result from the Drude model [37] is given by

$$\sigma_{xy} = \frac{ne^2\tau}{m} \frac{\left(\frac{eB}{m}\right)\tau}{1 + \left(\frac{eB}{m}\right)^2\tau}, \quad (2.2)$$

where  $e$ ,  $n$ , and  $m$  are the electron charge, density and mass, respectively, the magnetic field is represented by  $B$ , while  $\tau$  is a parameter representing a "friction" in Drude's model.

The quantum version of the Hall effect, which happens for very low temperatures and moderate to strong magnetic fields, yields a very different expression for the Hall conductivity [4]:

$$\sigma_{xy} = \nu \frac{e^2}{h}, \quad (2.3)$$

where  $\nu$  represents an integer number,  $e$  is the electron charge and  $h$  is Planck's constant. Surprisingly, there is a quantization of a macroscopical quantity in units of  $\frac{e^2}{h}$ , which is directly related to a quantum mechanical effect. Figure 2.2(b) shows a pictorial represen-

tation of the measurements of the longitudinal and transverse (Hall) resistivity,  $\rho_{xx}$  and  $\rho_{xy}$ , where we can see the distinct quantized plateaus for  $\rho_{xy}$ . What is interesting about this quantization is that it can be understood in terms of the (topological) properties of the electronic bands. As Thouless, Kohmoto, Nightingale, and den Nijs (TKNN) showed using the Kubo formula, for quantum Hall systems [9, 10]

$$\sigma_{xy} = \frac{ie^2}{2\pi\hbar} \sum_{\text{filled bands}} \int_{BZ} d^2k \int_{\text{unit cell}} d^3r \left( \frac{\partial u^*}{\partial k_x} \frac{\partial u}{\partial k_y} - \frac{\partial u^*}{\partial k_y} \frac{\partial u}{\partial k_x} \right), \quad (2.4)$$

where  $u(k_x, k_y)$  is an extended version of the wave function subjected to the generalized Bloch conditions. It was showed that the integrals in Eq. (2.4) could only assume integer values times  $4\pi i$ , thus explaining the quantization (2.3) of the Hall conductivity. This formula became known in the literature as the TKNN invariant. Later, this invariant was understood to be the integral of the Berry curvature  $\Omega_n(\mathbf{k})$  [40], that is,

$$\sigma_{xy} = \frac{e^2}{\hbar} \int_{BZ} \frac{d^2k}{(2\pi)^2} \Omega_n(\mathbf{k}), \quad (2.5)$$

where

$$\Omega_n(\mathbf{k}) = i \langle \nabla_{\mathbf{k}} u_n(\mathbf{k}) | \times | \nabla_{\mathbf{k}} u_n(\mathbf{k}) \rangle \cdot \hat{z}. \quad (2.6)$$

Interestingly, the integral of the Berry curvature defines the *Chern number*

$$C_n = \int_{BZ} \frac{d^2k}{2\pi} \Omega_n(\mathbf{k}), \quad (2.7)$$

that always assumes integer values [6, 10, 41].

## 2.3 Topological band theory

In this section, we provide a brief introduction to the two historical models that pioneered the study of topological and Chern insulators. Following this summary, the more general topological band theory will be discussed.

### 2.3.1 Haldane model: the first Chern insulator

Here we will discuss the physical aspects of Haldane model for graphene [5]. As mentioned in the Introduction, the model describes electrons hopping on a honeycomb lattice, which is made out of two superposed triangular lattices as shown in Figure 2.3(a).

The model Hamiltonian of the system is given by the (spinless) tight-binding model:

$$H = t_1 \sum_{\langle ij \rangle} c_i^\dagger c_j + \sum_{\langle\langle ij \rangle\rangle} t_2 e^{-i\phi_{ij}} c_i^\dagger c_j + M \sum_{i \in a, a} (-1)^a c_i^\dagger c_i, \quad (2.8)$$

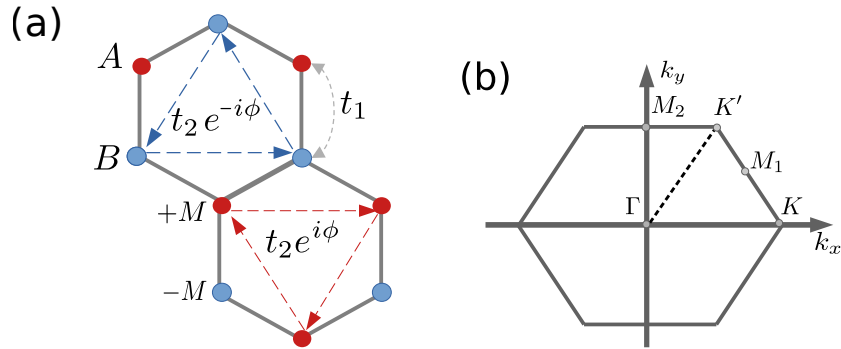


**Figure 2.3:** In panel (a), the schematic representation of the honeycomb lattice with its two sublattices A and B. The energy parameters of the Hamiltonian (2.8) are shown as  $t_1$ ,  $t_2$  and  $M$ . The complex phase of the second neighbor hopping will be positive (negative) for clockwise (counter-clockwise) motion. The first Brillouin zone is represented in panel (b) with some symmetrical points labeled.

where the operator  $c_i^\dagger$  ( $c_j$ ) creates (destroys) an electron at site  $i$  ( $j$ ) of the honeycomb lattice. In the first (kinetic) term of the Hamiltonian (2.8), the sum runs only over sites there are close to each other (first neighbors) and the probability amplitude for this process is quantified by  $t_1$ . For the second term, Haldane envisioned a next-nearest neighbor hopping term that would include a complex phase. The physical origin of this phase might be related to a spin-orbit interaction and it can be seen as a staggered magnetic field, that cancels out throughout the material, but is locally (inside the unit cell) important. In a sense, if an electron follows a closed path within the unit hexagon [see Figure 2.3(a)], it will acquire a complex phase proportional to the flux  $\phi$ , similarly to what happens to an electron in the Aharonov-Bohm effect [42]. The flux is positive  $\phi_{ij} = +\phi$  if the path follows a clockwise motion and is negative otherwise. The last term in the Hamiltonian (2.8) is a "mass term", that provides opposite on-site energies for the two different (triangular) sublattices.

The Hamiltonian (2.8) can be easily diagonalized by a Fourier transformation followed by a canonical transformation (see Section 3.1.1 for details) and the resulting electronic spectrum can be very different depending on the model parameters. Figure 2.4(a) shows the electronic bands for  $t_2 = 0$  and  $M = 0$ . We can see that at half-filling, the system has conducting behavior, i.e., it is metallic or in the case of graphene, it is called a zero gap semiconductor. Furthermore, at the points  $K$  and  $K'$  of the first Brillouin zone, the lower and upper bands touch each other, defining a Dirac point. Interestingly, in the vicinity of these points, the electronic band structure has a linear dispersion, resembling the linear dispersion of the Dirac model for relativistic free electrons. Now, if the parameter  $M$  is kept at zero and  $t_2$  is increased, time-reversal symmetry is broken. This will dissolve the Dirac cones, inducing a gap opening in the electronic spectrum as shown in Figure 2.4(b). In this scenario, at half-filling, the resulting electronic spectrum yields an insulating behavior. What was noticed by Haldane is that the Hall conductivity for this set of model

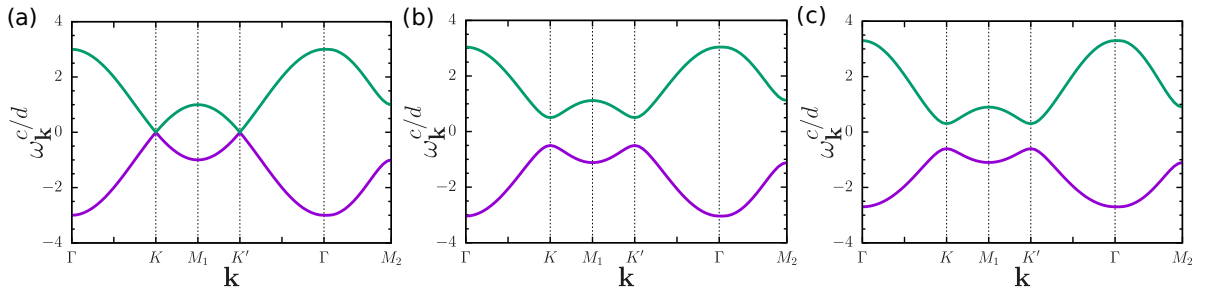


**Figure 2.4:** Electronic band structure of Haldane model (2.8) along particular directions within the Brillouin zone [Fig. 2.3(b)], for different configurations at half-filling. (a) A metallic phase for  $t_2 = 0$  and  $M = 0$ , (b) a topological nontrivial phase for  $t_2 \neq 0$  and  $M = 0$ , and (c) a trivial insulating phase with  $t_2 = 0$  and  $M \neq 0$ . All curves were calculated for  $\phi = \pi/3$ .

parameters was finite and quantized, i.e.,

$$\sigma_{xy} = \frac{e^2}{h}, \quad (2.9)$$

even without external sources of magnetic field. Comparing this result with Eq. (2.5) implies that the bands are topologically nontrivial and that the filled band possesses a Chern number equal to 1 [9]. Additionally, if the sign of the flux  $\phi$  is reversed, that is,  $\phi \rightarrow -\phi$ , the Chern number of the bands would be reversed, being  $-1$  to the lower band and  $+1$  to the upper band, thus reversing also the sign in the Hall conductivity (2.3). Lastly, if  $t_2 = 0$  and  $M$  is finite, the Hamiltonian (2.8) breaks inversion symmetry while keeping time-reversal symmetry. The break of the inversion symmetry also removes the Dirac points and introduces a gap between the electronic bands, driving the system to an insulating phase [Fig. 2.4(c)]. However, in this configuration, the system has zero Hall conductivity ( $\sigma_{xy} = 0$ ), which implies that the bands have zero Chern numbers, i.e., the electronic bands are topologically trivial.

The phase diagram  $M/t_2$  vs  $\phi$  of the Haldane model (2.8) is presented in Figure 2.5. It is important to notice that the Chern number assume only integer values, and a transition from a phase with finite Chern numbers to zero ones is accompanied by a closing in the gap between the filled and the empty bands. Such a transition is characterized by the sinusoidal curve

$$|M/t_2| = 3\sqrt{3} |\sin \phi|, \quad (2.10)$$

which is also showed in the phase diagram in Fig. 2.5. These characteristics are a general rule for Chern and topological insulators [2].

To summarize, Haldane model showed that a quantum Hall effect could in principle be realized in special insulating materials without the need of external magnetic fields. Nowadays, we say that Haldane model is the first example of a Chern insulator, a class of insulators that posses topological bands identified by an integer Chern number,  $C_n \in \mathbb{Z}$  [2, 10].

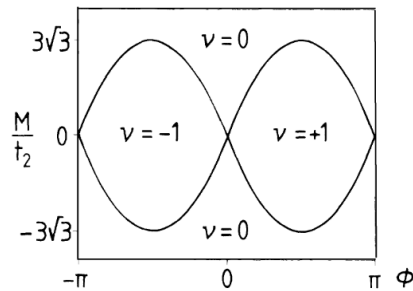


**Figure 2.5:** Phase diagram of the model (2.8), characterizing the trivial phases ( $\nu = 0$ ) and the topological phases ( $\nu = \pm 1$ ) as a function of the model parameters. The solid lines are delimited by Eq. (2.10). Figure extracted from Ref.[5].

### 2.3.2 Kane and Mele model: $Z_2$ topological insulator

Kane and Mele [7] showed that topological bands could generate a novel quantum spin Hall phase that could be realized in condensed matter systems without the need of external magnetic fields. To reach these conclusions, they considered a spinfull generalization of the model proposed by Haldane, where time-reversal symmetry is preserved. In addition, they also included a term to account for the presence/absence of a mirror symmetry. The Hamiltonian of the Kane and Mele model is given by

$$H = t \sum_{\langle ij \rangle} c_i^\dagger c_j + i\lambda_{SO} \sum_{\langle\langle ij \rangle\rangle} v_{ij} c_i^\dagger s_z c_j + i\lambda_R \sum_{\langle ij \rangle} c_i^\dagger (\mathbf{s} \times \hat{\mathbf{d}}_1)_z c_j + \lambda_\nu \sum_i \xi_i c_i^\dagger c_i, \quad (2.11)$$

where  $v_{ij} = (2/\sqrt{3})(\hat{\mathbf{d}}_1 \times \hat{\mathbf{d}}_2)_z = \pm 1$ , with  $\hat{\mathbf{d}}_1$  being the unit lattice vectors that connects the sites  $i$  and  $j$  of the same sublattice on a honeycomb lattice,  $s_z$  is the a Pauli matrix representing the electron spin. Here the spin indices of the fermions operators  $c_i(c_i)^\dagger$  are suppressed. Moreover,  $\lambda_R$  is the Rashba coupling strength, where  $\mathbf{s} \times \hat{\mathbf{d}}$  represents the interaction between local moments with spin  $\mathbf{s}$  and the conduction electrons. In the last term, we have  $\lambda_\nu$  representing an on-site energy with  $\xi_i = -1, +1$ . The physical interpretation of each term of the Hamiltonian (2.11) is as follows. The first term describes nearest-neighbor hopping, the second term is a spin-orbit interaction, the third one is a Rashba type of interaction, and the last term is exactly the mass term (2.8) written with other letters. In particular, if the Rashba term is neglected, the Hamiltonian (2.11) preserves the total spin component  $S_z$  and it is possible to show that it reduces to two independent copies of the Haldane model with  $\phi = \pi/2$ , one for each spin degree of freedom.

The electronic band spectrum of the Hamiltonian (2.11) was numerically calculated for a finite size lattice (zig-zag graphene), yielding four bulk and four edge bands as shown in Figure 2.6. One sees that the bands form two distinct patterns for different model parameters, thus characterizing two distinct insulating phases at half-filling. In

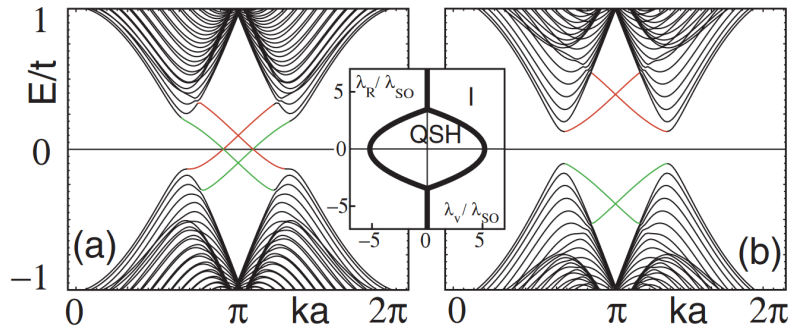


**Figure 2.6:** Numerically calculated electronic spectrum for a finite zigzag graphene sheet (  $\sim 400$  sites ) using model (2.11). In the left panel, the bands for the topological phase and in the right panel for the trivial insulator. A small phase diagram showing the extent of the topological (quantum spin Hall) phase is drawn at the center. Extracted from Ref.[3].

one of the phases, the edge states do not cross the (bulk) gap while, for the other, two pair of edge states connect the valence band and the conduction band. The presence of the edges states in the later case implies the existence of conducting channels at the border of the zig-zag ribbon, which is related to the quantum Hall effect presented in Haldane model. However, the calculation of the Chern number of the half-filled valence bands yields  $C_n = C_n^\downarrow + C_n^\uparrow = 0$ , i.e., although the bands are topologically nontrivial, the quantum Hall conductivity vanishes. Nevertheless, because of the intrinsic topological nature, it was stated that a nontrivial insulating phase is realized, one that should be classified by a different topological invariant. Indeed, although the total Chern number vanishes, the spin Chern number, which is defined as

$$\nu = C_n^\downarrow - C_n^\uparrow, \quad (2.12)$$

for systems that conserve the total spin component  $S_z$ , was found to be nonzero. Therefore, at half-filling, their model describes an insulating system that presents a finite spin Hall conductance. Later in the paper [3], Kane and Mele showed that a  $Z_2$  index could be defined in terms of the Bloch wave functions [analogous to Eqs. (2.5) and (2.6)] and that it would completely distinguish the topological and trivial insulators. Finally, the two phases can not be adiabatically connected, i.e., the band gap between the conduction and valence bands must close as the model parameters vary and the system changes from a topological insulating phase to a trivial one.

### 2.3.3 General concepts of topological band theory

As seen in the two previous sections, topological insulators in 2D follow two fundamental rules: (1) There is a number, called topological invariant, that assumes only integer numbers (  $C_n \in Z$  for the Chern insulator and  $\nu = 0$  and 1 for the  $Z_2$  topological insu-

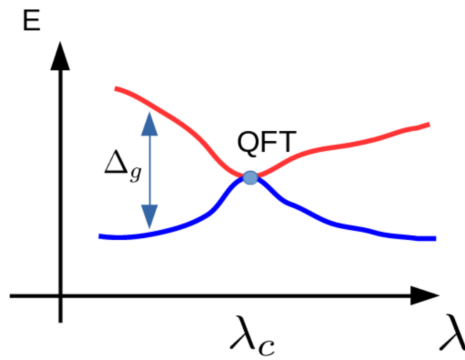


**Figure 2.7:** Evolution of the gap  $\Delta_g$  between the valence (blue) and conduction (red) bands as a function of a set of parameter  $\lambda = \lambda_1, \lambda_2, \dots$  that modifies a Hamiltonian  $H(\mathbf{k}, \lambda_1, \lambda_2, \dots)$ . A quantum phase transition occurs at the gap closure, allowing the topological invariant to change its value.

lator) that fully distinguishes the topological insulating phase from the trivial insulating phase; (2) there must be a gap closure between the valence and conduction bands for the system to transit between topologically distinct phases. These two features are general and apply to topological insulator in one, two and three dimensions [1, 3, 7, 14, 41].

The topological invariant determines a topological class that is composed of Hamiltonians that are adiabatically connected to one another. This adiabatic connection can be understood as follows: Consider a Hamiltonian  $H(\mathbf{k}, \lambda_1, \lambda_2, \dots)$  that can be tuned via a set of parameters  $\lambda_i$ ; if, and only if, the resulting energy spectrum for each configuration of the parameters  $\lambda_i$  is smoothly deformed and the band gap between the valence and conduction band remains, the Hamiltonians are said to be connected. Figure 2.7 schematically shows how the gap between the bottom of the conduction band and the top of the valence band evolves as the set of parameters  $\lambda_i$  is varied. At the point where the gap closes, a quantum phase transition occurs, allowing the topological invariant to change its value. An immediate parallel can be made with the mathematical concept of topological closed surfaces, where two surfaces are said to belong to the same topological class if they can be continuous deformed into one another without "violent changes" in their curvature, i.e., no new holes are made or destroyed in the process. Using this concept, it is possible to defined a trivial insulator as an insulator that can be adiabatically connect to the atomic insulator limit, in which the electron shells are closed and tightly bound to the atoms, implying that the electronic bands are discretely separated. Otherwise, the system is said to be a topological insulator [38].

## 2.4 Tight-binding models with topologically nontrivial flat bands

As seen in the previous section, the topological band theory [1, 2] allows for a better understanding of the physics behind the topological insulators. In particular, the concept of adiabatically connected Hamiltonians allows us to search for tight-binding models, whose parameters can be fine tuned such that the model displays (nearly) flat bands while maintaining its topological properties [18, 19]. Below, we briefly discuss the key points about these models and how flat bands can be obtained in these systems.

### 2.4.1 Spinless models

To discuss a little bit the features of these models, we follow the chronological order, and therefore, start by reviewing a model on a checkerboard lattice proposed by Ref. [19].

The Hamiltonian of the spinless model proposed by Ref. [19] has a similar form as the one in Eq. (2.8), i.e.,

$$H = -t \sum_{\langle i,j \rangle} e^{i\phi_{i,j}} (c_i^\dagger c_j + H.c.) - \sum_{\langle\langle i,j \rangle\rangle} t'_{ij} (c_i^\dagger c_j + H.c.) - t'' \sum_{\langle\langle\langle i,j \rangle\rangle\rangle} (c_i^\dagger c_j + H.c.), \quad (2.13)$$

where  $t$ ,  $t'_{ij}$  and  $t''$  are the nearest-neighbor, next-nearest-neighbor, and next-next-nearest-neighbor hopping amplitudes, respectively. A complex phase factor  $\phi_{i,j} = \pm\phi$  appears in the first term, whose sign is given by the direction of the nearest-neighbor hopping, as shown in Fig. 2.8(a). Also,  $t'_{ij}$  can be equal either to  $t'_1$  or  $t'_2$  depending on whether the sites are connected by solid or dashed lines. In momentum space, the Hamiltonian (2.13) can be written as

$$H = - \sum_{\mathbf{k}} \Psi_{\mathbf{k}}^\dagger \mathcal{H}_{\mathbf{k}} \Psi_{\mathbf{k}}, \quad (2.14)$$

where  $\Psi_{\mathbf{k}}^\dagger = (a_{\mathbf{k}}^\dagger, b_{\mathbf{k}}^\dagger)$  and the Bloch Hamiltonian  $\mathcal{H}_{\mathbf{k}}$  is given by

$$\begin{aligned} \mathcal{H}_{\mathbf{k}} = & [(t'_1 + t'_2)(\cos k_x + \cos k_y) + 4t'' \cos k_x \cos k_y] \mathcal{I} + 4t \cos \phi \left( \cos \frac{k_x}{2} \cos \frac{k_y}{2} \right) \sigma_x \\ & + 4t \sin \phi \left( \sin \frac{k_x}{2} \sin \frac{k_y}{2} \right) \sigma_y + (t'_1 - t'_2)(\cos k_x - \cos k_y) \sigma_z. \end{aligned} \quad (2.15)$$

Due to the fact that (2.15) is written in terms of the identity matrix  $\mathcal{I}$  and the vector of Pauli matrices  $\vec{\sigma} = (\sigma_x, \sigma_y, \sigma_z)$  in the form

$$\mathcal{H}_{\mathbf{k}} = h_{\mathbf{k}}^0 \mathcal{I} + \vec{h}_{\mathbf{k}} \cdot \vec{\sigma}, \quad (2.16)$$

where  $\vec{h}_{\mathbf{k}} = (h_{\mathbf{k}}^x, h_{\mathbf{k}}^y, h_{\mathbf{k}}^z)$ , the spectrum is well known (see Sec.3.1.1) and follows directly

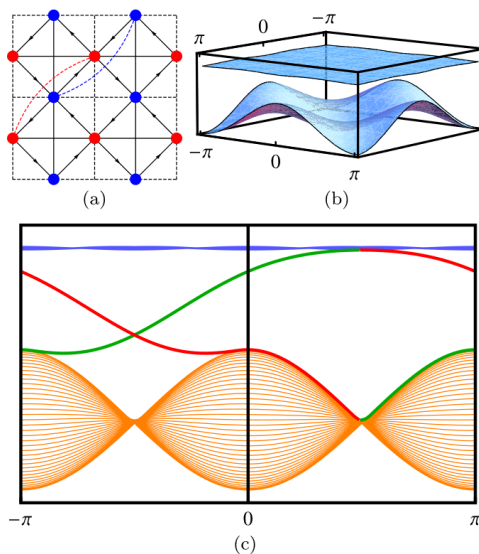


**Figure 2.8:** In panel (a), a schematic representation of the Hamiltonian (2.13) on a checkerboard lattice. The electronic spectrum with a flat band is shown in (b), while a projection of the same spectrum calculated for a finite size system is shown in panel (c), with the red and green lines representing the chiral (counter-propagating) edge states. Figure adapted from Ref. [19].

as

$$\omega_{\mathbf{k}}^{\pm} = h_{\mathbf{k}}^0 \pm \sqrt{h_{\mathbf{k}}^x{}^2 + h_{\mathbf{k}}^y{}^2 + h_{\mathbf{k}}^z{}^2}. \quad (2.17)$$

In general, the electronic spectrum (2.17) of the model (2.15) does not present flat bands. However, the bands can be made flat by fine tuning the hopping parameters  $t$ ,  $t'_1$ ,  $t'_2$  and  $t''$ . To find the optimal parameters, it was imposed that the higher energy band should obey

$$\omega_{\Gamma} = \omega_M = \omega_X = \omega_{(\pi/2, \pi/2)}, \quad (2.18)$$

where  $\Gamma = (0, 0)$ ,  $M = (\pi, \pi)$ ,  $X = (\pi, 0)$ . Such procedure provides a nonlinear system of equations for  $t$ ,  $t'_1$ ,  $t'_2$ ,  $t''$ , and  $\phi$  that can be solved to yield flat electronic bands. For example, setting  $t_1 = 1$  and  $\phi = \pi/4$ , flat electronic bands can be obtained once  $t'_1 = -t'_2 = 1/(2 + \sqrt{2})$  and  $t'' = 1/(2 + 2\sqrt{2})$ . Figure 2.8(b) shows such spectrum for these optimal parameters, where we can see that the upper band becomes almost dispersionless with a bandwidth of 1/30 of the band gap. Additionally, the bands were found to be topologically nontrivial as the Chern number of each of the two bands were found to be equal to  $\pm 1$ . The topological properties were also confirmed by the diagonalization of the Hamiltonian (2.13) in a finite size system for the same set of optimal flatness parameters. The obtained spectrum presented edge states connecting the lower and upper bands. Such conducting edges can be seen in the projected spectrum in Fig. 2.8(c), with the red/green lines representing the modes on each sample border.

A similar model for the square lattice showing topologically nontrivial flat bands was also discussed in the same year in a paper by Neupert *et al.* [18]. Although their model differ a bit from the one proposed in Ref.[19], since it includes only first and second

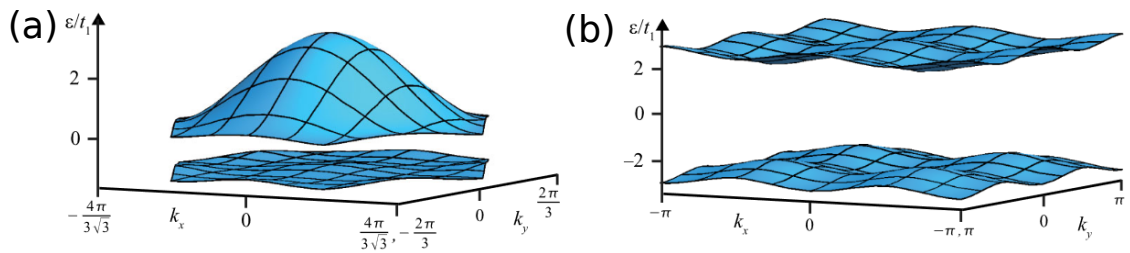


**Figure 2.9:** Free electronic band structure for (a) the Haldane model (2.8) on a honeycomb lattice and (b) for the  $\pi$ -flux model on a square lattice discussed in Ref. [18], both corresponding to the nearly flat band limit. Figure adapted from Ref. [18].

neighbor hoppings, the results were qualitatively the same, i.e., it is possible to find configurations with quite well separated electronic bands with very low dispersion when compared to the band gap. Figure 2.9(b) shows the respective optimal flatness limit of the electronic spectrum.

Neupert *et al.* [18] also discussed how flat bands can also be obtained in the Haldane model (2.8) [5]. They noticed that both the band gap and the band dispersions could be changed by adjusting the next-nearest-neighbor hopping amplitude  $t_2$  and the flux  $\phi$  [see Eq. (2.8)]. In this case, the choice  $\cos \phi = t_1/(4t_2)$  gives the maximum value for the flatness ratio of the lower (-) band, i.e., the ratio  $f_-$  is written as

$$f_- = \frac{\Delta}{W_-}, \quad (2.19)$$

where  $\Delta = \min(\omega_{\mathbf{k}}^+) - \max(\omega_{\mathbf{k}}^-)$  is the band gap and  $W_- = \max(\omega_{\mathbf{k}}^-) - \min(\omega_{\mathbf{k}}^-)$  is the bandwidth of the lower band. Although not stated in their paper, this optimal parameter choice can also be obtained by imposing that two points in the first Brillouin zone have the same energy. For example, matching the values of  $\omega_{\Gamma} = \omega_M$ , would yield a nonlinear system of equations that can be solved giving the optimal relation. Figure 2.9.(a) shows the electronic band structure of the Haldane model (2.8) for this optimal parameters choice, where we can see that the lower band of the model on a honeycomb lattice becomes almost flat.

## 2.4.2 Spinfull models

The extension for spinfull Hamiltonians was also considered in the literature [20, 21, 24]. For example, Doretto and Goerbig [24] have included the spin degree of freedom in the square lattice  $\pi$ -flux model discussed by Neupert *et al.* in Ref. [18]. They also have shown that the spin degree of freedom could be included in two ways: breaking or preserving time-reversal symmetry. In the first case, the model describes a Chern insulator while in the later it describes a  $Z_2$  topological insulator, both at half filling of the free-electronic

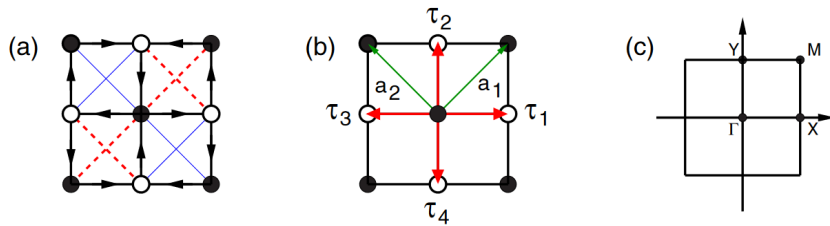


**Figure 2.10:** In (a), a schematic representation of the Hamiltonian (2.20) on a square lattice is shown. Solid black lines and its directions indicate the positive  $t_1 \exp(i\pi/4)$  hopping (for spin- $\uparrow$  electrons). The dashed red and solid blue connections indicates that the next-nearest-neighbor hopping amplitude is equal to  $+t_2$  and  $-t_2$  respectively. The lattice vectors are represented in (b), where  $\mathbf{a}_1 = a\hat{x}$  and  $\mathbf{a}_2 = a\hat{y}$ . In (c), we have the first Brillouin zone with its high symmetry points. Figure from Ref. [24].

bands.

To understand these concepts, we start by stating the square lattice  $\pi$ -flux model spinfull Hamiltonian,

$$H_0 = \sum_{i \in A, \tau, \sigma} (t_{i, i+\tau, \sigma} c_{iA\sigma}^\dagger c_{i+\tau B\sigma} + H.c.) + \sum_{i, \delta, a, \sigma} (\lambda_{i, i+\delta} c_{ia\sigma}^\dagger c_{i+\delta a\sigma} + H.c.), \quad (2.20)$$

where  $\sigma = \uparrow, \downarrow$  labels the electron spin and  $a = A, B$  the sublattice. Furthermore, the nearest-neighbor hopping is spin dependent and is given by

$$t_{i, i+\tau, \sigma} = t_1 \exp[i(-1)^\tau \gamma(\sigma) \pi/4], \quad (2.21)$$

while the next-nearest-neighbor one depends on the sublattice index

$$\lambda_{i, i+\delta} = \begin{cases} -(-1)^\delta t_2, & i \in A \\ +(-1)^\delta t_2 & i \in B \end{cases}, \quad (2.22)$$

with  $t_1$  and  $t_2$  being positive.  $\gamma(\sigma)$  is a factor that can be equal to  $\pm 1$  depending on the electron spin (see discussion bellow). Finally, the indices  $\tau = 1, 2, 3, 4$  and  $\delta = 1, 2$  are related to the lattice vectors connecting a site to its nearest- and next-nearest-neighbors. A schematic representation of the model (2.20) and the nearest- and next-nearest-neighbors vectors  $\tau$  and  $\delta$  are shown in Figs. 2.10(a) and (b), respectively.

In momentum space, the Hamiltonian (2.20) assumes the form

$$H = \sum_{\mathbf{k}} \Psi_{\mathbf{k}}^\dagger \mathcal{H}_{\mathbf{k}} \Psi_{\mathbf{k}},$$

where now the spinor is given by  $\Psi_{\mathbf{k}}^\dagger = (c_{\mathbf{k}A\uparrow}^\dagger, c_{\mathbf{k}B\uparrow}^\dagger, c_{\mathbf{k}A\downarrow}^\dagger, c_{\mathbf{k}B\downarrow}^\dagger)$  and

$$\mathcal{H}_{\mathbf{k}} = \begin{pmatrix} h_{\mathbf{k}}^\uparrow & 0 \\ 0 & h_{\mathbf{k}}^\downarrow \end{pmatrix}_{4 \times 4}. \quad (2.23)$$

Each spin sector in the Hamiltonian (2.23) can be written in terms of the Pauli and the identity matrices as  $h_{\mathbf{k}}^\sigma = B_{0,\mathbf{k}}\mathcal{I} + \vec{B}_{\mathbf{k}} \cdot \vec{\sigma}$ , with the coefficients given by

$$\begin{aligned} B_{0,\mathbf{k}} &= 0, \\ B_{1,\mathbf{k}} &= 2\sqrt{2}t_1 \cos \frac{k_x}{2} \cos \frac{k_y}{2}, \\ B_{2,\mathbf{k}}^\sigma &= 2\sqrt{2}t_1\gamma(\sigma) \sin \frac{k_x}{2} \sin \frac{k_y}{2}, \\ B_{3,\mathbf{k}} &= 2t_2(\cos k_x - \cos k_y). \end{aligned} \quad (2.24)$$

From this point, an analysis of the time-reversal symmetry (TRS) of the Hamiltonian can be made. If the commutation relation  $[\mathcal{H}_{\mathbf{k}}, \mathcal{T}] = 0$  is to be enforced, the Hamiltonian will be time reversal symmetric with the following relation between the spin sectors  $h_{\mathbf{k}}^\uparrow = (h_{-\mathbf{k}}^\downarrow)^*$ . This implies that  $\gamma(\uparrow) = -\gamma(\downarrow) = 1$  for the time-reversal symmetric case. On the other hand, when TRS is broken,  $h_{\mathbf{k}}^\uparrow = h_{\mathbf{k}}^\downarrow$ , implying that  $\gamma(\uparrow) = \gamma(\downarrow) = 1$ . Interestingly, the free-electronic spectrum is the same for both the time-reversal symmetric case and the one where TRS is broken. Similarly to Eq. (2.17), the electronic spectrum follows from the expansion coefficients (2.24) and can be readily calculated. Figure 2.11 shows the electronic spectrum  $\omega_{c/d,k}$ , for the Chern insulator, where the band gap and the flatness of the bands are altered by the tuning of parameter  $t_2$ , reaching gapped and nearly flat bands for  $t_2 = 1/\sqrt{2}t_1$ . This value coincides with the value found in Ref. [18]. Again,

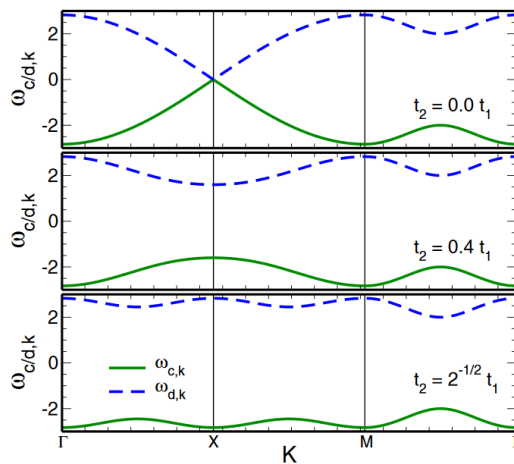


**Figure 2.11:** Electronic spectrum of the free Hamiltonian (2.20) for different values of  $t_2$  in paths along the first Brillouin zone [Fig. 2.10(c)]. As  $t_2$  is increased, a band gap develops and the band dispersion modifies becoming almost flat for  $t_2 = 1/\sqrt{2}t_1$ . Figure adapted from Ref.[24].

in the optimal flatness limit, the electron dispersion energy is the same for the highly symmetric momenta  $\Gamma$ ,  $X$  and  $M$ .

# Chapter 3

## Topological flat-band ferromagnetism

Here we combine the ideas of the previous chapter, more specifically, we follow the lines of Ref.[24] for the spinfull square lattice  $\pi$ -flux model and consider the spinfull Haldane model on a honeycomb lattice. We show in details that the model supports topologically nontrivial and nearly flat electronic bands. This model will be the basis for the developments in the next chapters, where it will be considered for the description of a Chern and a topological insulators on a honeycomb lattice. This chapter is heavily based on Refs. [34] and [35].

### 3.1 Spinfull Haldane model : Chern insulator

#### 3.1.1 Electronic bands and the nearly flat-band limit

Following Ref. [24], we generalize the Haldane model (2.8) on a honeycomb lattice for a system of  $N_e$  spin-1/2 electrons,

$$\begin{aligned}
 H_0 = & t_1 \sum_{i \in A, \delta, \sigma} \left( c_{iA\sigma}^\dagger c_{i+\delta B\sigma} + \text{H.c.} \right) \\
 & + t_2 \sum_{i \in A, \tau, \sigma} \left( e^{-i\phi} c_{iA\sigma}^\dagger c_{i+\tau A\sigma} + \text{H.c.} \right) \\
 & + t_2 \sum_{i \in B, \tau, \sigma} \left( e^{+i\phi} c_{iB\sigma}^\dagger c_{i+\tau B\sigma} + \text{H.c.} \right). \tag{3.1}
 \end{aligned}$$

Here the operator  $c_{ia\sigma}^\dagger$  ( $c_{ia\sigma}$ ) creates (destroys) an electron with spin  $\sigma = \uparrow, \downarrow$  on site  $i$  of the (triangular) sublattice  $a = A, B$  of the honeycomb lattice.  $t_1 \geq 0$  and  $t_2 e^{\pm i\phi}$  with  $t_2 \geq 0$  are, respectively, the nearest-neighbor and next-nearest-neighbor hoppings. One notices that the electron acquires a  $+\phi$  ( $-\phi$ ) phase as it moves in the same (opposite) direction of the arrows within the same sublattice [see dashed lines in Fig. 3.1(a)]. Indeed, the complex next-nearest-neighbor hopping  $t_2 e^{\pm i\phi}$  results in a fictitious flux pattern with zero

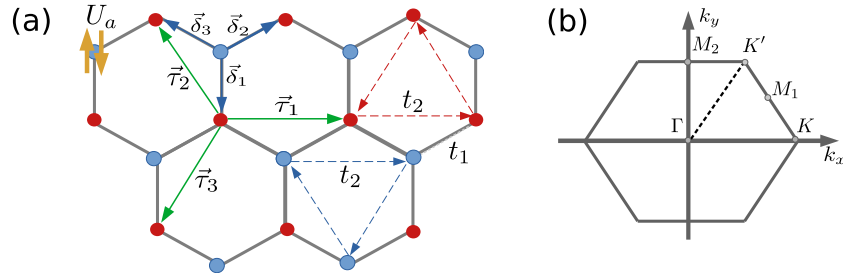


**Figure 3.1:** (a) Schematic representation of the Haldane model (3.1) on the honeycomb lattice, indicating the nearest-neighbor  $t_1$  and next-nearest-neighbor  $t_2 e^{\pm i\phi}$  hoppings. An on-site Hubbard repulsion energy  $U_a$  that will be added to the model latter is also shown. Blue and red circles indicate the sites of the (triangular) sublattices  $A$  and  $B$ , respectively.  $\delta_i$  and  $\tau_i$  are the nearest-neighbor (3.2) and next-nearest-neighbor (3.3) vectors, respectively. (b) The first Brillouin zone and its highly symmetric points:  $\mathbf{K} = (4\pi/3\sqrt{3}, 0)$ ,  $\mathbf{K}' = (2\pi/3\sqrt{3}, 2\pi/3)$ ,  $\mathbf{M}_1 = (\pi/\sqrt{3}, \pi/3)$ , and  $\mathbf{M}_2 = (0, 2\pi/3)$ . The nearest-neighbor distance of the honeycomb lattice  $a = 1$ .

net flux per unit cell [see, e.g, Fig. 1(a) in Ref. [18] for details]. The index  $\delta$  corresponds to the nearest-neighbor vectors [Fig. 3.1(a)]

$$\begin{aligned} \delta_1 &= -a\hat{y}, \\ \delta_2 &= \frac{a}{2} (\sqrt{3}\hat{x} + \hat{y}), \quad \delta_3 = -\frac{a}{2} (\sqrt{3}\hat{x} - \hat{y}), \end{aligned} \quad (3.2)$$

while  $\tau$  indicates the next-nearest-neighbor vectors

$$\begin{aligned} \tau_1 &= \delta_2 - \delta_3 = a\sqrt{3}\hat{x}, \\ \tau_2 &= \delta_3 - \delta_1 = -\frac{a}{2} (\sqrt{3}\hat{x} - 3\hat{y}), \\ \tau_3 &= \delta_1 - \delta_2 = -\frac{a}{2} (\sqrt{3}\hat{x} + 3\hat{y}). \end{aligned} \quad (3.3)$$

In the following, we set the nearest-neighbor distance to unit, i.e.,  $a = 1$ .

The first step to diagonalize the tight-binding Hamiltonian (3.1), and find the corresponding electronic spectrum, is to perform a Fourier transform,

$$c_{ia\sigma}^\dagger = \frac{1}{\sqrt{N_a}} \sum_{\mathbf{k} \in \text{BZ}} e^{-i\mathbf{k} \cdot \mathbf{R}_i} c_{\mathbf{k}a\sigma}^\dagger, \quad (3.4)$$

where the momentum sum runs over the first Brillouin zone (BZ) [Fig. 3.1(b)] associated with the underlying triangular Bravais lattice and  $N_a = N$  is the number of sites of the sublattice  $a$ . It is then easy to show that the noninteracting Hamiltonian (3.1) can be written in a matrix form,

$$H_0 = \sum_{\mathbf{k}} \Psi_{\mathbf{k}}^\dagger H_{\mathbf{k}} \Psi_{\mathbf{k}}, \quad (3.5)$$

where the  $4 \times 4$   $H_{\mathbf{k}}$  matrix reads

$$H_{\mathbf{k}} = \begin{pmatrix} h_{\mathbf{k}}^{\uparrow} & 0 \\ 0 & h_{\mathbf{k}}^{\downarrow} \end{pmatrix} \quad (3.6)$$

and the four-component spinor  $\Psi_{\mathbf{k}}$  is given by

$$\Psi_{\mathbf{k}} = (c_{\mathbf{k}A\uparrow} \ c_{\mathbf{k}B\uparrow} \ c_{\mathbf{k}A\downarrow} \ c_{\mathbf{k}B\downarrow})^T. \quad (3.7)$$

The  $2 \times 2$  matrices  $h_{\mathbf{k}}^{\sigma}$  associated with each spin sector are such that  $h_{\mathbf{k}}^{\uparrow} = h_{\mathbf{k}}^{\downarrow} = h_{\mathbf{k}}$ , with the  $h_{\mathbf{k}}$  matrix given by

$$h_{\mathbf{k}} = \begin{pmatrix} 2t_2 \sum_{\tau} \cos(\mathbf{k} \cdot \boldsymbol{\tau} + \phi) & t_1 \sum_{\delta} e^{i\mathbf{k} \cdot \boldsymbol{\delta}} \\ t_1 \sum_{\delta} e^{-i\mathbf{k} \cdot \boldsymbol{\delta}} & 2t_2 \sum_{\tau} \cos(\mathbf{k} \cdot \boldsymbol{\tau} - \phi) \end{pmatrix}. \quad (3.8)$$

It is possible to write the  $h_{\mathbf{k}}$  matrix in terms of the identity matrix  $\tau_0$  and the vector  $\hat{\boldsymbol{\tau}} = (\tau_1, \tau_2, \tau_3)$ , whose components are Pauli matrices. Thus, the  $h_{\mathbf{k}}$  matrix reads

$$h_{\mathbf{k}} = B_{0,\mathbf{k}}\tau_0 + \mathbf{B}_{\mathbf{k}} \cdot \hat{\boldsymbol{\tau}}, \quad (3.9)$$

where the  $B_{0,\mathbf{k}}$  function and the components of the vector  $\mathbf{B}_{\mathbf{k}} = (B_{1,\mathbf{k}}, B_{2,\mathbf{k}}, B_{3,\mathbf{k}})$  are given by

$$\begin{aligned} B_{0,\mathbf{k}} &= 2t_2 \cos(\phi) \sum_{\tau} \cos(\mathbf{k} \cdot \boldsymbol{\tau}), \\ B_{1,\mathbf{k}} &= t_1 \sum_{\delta} \cos(\mathbf{k} \cdot \boldsymbol{\delta}), \\ B_{2,\mathbf{k}} &= t_1 \sum_{\delta} \sin(\mathbf{k} \cdot \boldsymbol{\delta}), \\ B_{3,\mathbf{k}} &= -2t_2 \sin(\phi) \sum_{\tau} \sin(\mathbf{k} \cdot \boldsymbol{\tau}), \end{aligned} \quad (3.10)$$

with the indices  $\delta$  and  $\tau$  corresponding to the nearest-neighbor (3.2) and next-nearest-neighbor (3.3) vectors, respectively. The fact that the matrices  $h_{\mathbf{k}}^{\sigma}$  related to each spin sector  $h_{\mathbf{k}}^{\uparrow} = h_{\mathbf{k}}^{\downarrow} = h_{\mathbf{k}}$  indicates that the noninteracting model (3.1) breaks time-reversal symmetry (see also the discussion for the  $Z_2$  topological insulator in Sec.3.2). The Hamiltonian (3.5) can now be diagonalized via the canonical transformation

$$\begin{aligned} d_{\mathbf{k}\sigma} &= u_{\mathbf{k}}c_{\mathbf{k}A\sigma} + v_{\mathbf{k}}c_{\mathbf{k}B\sigma}, \\ c_{\mathbf{k}\sigma} &= v_{\mathbf{k}}^*c_{\mathbf{k}A\sigma} - u_{\mathbf{k}}^*c_{\mathbf{k}B\sigma}, \end{aligned} \quad (3.11)$$

where the coefficients  $u_{\mathbf{k}}$  and  $v_{\mathbf{k}}$  are given by

$$\begin{aligned} |u_{\mathbf{k}}|^2 &= \frac{1}{2} \left( 1 + \hat{B}_{3,\mathbf{k}} \right), & |v_{\mathbf{k}}|^2 &= \frac{1}{2} \left( 1 - \hat{B}_{3,\mathbf{k}} \right), \\ u_{\mathbf{k}}v_{\mathbf{k}}^* &= \frac{1}{2} \left( \hat{B}_{1,\mathbf{k}} + i\hat{B}_{2,\mathbf{k}} \right), \end{aligned} \quad (3.12)$$

with the hatted  $B_{i,\mathbf{k}}$  standing for the  $i$ -component of the normalized vector  $\hat{\mathbf{B}}_{\mathbf{k}} = \mathbf{B}_{\mathbf{k}}/|\mathbf{B}_{\mathbf{k}}|$ . After the diagonalization, the Hamiltonian (3.5) then reads

$$H_0 = \sum_{\mathbf{k}\sigma} \omega_{\mathbf{k}}^c c_{\mathbf{k}\sigma}^\dagger c_{\mathbf{k}\sigma} + \omega_{\mathbf{k}}^d d_{\mathbf{k}\sigma}^\dagger d_{\mathbf{k}\sigma}, \quad (3.13)$$

with the dispersions of the lower band  $c$  ( $-$  sign) and the upper one  $d$  ( $+$  sign) given by

$$\omega_{\mathbf{k}}^{d/c} = B_0 \pm \sqrt{B_{1,\mathbf{k}}^2 + B_{2,\mathbf{k}}^2 + B_{3,\mathbf{k}}^2}. \quad (3.14)$$

Notice that both  $c$  and  $d$  free-electronic bands are doubly degenerated with respect to the spin degree of freedom. Figure 3.2(a) shows the electronic bands (3.14) along paths in the first Brillouin zone [Fig. 3.1(b)] for two different parameter sets. For  $t_2 = 0.3155 t_1$  and  $\phi = 0$ , the spectrum is gapless due to the presence of Dirac points at the  $K$  and  $K'$  points, i.e., the upper and lower bands touch at these points and the bands disperse linearly with momentum around them. A finite phase  $\phi$  breaks time-reversal symmetry and opens a gap  $\Delta$  between the lower and upper bands at the  $K$  and  $K'$  points, as exemplified for the parameter choice  $t_2 = 0.3155 t_1$  and  $\phi = 0.656$ .

Interestingly, a finite phase  $\phi$  yields topologically nontrivial free-electronic bands, since

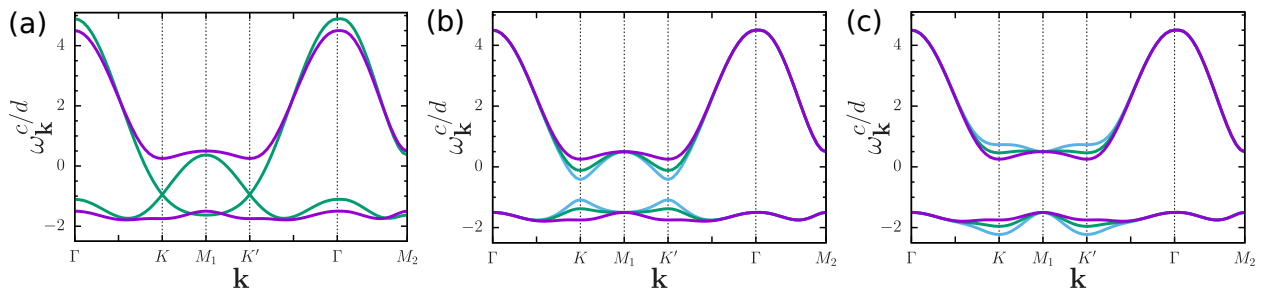


**Figure 3.2:** Band structure (3.14) of the noninteracting hopping term (3.1) (in units of the nearest-neighbor hopping amplitude  $t_1$ ) along paths in the first Brillouin zone [Fig. 3.1(b)] for different values of the next-nearest-neighbor hopping amplitude  $t_2$  and phase  $\phi$ : (a)  $t_2 = 0.3155 t_1$ ,  $\phi = 0$  (green) and  $t_2 = 0.3155 t_1$ ,  $\phi = 0.656$  (magenta); (b)  $\phi = 0.4$  (blue),  $\phi = 0.5$  (green), and  $\phi = 0.656$  (magenta), with  $t_2$  given by the relation  $\cos(\phi) = t_1/(4t_2)$ ; and (c)  $\phi = 0.656$  (magenta)  $\phi = 0.75$  (green), and  $\phi = 0.85$  (blue), with  $t_2$  given by the relation  $\cos(\phi) = t_1/(4t_2)$ .

the corresponding Chern numbers [7, 18]

$$C_\sigma^{c/d} = \pm \frac{1}{4\pi} \int_{BZ} d^2k \hat{\mathbf{B}}_{\mathbf{k}} \cdot (\partial_{k_x} \hat{\mathbf{B}}_{\mathbf{k}} \times \partial_{k_y} \hat{\mathbf{B}}_{\mathbf{k}}), \quad (3.15)$$

are finite. Notice that, when we compare the integrand of Eq. (3.15) with Eq. (2.5) and (2.6), we see that it is proportional to the Berry curvature. Therefore, for this case, the Berry curvature is given by

$$\Omega_{k_x, k_y} = \frac{1}{2} \hat{\mathbf{B}}_{\mathbf{k}} \cdot (\partial_{k_x} \hat{\mathbf{B}}_{\mathbf{k}} \times \partial_{k_y} \hat{\mathbf{B}}_{\mathbf{k}}). \quad (3.16)$$

A plot of the Berry curvature (3.16) for the nearly flat band limit [see Eq. (3.18) below] of the Hamiltonian (3.1) is shown in Fig. 3.3. One sees that the Berry curvature has peaks around the first Brillouin zone corners. The area below the curve was numerically calculated and adds to  $-1$  ( $+1$ ) for the upper (lower) band. For the topologically trivial phase, the Berry curvature is zero everywhere (not shown). Therefore, one finds that, for the topologically nontrivial phase, regardless of the spin,  $C_\sigma^c = +1$  and  $C_\sigma^d = -1$  for the lower and upper bands, respectively. As mentioned in Chapter 2, such nonzero Chern numbers combined with broken time-reversal symmetry indicate that the gapped phase of the noninteracting model (3.1) at half filling is indeed a Chern band insulator [7, 8]. The phase diagram  $t_2/t_1$  v.s.  $\phi$  for the noninteracting model (3.1) at half-filling can be found, e.g., in Ref. [43]: in addition to a (gapped) Chern band insulator phase with quantized Hall conductivity  $\sigma_{xy} = \pm e^2/h$  per spin, the model also displays a Chern metal phase with nonquantized  $\sigma_{xy}$ .

Coming back to the effects of the  $t_2$  and  $\phi$  parameters on the band structure (3.14), we can see in Fig. 3.2(b) how the electronic band structure changes as the parameter  $\phi$  increases ( $\phi = 0.4, 0.5, 0.656$ ) with  $t_2$  given by  $\cos(\phi) = t_1/(4t_2)$ . One notices that, as the phase  $\phi$  increases, the band width of the lower c band, which is defined as  $W_c = \max(\omega_{\mathbf{k}}^c) - \min(\omega_{\mathbf{k}}^c)$ , decreases, while the energy gap between the lower c and upper d

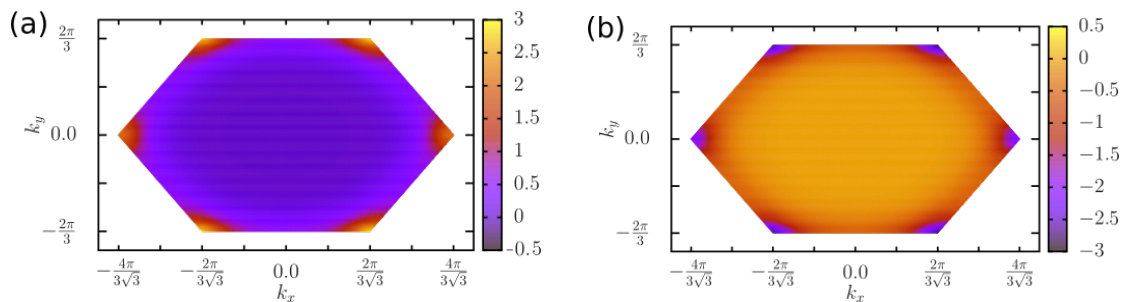


**Figure 3.3:** Contour plot of the Berry curvature (3.16) of the (a) lower and (b) upper electronic bands (3.14) of the Hamiltonian (3.1) at the nearly flat band limit (3.18).

band  $[\Delta = \min(\omega_{d,\mathbf{k}}) - \max(\omega_{c,\mathbf{k}})]$  increases. The flatness ratio (2.19) reads,

$$f_c = \frac{\Delta}{W_c}. \quad (3.17)$$

We can see that, as  $\phi$  increases, the flatness ratio of the lower  $c$  band also increases. Indeed, the parameter choice (nearly flat band limit)

$$t_2 = 0.3155 t_1 \quad \text{and} \quad \phi = 0.656, \quad (3.18)$$

yields the largest flatness ratio,  $f_c = 7$ . Notice that the lower  $c$  band becomes almost flat [see magenta curves in Fig. 3.2(a)-(c)]. The parameter choice (3.18), with  $\cos(\phi) = t_1/(4t_2) = 3\sqrt{3/43}$  agrees with the optimal flatness parameter choice for the Haldane model determined in Ref. [18]. The condition (3.18) will be referred throughout the thesis as the **nearly flat band limit**. Finally, in Fig. 3.2(c), we show the electronic spectrum (3.14) when  $\phi > 0.656$ , i.e.,  $\phi = 0.7, 0.8, 0.9$  and, again,  $t_2$  given by  $\cos(\phi) = t_1/(4t_2) = 3\sqrt{3/43}$ . Note that the width  $W_c$  of the lower band  $c$  increases with  $\phi$ .

### 3.1.2 Mass term

An additional interesting term, that is also present in Haldane's original model [5], is a staggered on-site energy term that breaks inversion symmetry:

$$H_M = M \sum_{i\sigma} \left( c_{iA\sigma}^\dagger c_{iA\sigma} - c_{iB\sigma}^\dagger c_{iB\sigma} \right). \quad (3.19)$$

Adding the staggered on-site energy term (3.19) to the tight-binding model (3.1), one easily finds that the new Hamiltonian  $H_0 + H_M$  also assumes the form (3.5) with the  $B_{0,\mathbf{k}}$  and the  $B_{i,\mathbf{k}}$  ( $i = 1, 2, 3$ ) functions given by Eq. (3.10), apart from the replacement

$$B_{3,\mathbf{k}} \rightarrow B_{3,\mathbf{k}} + M. \quad (3.20)$$

In Fig. 3.4, we plot the band structure (3.14) for the parameters (3.18) and  $M = 0, 0.1, 0.2$ , and  $0.3 t_1$ . We notice that, for a finite on-site energy  $M > 0$  ( $M < 0$ , not shown here), the energy gap is located at the  $K'$  ( $K$ ) point. Moreover, as the parameter  $M$  increases, the energy gap decreases, the difference  $(\omega_{K'}^c - \omega_K^c)$  increases, and the flatness ratio of the lower band  $c$  decreases. Indeed, the increasing of the parameter  $M$  can induce a gap closure that destroys the topological phase, as shown in Fig. 2.5. In Sec. 4.2.3 below, we consider a finite staggered on-site energy  $M$  as a source of departure of the lower band  $c$  from the nearly flat band limit (3.18).

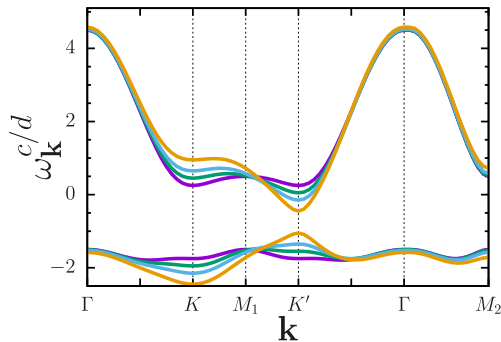


**Figure 3.4:** Band structure (3.14) of the noninteracting hopping term (3.1) with the additional staggered on-site energy term (3.19) (in units of the nearest-neighbor hopping amplitude  $t_1$ ) along paths in the first Brillouin zone for the next-nearest-neighbor hopping amplitude  $t_2 = 0.3155 t_1$ , phase  $\phi = 0.656$ , and staggered on-site energy  $M = 0$  (magenta),  $0.1$  (green),  $0.2$  (blue), and  $0.3 t_1$  (orange).

## 3.2 Spinfull Haldane model with TRS : $Z_2$ topological insulator

### 3.2.1 Time-reversal-symmetric Hamiltonian

One of the key differences between the  $Z_2$  topological insulator and the Chern insulator is that time-reversal symmetry is preserved in the  $Z_2$  topological insulator. To preserve time-reversal symmetry in the Hamiltonian (3.1), the Hamiltonian should commute with the time-reversal operator  $\mathcal{T} = i(\sigma_y \otimes \mathbf{I})K$ , that is, it should satisfy the following relation (see Ref. [24] for details)

$$\mathcal{T}^{-1}H_0(\mathbf{k})\mathcal{T} = H_0(-\mathbf{k}). \quad (3.21)$$

If we look at the form of the Hamiltonian (3.1) in momentum space [Eq. (3.5)], condition (3.21) implies that the Hamiltonians  $h_{\mathbf{k}}^\sigma$  of each spin sector should obey the constrain

$$h_{\mathbf{k}}^\downarrow = h_{-\mathbf{k}}^{\uparrow*}. \quad (3.22)$$

The only way for condition (3.22) to be satisfied is by choosing the phase of the next-nearest-neighbors hopping as a spin dependent quantity, i.e.,  $\phi_\sigma$  should be positive ( $+\phi$ ) for the spin- $\uparrow$  electrons and negative ( $-\phi$ ) for the spin- $\downarrow$  electrons. Therefore, the time-

reversal- symmetric version of the Hamiltonian (3.1) is

$$\begin{aligned}
H_0 = & t_1 \sum_{i \in A, \delta, \sigma} \left( c_{iA\sigma}^\dagger c_{i+\delta B\sigma} + \text{H.c.} \right) \\
& + t_2 \sum_{i \in A, \tau, \sigma} \left( e^{-i\phi_\sigma} c_{iA\sigma}^\dagger c_{i+\tau A\sigma} + \text{H.c.} \right) \\
& + t_2 \sum_{i \in B, \tau, \sigma} \left( e^{+i\phi_\sigma} c_{iB\sigma}^\dagger c_{i+\tau B\sigma} + \text{H.c.} \right), \tag{3.23}
\end{aligned}$$

i.e., similar to Eq. (3.1), but with the sign of  $\phi_\sigma$  given by the convention stated above. Following the same steps employed in the diagonalization of the Chern insulator Hamiltonian (3.1) in Sec.3.1.1, we here arrive at the same general form of the free Hamiltonian [Eqs. (3.5)-(3.6)], where now the Hamiltonians of each spin sectors are

$$h_{\mathbf{k}}^\sigma = B_{0,\mathbf{k}}^\sigma \tau_0 + \mathbf{B}_{\mathbf{k}}^\sigma \cdot \hat{\tau}, \tag{3.24}$$

with the  $\mathbf{B}_{i,\mathbf{k}}^\sigma$  functions assuming the form

$$\begin{aligned}
B_{0,\mathbf{k}}^\sigma &= 2t_2 \cos(\phi_\sigma) \sum_{\tau} \cos(\mathbf{k} \cdot \boldsymbol{\tau}), \\
B_{1,\mathbf{k}} &= t_1 \sum_{\delta} \cos(\mathbf{k} \cdot \boldsymbol{\delta}), \\
B_{2,\mathbf{k}} &= t_1 \sum_{\delta} \sin(\mathbf{k} \cdot \boldsymbol{\delta}), \\
B_{3,\mathbf{k}}^\sigma &= -2t_2 \sin(\phi_\sigma) \sum_{\tau} \sin(\mathbf{k} \cdot \boldsymbol{\tau}). \tag{3.25}
\end{aligned}$$

Although the two spin sectors have different representations, they are related to each other through time-reversal symmetry, which implies that  $h_{\mathbf{k}}^\uparrow = (h_{-\mathbf{k}}^\downarrow)^*$ , as  $\phi_\uparrow = +\phi$  and  $\phi_\downarrow = -\phi$ . (see also, e.g, Appendix A from Ref. [24] for details). To simplify all the following expressions, we will use  $B_{i,\mathbf{k}}^\uparrow$  as reference and omit the spin dependence most of the time, but explicit it when needed. In this way, each spin sector can be diagonalized by a distinct canonical transformation [compare with (3.11)]

$$\begin{aligned}
c_{\mathbf{k}A\uparrow} &= u_{\mathbf{k}}^* d_{\mathbf{k}\uparrow} + v_{\mathbf{k}} c_{\mathbf{k}\uparrow}, & c_{\mathbf{k}B\uparrow} &= v_{\mathbf{k}}^* d_{\mathbf{k}\uparrow} - u_{\mathbf{k}} c_{\mathbf{k}\uparrow}, \\
c_{\mathbf{k}A\downarrow} &= u_{-\mathbf{k}} d_{\mathbf{k}\downarrow} + v_{-\mathbf{k}}^* c_{\mathbf{k}\downarrow}, & c_{\mathbf{k}B\downarrow} &= v_{-\mathbf{k}} d_{\mathbf{k}\downarrow} - u_{-\mathbf{k}}^* c_{\mathbf{k}\downarrow}, \tag{3.26}
\end{aligned}$$

with the common coefficients  $u_{\mathbf{k}}$  and  $v_{\mathbf{k}}$ . The coefficients are equal to (3.12), i.e.,

$$\begin{aligned}
|u_{\mathbf{k}}|^2 &= \frac{1}{2} \left( 1 + \hat{B}_{3,\mathbf{k}} \right), & |v_{\mathbf{k}}|^2 &= \frac{1}{2} \left( 1 - \hat{B}_{3,\mathbf{k}} \right), \\
u_{\mathbf{k}} v_{\mathbf{k}}^* &= \frac{1}{2} \left( \hat{B}_{1,\mathbf{k}} + i \hat{B}_{2,\mathbf{k}} \right), \tag{3.27}
\end{aligned}$$

with the hatted  $B_{i,\mathbf{k}} \equiv B_{i,\mathbf{k}}^\dagger$  being the  $i$ -th component of the vector  $\hat{\mathbf{B}}_{\mathbf{k}} = \mathbf{B}_{\mathbf{k}}/|\mathbf{B}_{\mathbf{k}}|$ . Again, the diagonalized Hamiltonian has the following form

$$H_0 = \sum_{\mathbf{k}\sigma} \omega_{\mathbf{k}\sigma}^c c_{\mathbf{k}\sigma}^\dagger c_{\mathbf{k}\sigma} + \omega_{\mathbf{k}\sigma}^d d_{\mathbf{k}\sigma}^\dagger d_{\mathbf{k}\sigma}, \quad (3.28)$$

with the electronic spectrum given by an updated expression [see Eq. (3.14)]

$$\omega_{\mathbf{k}\sigma}^{d/c} = B_0^\sigma \pm \sqrt{B_{1,\mathbf{k}}^2 + B_{2,\mathbf{k}}^2 + B_{3,\mathbf{k}}^{\sigma^2}}, \quad (3.29)$$

which now explicitly incorporates the dependence on the spin degree of freedom. Nevertheless, both  $c$  and  $d$  free-electronic bands are still doubly degenerated with respect to the spin degree of freedom if the mass term (3.19) is not included. Therefore, in the absence of the mass term (3.19), the electronic spectrum can be cast into the nearly flat band limit (3.18) with the bands having the same behavior as shown in Fig. 3.2.

With respect to the band topology, there are some differences as compared with the system where TRS is broken. Here, the Chern numbers of the free-electronic bands are given by  $C_\downarrow^d = -C_\uparrow^d = -1$  and  $C_\downarrow^c = -C_\uparrow^c = +1$ . Interestingly, at half-filling, the total Chern number, which is the sum of all Chern numbers of the filled bands, adds to zero. Nevertheless, one finds that the spin Chern number  $C_s^c$  of the  $c$  bands, defined by Eq. (2.12), is finite and equal to one, i.e.,

$$C_s^c = \frac{1}{2} (C_\downarrow^c - C_\uparrow^c) = 1. \quad (3.30)$$

In this condition, the system should display the quantum spin Hall effect with the spin Hall conductivity given by  $\sigma_{xy}^{SH} = eC_s^c/2\pi$ . Recall that the  $Z_2$  invariant is directly related to the  $C_s$  number for systems that preserve the total  $S_z$  component of the spin [2, 3], which is indeed the case here [spin symmetries are discussed in Appendix A]. Therefore, the model (3.23) indeed describes a  $Z_2$  topological insulator (see also discussion in Ref. [24]).

### 3.2.2 Mass term

With the inclusion of the mass term (3.19) into the Hamiltonian (3.23), all equations concerning the diagonalization of this new Hamiltonian are equal to the ones discussed in Sec.3.1.2, apart from the replacement (3.20). The degeneracy of the  $c$  and  $d$  electronic bands (3.29) with respect to the degrees of freedom is removed, see Fig. 3.5. For example, at the  $K$  point,  $\omega_{\mathbf{k}\uparrow}^c < \omega_{\mathbf{k}\downarrow}^c$  and the effect is reversed at the  $K'$  point. Interestingly, the curves overlap near the  $\Gamma$  and  $M$  points. The mass term mildly affects the bandwidth of the lower  $c$  band as it can be seen in Fig. 3.5(b) for  $M = 0.1t_1$ .

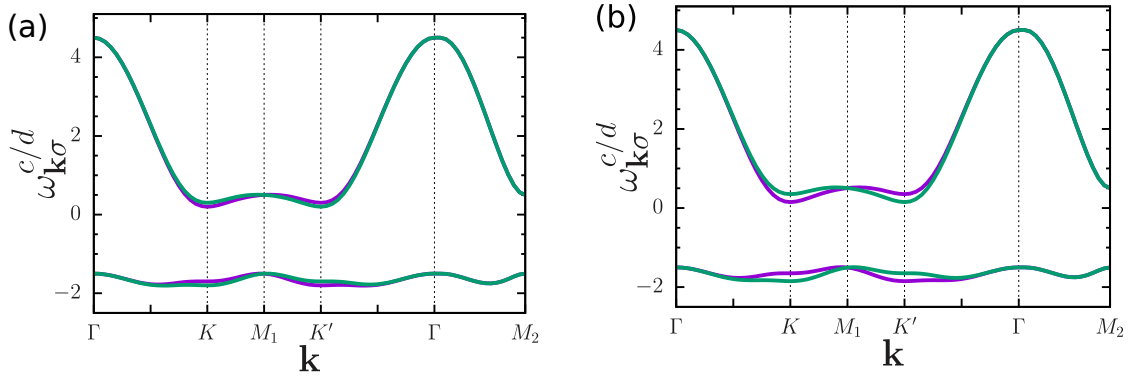


**Figure 3.5:** Electronic spectrum (3.14) with modification (3.20) at the nearly flat band limit (3.18) for (a)  $M = 0.05t_1$  and (b)  $M = 0.1t_1$ . A finite  $M$  lifts the degeneracy between the spin- $\uparrow$  (green) and the spin- $\downarrow$  (magenta) bands as compared to the Chern insulator [Fig. 3.4]. The path chosen in momentum space follows the highly symmetric points in the first Brillouin zone [Fig. 3.1(b)].

### 3.3 Itinerant ferromagnetism

Consider the case where the system is in the nearly flat band limit (3.18) of the electronic bands (3.14) and (3.29) and at 1/4 filling, i.e., only one of the lower  $c$  bands is completely filled. In this situation, Hund's rule indicates that the ground state is spin polarized, representing a ferromagnetic ground state. Figure 3.6 shows a pictorial representation of such state. If the occupied band is  $\omega_{k\uparrow}^c$ , the ground state can be written as a single-particle product state

$$|\text{FM}\rangle = \prod_{\mathbf{k} \in \text{BZ}} c_{\mathbf{k}\uparrow}^\dagger |0\rangle. \quad (3.31)$$

As this ordering occurs in momentum space, the spins are not localized, and therefore, the ferromagnetism will be driven by the conduction electrons, characterizing an itinerant ferromagnetism. This type of flat-band ferromagnetism was previously studied by Tasaki and Mielke [44, 45]. It was shown that the spin polarized ground state is stable in the presence of Coulomb interaction, for instance, by adding a Hubbard term

$$H_U = U \sum_i n_{i\uparrow} n_{i\downarrow}, \quad (3.32)$$

that provides an energy penalty when lattice sites are simultaneously occupied by one spin- $\uparrow$  and one spin- $\downarrow$  electron. In this cases [44, 45], there is a minimum critical value for the on-site energy  $U > U_c$ , above which ferromagnetism is stabilized. Also, Neupert *et al.* [21] have showed that in a topological Hubbard model with flat bands at 1/4 filling, a ferromagnetic ground state is stabilized by the Hubbard interaction. In the next two chapters, we will investigate the stability of a flat-band ferromagnetic ground state for both Chern and  $Z_2$  topological insulators. Stability signatures usually can be found in

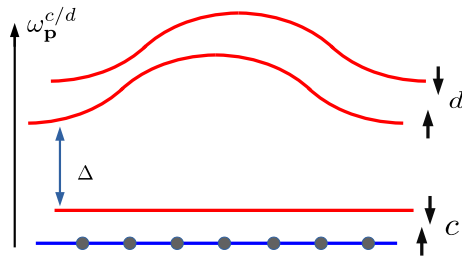


**Figure 3.6:** Schematic representation of the ground state (3.31) of the noninteracting term (3.1) in the nearly flat limit (3.18) of the lower band  $c$  at  $1/4$ -filling. Although the free bands  $c$  and  $d$  are doubly degenerated with respect to the spin degree of freedom, an offset between the  $\sigma = \uparrow$  and  $\downarrow$  bands are introduced for clarity.

the spin-wave spectrum, which will be derived using a bosonization scheme.

# Chapter 4

## Correlated Chern insulator

In this chapter, we will add a Hubbard interaction term to the noninteraction model (3.1) that describes a Chern insulator. To treat the effects of the interaction, a bosonization scheme, previously used to describe quantum Hall systems, will be applied. The original interacting fermion model will be mapped onto a bosonic interacting model, that describes the low energy magnetic excitations of the system, and that can be solved analytically at the harmonic approximation. This chapter is based on Ref. [34].

### 4.1 Haldane-Hubbard model for the Chern insulator

Let us consider  $N_e$  spin-1/2 electrons on a honeycomb lattice described by the Haldane-Hubbard model, whose Hamiltonian is given by [43, 46, 47, 48, 49, 50, 51, 52, 53, 54].

$$H = H_0 + H_U, \quad (4.1)$$

where the free term  $H_0$  is given by (3.1), while the interacting term  $H_U$  is given by a Hubbard like term,

$$H_U = \sum_i \sum_{a=A,B} U_a \hat{\rho}_{ia\uparrow} \hat{\rho}_{ia\downarrow}. \quad (4.2)$$

The term  $H_0$  [Eq. (3.1)] is a tight-binding term which describes electrons hopping between lattice sites as described in detail in Chapter 3. The interaction term  $H_U$  [Eq. (4.2)] is the one-site Hubbard repulsion term, which represents an energy cost paid by double occupation of site  $i$ , and

$$\hat{\rho}_{ia\sigma} = c_{ia\sigma}^\dagger c_{ia\sigma} \quad (4.3)$$

is the density operator associated with electrons with spin  $\sigma$  at site  $i$  of sublattice  $a$ . We consider that the one-site repulsion energies  $U_a > 0$  may depend on the sublattice  $a$ .

The expression for the on-site Hubbard interaction (4.2) in momentum space easily follows from the Fourier transform of the electron density operator (4.3), which is given

by

$$\hat{\rho}_{i a \sigma} = \frac{1}{N} \sum_{\mathbf{q} \in \text{BZ}} e^{i \mathbf{q} \cdot \mathbf{R}_i} \hat{\rho}_{a \sigma}(\mathbf{q}). \quad (4.4)$$

Substituting Eq. (4.4) into the Hamiltonian (4.2), one finds

$$H_U = \frac{1}{N} \sum_{a=A,B} \sum_{\mathbf{q}} U_a \hat{\rho}_{a \uparrow}(-\mathbf{q}) \hat{\rho}_{a \downarrow}(\mathbf{q}). \quad (4.5)$$

It is also useful to determine the expansion of the density operator  $\hat{\rho}_{a \sigma}(\mathbf{k})$  in terms of the (original) fermion operators  $c_{\mathbf{k} a \sigma}$ . With the aid of Eqs. (3.4), (4.3), and (4.4), one shows that

$$\hat{\rho}_{a \sigma}(\mathbf{q}) = \sum_{\mathbf{p}} c_{\mathbf{p}-\mathbf{q} a \sigma}^\dagger c_{\mathbf{p} a \sigma}. \quad (4.6)$$

The canonical transformation (3.11) allows us to express (4.6) in terms of the fermion operators  $c_{\mathbf{k} \sigma}$  and  $d_{\mathbf{k} \sigma}$ . In particular, the density operator (4.6) *projected* into the lower noninteracting band  $c$  reads [24]

$$\bar{\rho}_{a \sigma}(\mathbf{q}) = \sum_{\mathbf{p}} G_a(\mathbf{p}, \mathbf{q}) c_{\mathbf{p}-\mathbf{q} \sigma}^\dagger c_{\mathbf{p} \sigma}, \quad (4.7)$$

with the  $G_a(\mathbf{p}, \mathbf{q})$  function given by the coefficients (3.12) of the canonical transformation (3.11), i.e.,

$$G_a(\mathbf{p}, \mathbf{q}) = \delta_{a,A} v_{\mathbf{p}-\mathbf{q}}^* v_{\mathbf{p}} + \delta_{a,B} u_{\mathbf{p}-\mathbf{q}}^* u_{\mathbf{p}}. \quad (4.8)$$

Once the expression of the projected density operator (4.7) is known, we can determine the projection  $\bar{H}_U$  of the on-site Hubbard term (4.5) into the noninteracting lower  $c$  bands. Indeed,  $\bar{H}_U$  assumes the form (4.5) with the replacement  $\hat{\rho}_{a \sigma}(\mathbf{q}) \rightarrow \bar{\rho}_{a \sigma}(\mathbf{q})$ , i.e.,

$$\bar{H}_U = \frac{1}{N} \sum_{a=A,B} \sum_{\mathbf{q}} U_a \bar{\rho}_{a \uparrow}(-\mathbf{q}) \bar{\rho}_{a \downarrow}(\mathbf{q}). \quad (4.9)$$

## 4.2 Bosonization scheme

In this section, we briefly summarize the bosonization scheme for a Chern insulator introduced in Ref. [24] for the description of the flat-band ferromagnetic phase of a correlated Chern insulator on a square lattice.

Let us consider a spinfull Chern insulator on a bipartite lattice whose Hamiltonian assumes the form (3.5). To start, we choose the flat band limit (3.18), where the lower  $c$  band has the largest flatness ratio (3.17). Also, by considering the 1/4-filling of the electronic bands (3.14), the ground state of the noninteracting system is given by a spin-

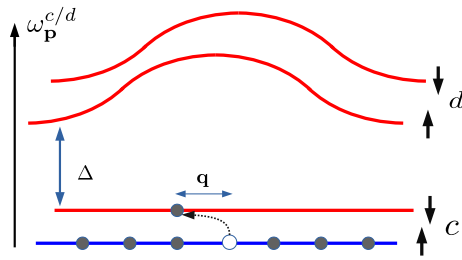


**Figure 4.1:** Schematic representation of a particle-hole pair excitation above the ground state (3.31). Although the free bands  $c$  and  $d$  are doubly degenerated with respect to the spin degree of freedom, an offset between the  $\sigma = \uparrow$  and  $\downarrow$  bands are introduced for clarity.

polarized state represented by the single-particle product state (3.31). This will be the **reference state** in which the bosonization scheme will be built upon.

Since the lower flat  $c$  bands are separated from the upper  $d$  bands by a large energy gap  $\Delta$ , all the physics will be dominated by process within the lower  $c$  bands. Therefore, the lowest-energy neutral excitations above the ground state (3.31) are given by particle-hole pairs within the lower  $c$  bands, i.e., they are spin-flips that can be written as [see Fig. 4.1]

$$|\Psi_{\mathbf{k}}\rangle \propto S_{\mathbf{k}}^- |\text{FM}\rangle. \quad (4.10)$$

The correct expression for Eq. (4.10) can be a little tricky to find, as the proportionality coefficient might also depend on the momentum [55]. Nevertheless, it is possible to construct (approximated) boson operators that represent this type of excitations [see Appendix B for details]. Indeed, one can define boson operators,

$$\begin{aligned} b_{\alpha, \mathbf{q}} &= \frac{\bar{S}_{-\mathbf{q}, \alpha}^+}{F_{\alpha\alpha, \mathbf{q}}} = \frac{1}{F_{\alpha\alpha, \mathbf{q}}} \sum_{\mathbf{p}} g_{\alpha}(\mathbf{p}, -\mathbf{q}) c_{\mathbf{p}+\mathbf{q}\uparrow}^{\dagger} c_{\mathbf{p}\downarrow}, \\ b_{\alpha, \mathbf{q}}^{\dagger} &= \frac{\bar{S}_{\mathbf{q}, \alpha}^-}{F_{\alpha\alpha, \mathbf{q}}} = \frac{1}{F_{\alpha\alpha, \mathbf{q}}} \sum_{\mathbf{p}} g_{\alpha}(\mathbf{p}, \mathbf{q}) c_{\mathbf{p}-\mathbf{q}\downarrow}^{\dagger} c_{\mathbf{p}\uparrow}, \end{aligned} \quad (4.11)$$

with  $\alpha = 0, 1$ , that satisfy the canonical commutation relations

$$\begin{aligned} [b_{\alpha, \mathbf{k}}, b_{\beta, \mathbf{q}}^{\dagger}] &= \delta_{\alpha, \beta} \delta_{\mathbf{k}, \mathbf{q}}, \\ [b_{\alpha, \mathbf{k}}, b_{\beta, \mathbf{q}}] &= [b_{\alpha, \mathbf{k}}^{\dagger}, b_{\beta, \mathbf{q}}^{\dagger}] = 0, \end{aligned} \quad (4.12)$$

and whose vacuum state is given by the (reference) spin-polarized state (3.31), i.e.,

$$b_{\alpha, \mathbf{q}} |\text{FM}\rangle = 0. \quad (4.13)$$

Here the operators  $\bar{S}_{\mathbf{q}, \alpha}^{\pm}$  are linear combinations of *projected* spin operators associated with sublattices  $A$  and  $B$ ,

$$\bar{S}_{\mathbf{q}, \alpha}^{\pm} = \bar{S}_{\mathbf{q}, A}^{\pm} + (-1)^{\alpha} \bar{S}_{\mathbf{q}, B}^{\pm}, \quad (4.14)$$

with  $\alpha = 0, 1$  and  $\bar{S}_{\mathbf{q},a}^{\pm} = \bar{S}_{\mathbf{q},a}^x \pm i\bar{S}_{\mathbf{q},a}^y$ . The operator  $\bar{S}_{\mathbf{q},a}^{\lambda}$ , with  $\lambda = x, y, z$ , is the  $\lambda$ -component of the spin operator  $S_{\mathbf{q},a}^{\lambda}$  projected into the lower  $c$  bands with  $S_{\mathbf{q},a}^{\lambda}$  being the Fourier transform of the spin operator  $S_{i,a}^{\lambda}$  at site  $i$  of the sublattice  $a$ . Indeed, the projected operator  $\bar{S}_{\mathbf{q},a}^{\lambda}$  is determined from the operator  $S_{i,a}^{\lambda}$ , following the same procedure outlined in Sec. 4.1 for the density operator (4.7). Finally, the square of the  $F_{\alpha\beta,\mathbf{q}}$  function is given by

$$F_{\alpha\beta,\mathbf{q}}^2 = \sum_{\mathbf{p}} g_{\alpha}(\mathbf{p}, \mathbf{q}) g_{\beta}^*(\mathbf{p}, \mathbf{q}), \quad (4.15)$$

with the  $g_{\alpha}(\mathbf{p}, \mathbf{q})$  function being related to the coefficients (3.12) of the canonical transformation (3.11),

$$g_{\alpha}(\mathbf{p}, \mathbf{q}) = v_{\mathbf{p}-\mathbf{q}}^* v_{\mathbf{p}} + (-1)^{\alpha} u_{\mathbf{p}-\mathbf{q}}^* u_{\mathbf{p}}. \quad (4.16)$$

Any operator expanded in terms of the fermion operators  $c_{\mathbf{k}\sigma}^{\dagger}$  and  $c_{\mathbf{k}\sigma}$  can, in principle, be rewritten in terms of the bosons (4.11). In particular, the density operator (4.7) projected into the lower  $c$  bands assumes the form

$$\bar{\rho}_{a\sigma}(\mathbf{k}) = \frac{1}{2} N \delta_{\sigma,\uparrow} \delta_{\mathbf{k},0} + \sum_{\alpha,\beta} \sum_{\mathbf{q}} \mathcal{G}_{\alpha\beta a\sigma}(\mathbf{k}, \mathbf{q}) b_{\beta,\mathbf{k}+\mathbf{q}}^{\dagger} b_{\alpha,\mathbf{q}}, \quad (4.17)$$

where the  $\mathcal{G}_{\alpha\beta a\sigma}(\mathbf{k}, \mathbf{q})$  function is given by Eqs. (B.24) and (B.23). Importantly, both  $F_{\alpha\beta,\mathbf{q}}^2$  and  $\mathcal{G}_{\alpha\beta a\sigma}(\mathbf{k}, \mathbf{q})$  functions can be explicitly written in terms of the coefficients (3.10), see Eqs. (C.1) and (C.2), respectively.

### 4.2.1 Effective bosonic Hamiltonian

The bosonization scheme developed in Ref. [24] allows us to map the Hamiltonian (4.1) into an effective interacting boson model. In order to derive such an effective boson model, the first step is to project the Hamiltonian (4.1) into the lower noninteracting  $c$  bands (see Eq. (28) from Ref. [24] for details):

$$H \rightarrow \bar{H} = \bar{H}_0 + \bar{H}_U. \quad (4.18)$$

Here the projected noninteracting term  $\bar{H}_0$  follows from Eq. (3.13),

$$\bar{H}_0 = \sum_{\mathbf{k}\sigma} \omega_{\mathbf{k}}^c c_{\mathbf{k}\sigma}^{\dagger} c_{\mathbf{k}\sigma}, \quad (4.19)$$

while the projected on-site Hubbard term  $\bar{H}_U$  is given by Eq. (4.9).

The expression of the noninteracting (kinetic) term  $\bar{H}_0$  in terms of the bosons (4.11) is given by (see Appendix B.2 for details)

$$\bar{H}_{0,B} = E_0 + \sum_{\alpha\beta} \sum_{\mathbf{q} \in BZ} \bar{\omega}_{\mathbf{q}}^{\alpha\beta} b_{\beta,\mathbf{q}}^{\dagger} b_{\alpha,\mathbf{q}}, \quad (4.20)$$

where  $E_0 = \sum_{\mathbf{k}} \omega_{\mathbf{k}}^c$  is a constant associated with the action of  $\bar{H}_0$  into the reference state (3.31) and

$$\bar{\omega}_{\mathbf{q}}^{\alpha\beta} = \frac{1}{F_{\alpha\alpha,\mathbf{q}} F_{\beta\beta,\mathbf{q}}} \sum_{\mathbf{p}} (\omega_{\mathbf{p}-\mathbf{q}}^c - \omega_{\mathbf{p}}^c) g_{\alpha}(\mathbf{p}, \mathbf{q}) g_{\beta}^*(\mathbf{p}, \mathbf{q}), \quad (4.21)$$

with the  $F_{\alpha\beta,\mathbf{q}}$  and the  $g_{\alpha}(\mathbf{p}, \mathbf{q})$  functions given by Eqs. (4.15) and (4.16), respectively. The bosonic representation of the projected on-site Hubbard term  $\bar{H}_U$  follows from Eqs. (4.9) and (4.17): After normal ordering the expression resulting from the substitution of the density operator (4.17) into (4.9), one shows that [24]

$$\bar{H}_{U,B} = \bar{H}_{U,B}^{(2)} + \bar{H}_{U,B}^{(4)}, \quad (4.22)$$

where the quadratic and quartic boson terms read

$$\bar{H}_{U,B}^{(2)} = \sum_{\alpha\beta} \sum_{\mathbf{q}} \epsilon_{\mathbf{q}}^{\alpha\beta} b_{\beta,\mathbf{q}}^{\dagger} b_{\alpha,\mathbf{q}}, \quad (4.23)$$

$$\bar{H}_{U,B}^{(4)} = \frac{1}{N} \sum_{\mathbf{k},\mathbf{q},\mathbf{p}} \sum_{\alpha\beta\alpha'\beta'} V_{\mathbf{k},\mathbf{q},\mathbf{p}}^{\alpha\beta\alpha'\beta'} b_{\beta',\mathbf{p}+\mathbf{k}}^{\dagger} b_{\beta,\mathbf{q}-\mathbf{k}}^{\dagger} b_{\alpha\mathbf{q}} b_{\alpha'\mathbf{p}}, \quad (4.24)$$

with the coefficient

$$\begin{aligned} \epsilon_{\mathbf{q}}^{\alpha\beta} &= \frac{1}{2} \sum_a U_a \mathcal{G}_{\alpha\beta a\downarrow}(0, \mathbf{q}) \\ &+ \frac{1}{N} \sum_{a,\alpha',\mathbf{k}} U_a \mathcal{G}_{\alpha'\beta a\uparrow}(-\mathbf{k}, \mathbf{k} + \mathbf{q}) \mathcal{G}_{\alpha\alpha' a\downarrow}(\mathbf{k}, \mathbf{q}) \end{aligned} \quad (4.25)$$

and the boson-boson interaction given by

$$V_{\mathbf{k},\mathbf{q},\mathbf{p}}^{\alpha\beta\alpha'\beta'} = \frac{1}{N} \sum_a U_a \mathcal{G}_{\alpha\beta a\uparrow}(-\mathbf{k}, \mathbf{q}) \mathcal{G}_{\alpha'\beta' a\downarrow}(\mathbf{k}, \mathbf{p}). \quad (4.26)$$

The effective *interacting* boson model that describes the flat-band ferromagnetic phase of the Haldane-Hubbard model (4.1) then assumes the form

$$\bar{H}_B = \bar{H}_{0,B} + \bar{H}_{U,B}^{(2)} + \bar{H}_{U,B}^{(4)}. \quad (4.27)$$

## 4.2.2 Spin-wave spectrum in the nearly flat band limit

In this section, we consider the effective boson model (4.27) in the lowest-order (harmonic) approximation, which consists of keeping only terms up to quadratic order in the

boson operators (4.11) of the Hamiltonian (4.27), i.e., we consider

$$\bar{H}_B \approx \bar{H}_{0,B} + \bar{H}_{U,B}^{(2)}. \quad (4.28)$$

In principle, the Hamiltonian (4.28) can be diagonalized via a canonical transformation yielding the spectrum of elementary excitations (spin-waves) in terms of  $\bar{\omega}_{\mathbf{q}}^{\alpha\beta}$  [Eq. (4.21)] and  $\epsilon_{\mathbf{q}}^{\alpha\beta}$  [Eq. (4.25)]. However, before proceeding, we would like to discuss both contributions in details.

The coefficient  $\bar{\omega}_{\mathbf{q}}^{\alpha\beta}$  [Eq. (4.21)] represents the (kinetic) contribution to the energy of the elementary excitations explicitly related to the dispersion of the noninteracting (lower)  $c$  bands. One can see that, if the free  $c$  band is completely flat ( $\omega_{\mathbf{q}}^c = \text{constant}$ ), this coefficient vanishes while, in the nearly flat band limit, it can be finite. For the noninteracting term (3.1) on the honeycomb lattice at the nearly flat-band limit (3.18), we find that  $\bar{\omega}_{\mathbf{q}}^{\alpha\alpha} = 0$  while  $\bar{\omega}_{\mathbf{q}}^{01} = \bar{\omega}_{\mathbf{q}}^{10}$  are finite but rather small in units of the nearest-neighbor hopping energy  $t_1$  [see Fig. 4.2(a)]. Such a result is distinct from the square lattice  $\pi$ -flux model, where symmetry considerations yield  $\bar{\omega}_{\mathbf{q}}^{\alpha\beta} = 0$  [24]. We believe that the finite values of the coefficients  $\bar{\omega}_{\mathbf{q}}^{01}$  and  $\bar{\omega}_{\mathbf{q}}^{10}$  for the Haldane model might be related not only to the symmetries of the noninteracting Hamiltonian (3.1), but also to the fact that the condition

$$F_{\alpha\beta,\mathbf{q}} = \delta_{\alpha,\beta} F_{\alpha\alpha,\mathbf{q}} \quad (4.29)$$

is not fulfilled for the Haldane model, an important feature distinct from the square lattice  $\pi$ -flux model [24]. We refer the reader to Appendix B for a detailed discussion about the implications of the condition (4.29) for the approximations involved in the bosonization scheme. Due to the smallness of  $\bar{\omega}_{\mathbf{q}}^{01}$  and  $\bar{\omega}_{\mathbf{q}}^{10}$ , in the following, we assume that  $\bar{\omega}_{\mathbf{q}}^{\alpha\beta} \approx 0$ , i.e., we neglected the (explicit) kinetic contribution (4.21) to the energy of the elementary excitations.

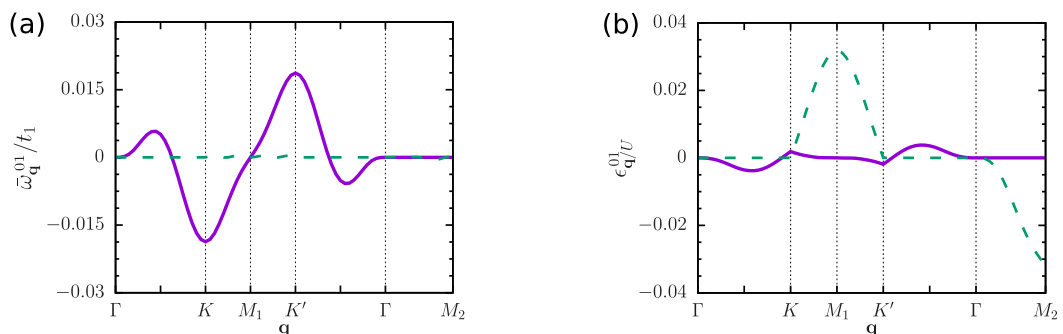


**Figure 4.2:** The real (solid magenta line) and imaginary (dashed green line) parts of (a) the coefficient  $\bar{\omega}_{\mathbf{q}}^{01}$  [Eq. (4.21)] and (b) the coefficient  $\epsilon_{\mathbf{q}}^{01}$  [Eq. (4.25)] along paths in the first Brillouin zone [Fig. 3.1(b)] for the Haldane-Hubbard model (3.1) in the nearly-flat band limit (3.18) of the lower noninteracting band  $c$ .

Concerning the coefficients (4.25), which are related to the on-site Hubbard term (4.9),

we find that  $\epsilon_{\mathbf{q}}^{\alpha\alpha}$  are real quantities while  $\epsilon_{\mathbf{q}}^{01} = -\epsilon_{\mathbf{q}}^{10} = \epsilon_{-\mathbf{q}}^{10} = -\epsilon_{-\mathbf{q}}^{01}$  are complex ones, implying that the Hamiltonian (4.23) is non-Hermitian. Such a feature is also in contrast with the square lattice  $\pi$ -flux model [24] for which  $\epsilon_{\mathbf{q}}^{01} = \epsilon_{\mathbf{q}}^{10} = 0$ . In particular, for the nearly flat band limit (3.18), one finds that  $\epsilon_{\mathbf{q}}^{01}$  is quite pronounced around the  $M_1$  and  $M_2$  points and it is also finite close to the  $K$  and  $K'$  points of the first Brillouin zone [see Fig. 4.2(b)]. Again, we believe that the non-Hermiticity of the Hamiltonian  $\bar{H}_{U,B}^{(2)}$  might be an artifact of the bosonization scheme related to the fact that the condition (4.29) is not fulfilled for the Haldane model (see Appendix B for details). Since such an issue is not completely understood at the moment, in the following, we determine the spin-wave spectrum both in the presence and in the absence of the off-diagonal terms  $(\alpha, \beta) = (0, 1)$  and  $(1, 0)$  of the Hamiltonian (4.23).

The Hamiltonian (4.28) with  $\bar{\omega}_{\mathbf{q}}^{\alpha\beta} = 0$  can be diagonalized via a canonical transformation similar to Eq. (3.11),

$$\begin{aligned} b_{0,\mathbf{q}} &= u_{\mathbf{q}}^{\dagger} a_{+,\mathbf{q}} + v_{\mathbf{q}} a_{-,\mathbf{q}}, \\ b_{1,\mathbf{q}} &= v_{\mathbf{q}}^{\dagger} a_{+,\mathbf{q}} - u_{\mathbf{q}} a_{-,\mathbf{q}}, \end{aligned} \quad (4.30)$$

where the coefficients  $u_{\mathbf{q}}$  and  $v_{\mathbf{q}}$  are now given by

$$\begin{aligned} |u_{\mathbf{q}}|^2, |v_{\mathbf{q}}|^2 &= \frac{1}{2} \pm \frac{1}{4\epsilon_{\mathbf{q}}} (\epsilon_{\mathbf{q}}^{00} - \epsilon_{\mathbf{q}}^{11}), \\ u_{\mathbf{q}} v_{\mathbf{q}}^* &= \frac{\epsilon_{\mathbf{q}}^{01}}{4\epsilon_{\mathbf{q}}}, \quad v_{\mathbf{q}} u_{\mathbf{q}}^* = \frac{\epsilon_{\mathbf{q}}^{10}}{4\epsilon_{\mathbf{q}}}, \end{aligned} \quad (4.31)$$

with

$$\epsilon_{\mathbf{q}} = \frac{1}{2} \sqrt{(\epsilon_{\mathbf{q}}^{00} - \epsilon_{\mathbf{q}}^{11})^2 + 4\epsilon_{\mathbf{q}}^{01}\epsilon_{\mathbf{q}}^{10}}. \quad (4.32)$$

It is then easy to show that the Hamiltonian (4.28) assumes the form

$$\bar{H}_B = E_0 + \sum_{\mu=\pm} \sum_{\mathbf{q} \in BZ} \Omega_{\mu,\mathbf{q}} a_{\mu,\mathbf{q}}^{\dagger} a_{\mu,\mathbf{q}}, \quad (4.33)$$

where the constant  $E_0 = \sum_{\mathbf{k}} \omega_{\mathbf{k}}^c = (-1.69 t_1) N$  for the nearly flat-band limit (3.18) and the dispersion relation of the bosons  $a_{\pm}$  reads

$$\Omega_{\pm,\mathbf{q}} = \frac{1}{2} (\epsilon_{\mathbf{q}}^{00} + \epsilon_{\mathbf{q}}^{11}) \pm \epsilon_{\mathbf{q}}, \quad (4.34)$$

with  $\epsilon_{\mathbf{q}}$  given by Eq. (4.32). Assuming that  $\epsilon_{\mathbf{q}}^{01} = \epsilon_{\mathbf{q}}^{10} = 0$ , the dispersion relation (4.34) reduces to

$$\Omega_{-,\mathbf{q}} = \epsilon_{\mathbf{q}}^{00} \quad \text{and} \quad \Omega_{+,\mathbf{q}} = \epsilon_{\mathbf{q}}^{11}, \quad (4.35)$$

since  $\epsilon_{\mathbf{q}}^{00} < \epsilon_{\mathbf{q}}^{11}$ .

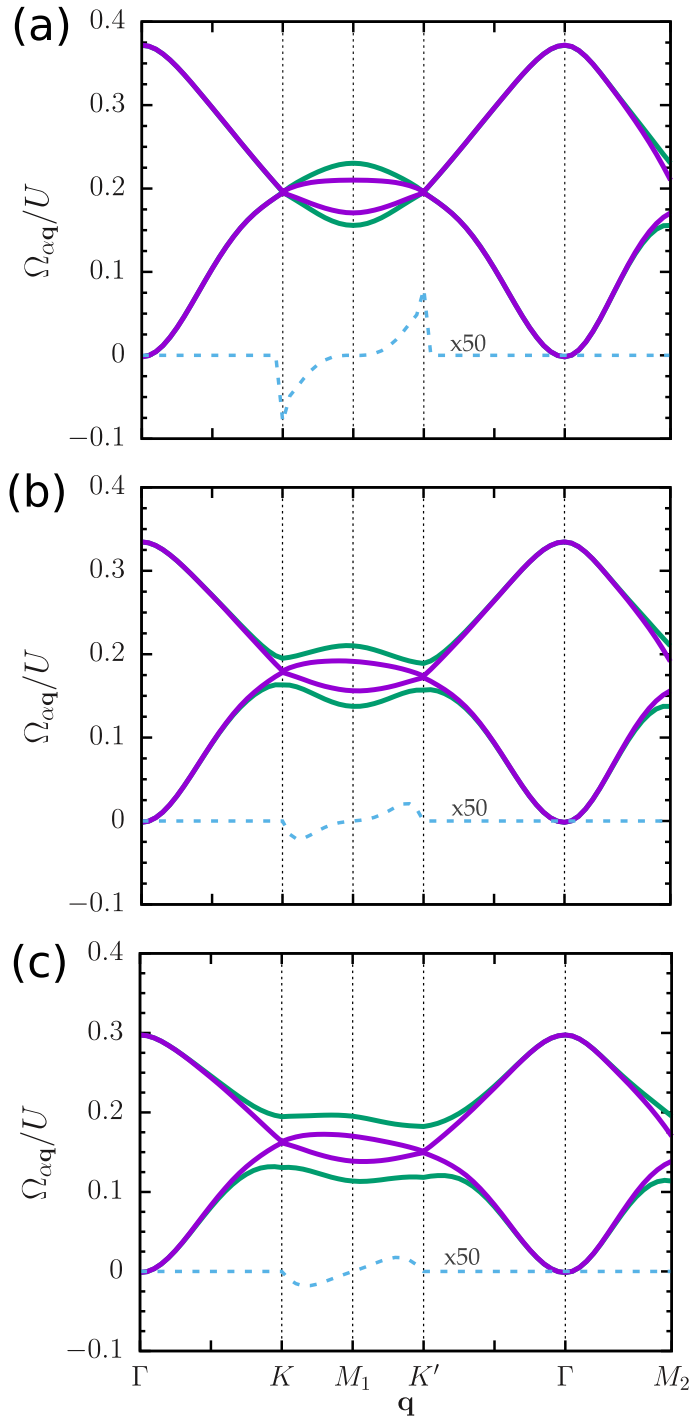


**Figure 4.3:** The elementary excitation (spin-wave) energies of the effective boson model (4.28) in the harmonic approximation for the nearly-flat band limit (3.18): dispersion relations (4.34) (real part, solid green line) and (4.35) (solid magenta line) along paths in the first Brillouin zone [Fig. 3.1(b)]. The dashed blue line indicates the imaginary part of  $\Omega_{+, \mathbf{q}} = -\Omega_{-, \mathbf{q}}$  [see Eq. (4.34)], which is multiplied by a factor of 50 for clarity. On-site repulsion energies: (a)  $U_A = U_B = U$ ; (b)  $U_B = 0.8U_A = 0.8U$ ; and (c)  $U_B = 0.6U_A = 0.6U$ .

One notices that the ground state of the Hamiltonian (4.33) is the vacuum (reference) state for both bosons  $b_{0,1}$  and  $a_{\pm}$ , which corresponds to the spin-polarized ferromagnet state |FM> [see Eqs. (3.31) and (4.13)]. Such a result is a first indication of the stability

of a flat-band ferromagnetic phase for the Haldane-Hubbard model (3.1).

The dispersion relations (4.34) and (4.35) of the bosons  $a_{\pm}$ , which indeed corresponds to the spin-wave spectrum above the flat-band ferromagnetic ground state (3.31), for the nearly flat band limit (3.18) and  $U_A = U_B = U$  is shown in Fig. 4.3(a). Due to the absence of the kinetic coefficients (4.21) associated with the dispersion of the noninteracting c bands, one sees that the energy scale of the spin-wave spectrum is determined by the on-site repulsion energy  $U$ . Both spin-wave spectra (4.34) and (4.35) have two branches: the acoustic (lower) branch  $\Omega_{-,q}$  is gapless, with a Goldstone mode at the Brillouin zone center ( $\Gamma$  point) and the characteristic quadratic dispersion of ferromagnetic spin-waves near the  $\Gamma$  point; the optical (upper) one  $\Omega_{+,q}$  is gapped, with the lowest energy excitation at the  $K$  and  $K'$  points. The presence of the Goldstone mode indicates the stability of the flat-band ferromagnetic phase. Interestingly, for the dispersion relation (4.35), one finds a quite small energy gap at the  $K$  and  $K'$  points,

$$\Delta^{(K)} = \Omega_{+,K} - \Omega_{-,K} = 2.01 \times 10^{-3} U, \quad (4.36)$$

while the excitation spectrum (4.34) displays Dirac points at the  $K$  and  $K'$  points. Indeed, the presence of the Dirac points is related to the fact that  $\epsilon_{\mathbf{q}}^{01}$  and  $\epsilon_{\mathbf{q}}^{10}$  are finite at the  $K$  and  $K'$  points, see Fig. 4.2(b). Moreover, the fact that  $\epsilon_{\mathbf{q}}^{01} = -\epsilon_{\mathbf{q}}^{10}$  yields a very small decay rate (the imaginary part of  $\Omega_{\pm,q}$ ) for the spin-wave excitations (4.34) at the border of the first Brillouin zone [see the dashed line in Fig. 4.3(a) and note the multiplicative factor 50].

In addition to a configuration with homogeneous on-site Hubbard energies  $U_A = U_B = U$ , we also consider the Haldane-Hubbard model with a sublattice dependent on-site Hubbard energy. The spin-wave spectra (4.34) and (4.35) for the nearly flat-band limit (3.18) and with  $U_B = 0.8U_A = 0.8U$  and  $U_B = 0.6U_A = 0.6U$  are shown in Figs. 4.3(b) and (c), respectively. One notices that both spin-wave spectra (4.34) and (4.35) have a Goldstone mode at the  $\Gamma$  point, the energies of the excitations decreases as the difference  $\Delta U = U_A - U_B$  increases, and the difference between the energies at the  $K$  and  $K'$  points (e.g.,  $\Omega_{-,K} - \Omega_{-,K'}$ ) also increases with  $\Delta U$ . For  $U_B > U_A$ , we find similar features (not shown here), but the energy at the  $K$  point is lower than the one at the  $K'$  point. Importantly, the dispersion relation (4.35) has a small gap at the  $K$  and  $K'$  points, i.e.,

$$\Delta^{(K)} = 1.81 \times 10^{-3} U \quad \text{for} \quad \Delta U = 0.2 U \quad (4.37)$$

and

$$\Delta^{(K)} = 1.61 \times 10^{-3} U \quad \text{for} \quad \Delta U = 0.4 U, \quad (4.38)$$

similar to the homogeneous case  $U_A = U_B$ . On the other hand, for the dispersion relation (4.34), a finite energy gap opens at the  $K$  and  $K'$  points in contrast with the homogeneous

case  $\Delta U = 0$ . One finds that

$$\Delta^{(K)} = 3.18 \times 10^{-2} U \quad \text{for} \quad \Delta U = 0.2 U, \quad (4.39)$$

and

$$\Delta^{(K)} = 6.40 \times 10^{-2} U \quad \text{for} \quad \Delta U = 0.4 U. \quad (4.40)$$

Such a finite energy gap might be related to the fact that a Hubbard term with  $U_A \neq U_B$  breaks inversion symmetry. Similar to the homogeneous configuration, the spin-wave excitations (4.34) at the first Brillouin zone border have a finite decay rate.

Meanwhile, Gu and collaborators [29] performed exact diagonalization calculations and determined the spin-wave spectrum for the Haldane-Hubbard model (4.1) in the nearly flat band limit (3.18), in one of the cases, neglecting the dispersion of the noninteracting electronic bands, which corresponds to the approximation  $\bar{\omega}_{\mathbf{q}}^{\alpha\beta} = 0$  considered above. As shown in Fig. 4.4(a<sub>1</sub>), for homogeneous on-site Hubbard energies  $U_A = U_B$  and at the nearly flat band limit, it was found that the spin-wave spectrum has Dirac points at the  $K$  and  $K'$  points while, for a finite  $\Delta U$  [Fig. 4.4(b<sub>1</sub>)], the energies of the excitations decrease with  $\Delta U$  and energy gaps open at the  $K$  and  $K'$  points. They also showed that the Chern number  $C_n$  of the lower spin-wave band is equal to zero for the flat band limit, as shown in Fig. 4.4(b<sub>1</sub>). Remarkably, the spin-wave spectrum (4.34) determined within the bosonization scheme qualitatively agrees with the numerical one, for both  $U_A = U_B$  and  $U_A > U_B$ , apart from the fact that the numerical results do not indicate a finite decay rate. Indeed, a good qualitative agreement was also found between the spin-wave spectrum calculated at the flat band limit using the bosonization scheme [24] and the one determined via exact diagonalization of a finite size system [28] for the Chern insulator in the square lattice described by the  $\pi$ -flux model discussed in Chapter 2.

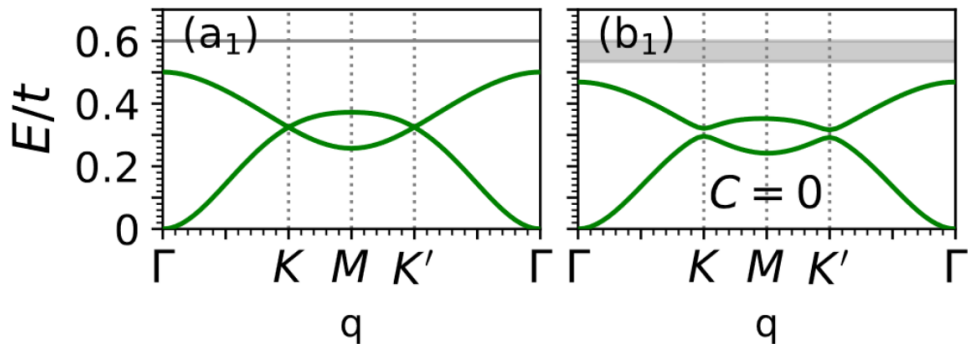


**Figure 4.4:** The spin-wave energies (solid lines) and the Stoke spectrum (gray) of the Haldane-Hubbard model (4.1) at the nearly flat band limit (3.18) calculated via exact diagonalization of the Hamiltonian for a finite system [29] along paths in the first Brillouin zone [Fig. 3.1(b)]. On-site repulsion energies: (a<sub>1</sub>)  $U_A = U_B = U$ ; (b<sub>1</sub>)  $U_B = 1.0688$  and  $U_A = 1.2$ ;  $C = 0$  is the Chern number of the lower band. Figure adapted from Ref. [29]

One should mention that the presence of Dirac points at the  $K$  and  $K'$  points is not only a feature of the spin-wave spectrum of the flat-band ferromagnetic phase of the Haldane-Hubbard model. Indeed, recent exact diagonalization calculations [30] for a topological Hubbard model on a kagome lattice also indicate such a feature in the excitation spectrum of the corresponding flat-band ferromagnetic phase when the dispersion of the (lower) noninteracting electronic band is neglected.

As mentioned above, although the non-Hermiticity of the Hamiltonian (4.23) (and consequently finite decay rates) might be an artifact of the bosonization scheme, the off-diagonal terms  $\epsilon_{\mathbf{q}}^{01}$  and  $\epsilon_{\mathbf{q}}^{10}$  of the quadratic Hamiltonian (4.23) should be considered in order to properly describe the spin-wave spectrum at the border of the first Brillouin zone. Therefore, in the following, we determine the spin-wave spectrum away from the nearly flat-band limit (3.18) with the aid of Eq. (4.34).

### 4.2.3 Spin-wave spectrum away from the nearly flat band limit

Although the main focus of our discussion is the description of the flat-band ferromagnetic phase of the Haldane-Hubbard model in the nearly-flat band limit (3.18), we also consider configurations such that the noninteracting band  $c$  has smaller flatness ratio  $f_c < 7$ . In particular, we consider the effects on the spin-wave spectrum (4.34) related to the increasing of the band width  $W_c$  (decreasing of the flatness ratio  $f_c$ ) of the noninteracting band  $c$  due to (i) the decrease/increase of the phase  $\phi$  [see Figs. 3.2(b) and (c)] and (ii) the presence of a staggered on-site energy term (3.19) in the total Hamiltonian (see Fig. 3.4). These perturbations provide some clues about the stability of the flat-band ferromagnetic phase.

In Fig. 4.5(a), we show the spin-wave spectrum (4.34) for  $\phi = 0.4, 0.5$ , and  $0.656$ , the

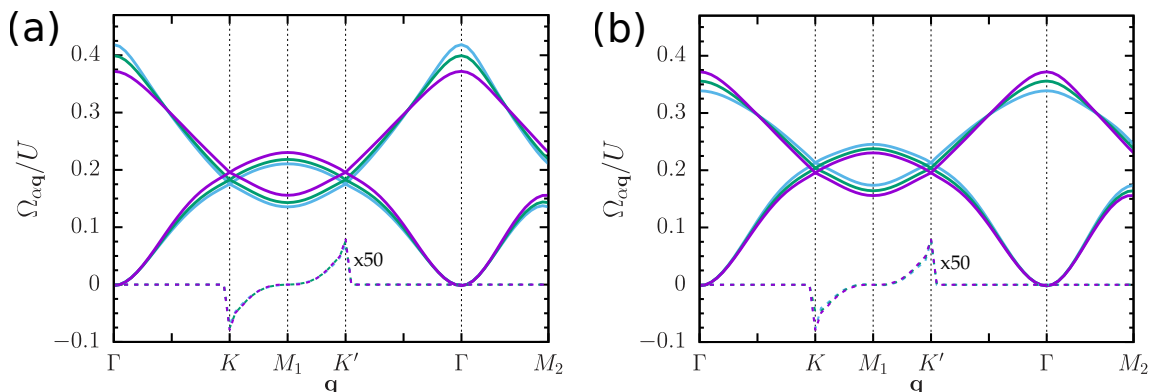


**Figure 4.5:** The real part of the dispersion relation (4.34) (solid line) along paths in the first Brillouin zone [Fig. 3.1(b)] for on-site repulsion energies  $U_A = U_B = U$  and  $t_2$  given by the relation  $\cos(\phi) = t_1/(4t_2)$ . (a)  $\phi = 0.4$  (blue),  $\phi = 0.5$  (green),  $\phi = 0.656$  (magenta) and (b)  $\phi = 0.656$  (magenta),  $\phi = 0.75$  (green),  $\phi = 0.85$  (blue). The corresponding dashed line indicates the imaginary part of  $\Omega_{+,q} = -\Omega_{-,q}$  [see Eq. (4.34)], which is multiplied by a factor of 50 for clarity.

hopping amplitude  $t_2$  given by the relation  $\cos(\phi) = t_1/(4t_2)$ , and the on-site repulsion energies  $U_A = U_B = U$ . One sees that the spin-wave spectrum (in units of the on-site repulsion energy  $U$ ) for  $\phi = 0.4$  and  $0.5$  is quite similar to the one derived for the nearly flat band limit (3.18). As the flux parameter  $\phi$  decreases, the excitation energies near the border of the Brillouin zone [the  $K$ - $M_1$ - $K'$  line] decrease, while the energies of the optical branch in the vicinity of the  $\Gamma$  point increase. The fact that the spin-wave spectrum displays a Goldstone mode at the  $\Gamma$  point, regardless the value of the phase  $\phi$ , indicates the stability of the flat-band ferromagnetic phase with respect to the simultaneous variations of the phase  $\phi$  and the next-nearest-neighbor hopping amplitude  $t_2$ . Finite decay rates are still found at the border of the first Brillouin zone. The flat-band ferromagnetic phase seems also to be stable for  $\phi > 0.656$ , see Fig. 4.5(b). Here, however, as the flux parameter  $\phi$  increases, the excitation energies near the border of the Brillouin zone increase and the energies of the upper branch in the vicinity of the  $\Gamma$  point decrease.

The effect on the spin-wave spectrum of a finite staggered on-site energy  $M$  [Eq. (3.19)] is quite distinct. In Fig. 4.6(a), we plot the spin-wave spectrum (4.34) for the optimal parameters (3.18),  $M = 0.1$  and  $0.2t_1$ , and the on-site Hubbard energies  $U_A = U_B = U = t_1$ . Comparing with the homogeneous on-site energy  $M = 0$  configuration [Fig. 4.3(a)], one sees that the whole spin-wave spectrum shifts downward in energy as  $M$  increases and energy gaps open at the  $K$  and  $K'$  points. The latter is indeed related to the fact that the staggered on-site energy term (3.19) breaks inversion symmetry. Most importantly, the energies of the acoustic branch are negative in the vicinity of the  $\Gamma$  point, indicating an instability of the flat-band ferromagnetic phase for finite values of the staggered on-site energy  $M$ . A finite staggered on-site energy  $M$  also modifies the (kinetic) coefficients (4.21) directly related to the dispersion of the noninteracting band  $c$ . In particular, we find that  $\bar{\omega}_{\mathbf{q}}^{\alpha\alpha}$  no longer vanishes for a finite  $M$  [see Fig. 4.2(a) for  $M = 0$ ]. Such an effect can be easily included in the spin-wave spectrum (4.34) with the replacement

$$\epsilon_{\mathbf{q}}^{\alpha\alpha} \rightarrow \bar{\omega}_{\mathbf{q}}^{\alpha\alpha} + \epsilon_{\mathbf{q}}^{\alpha\alpha}. \quad (4.41)$$

Figure 4.6(b) shows the spin-wave spectrum (4.34) with the replacement (4.41) (in units of the nearest-neighbor hopping amplitude  $t_1$ ) for the optimal parameters (3.18),  $M = 0.1$  and  $0.2t_1$ , and the on-site Hubbard energies  $U_A = U_B = U = t_1$ . One notices that  $\bar{\omega}_{\mathbf{q}}^{\alpha\alpha}$  does not modify the excitation energies in the vicinity of the  $\Gamma$  point, but only changes the excitation energies near the border  $K$ - $M_1$ - $K'$  of the first Brillouin zone. Such an effect resembles the one found when distinct on-site repulsion energies  $U_A \neq U_B$  are considered, see Figs. 4.3(b) and (c).

The stability of a flat-band ferromagnetic phase was studied by Kusakabe and Aoki via exact diagonalization calculations performed for the two-dimensional Mielke model [55] and Mielke and Tasaki models [56]. A parameter  $\gamma$  was introduced in the original models,

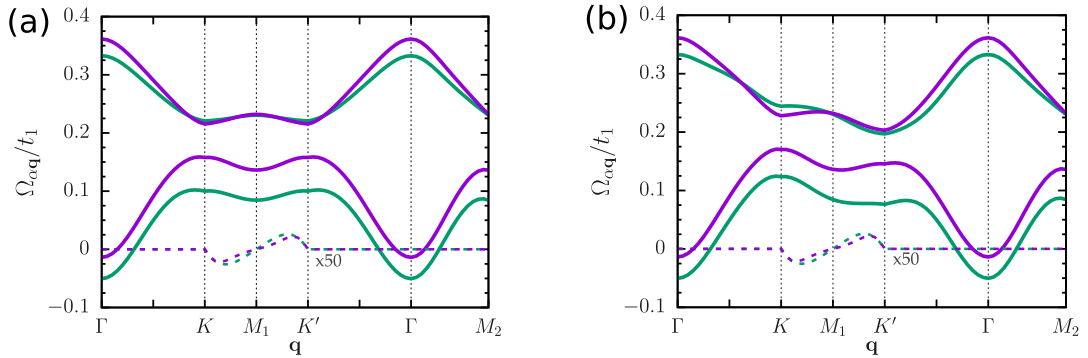


**Figure 4.6:** The real part of the dispersion relation (4.34) (solid line) along paths in the first Brillouin zone [Fig. 3.1(b)] for the optimal parameters (3.18), on-site Hubbard energies  $U_A = U_B = U = t_1$ , and staggered on-site energy  $M = 0.1$  (magenta) and  $0.2 t_1$  (green). (b) Similar results for the spin-wave spectrum (4.34), but with the replacement (4.41). The corresponding dashed line indicates the imaginary part of  $\Omega_{+,q} = -\Omega_{-,q}$  [see Eq. (4.34)], which is multiplied by a factor of 50 for clarity.

such that  $\gamma = 0$  corresponds to (lower) noninteracting bands completely flat (flat-band limit). It was found that, for  $\gamma = 0$ , a ferromagnetic phase is stable regardless the value of the on-site repulsion energy  $U$ . For finite values of the parameter  $\gamma$  (system away from the flat-band limit), a ferromagnetic ground state is stable only if  $U \geq U_c(\gamma)$  (see Figs. 1 and 2 from Ref. [56]). Such a scenario agrees with more recently numerical results for the square lattice  $\pi$ -flux model in the nearly-flat band limit [28], which indicates that a ferromagnetic phase sets in only if  $U \geq U_c(t_2)$ , with  $t_2$  being the next-nearest neighbor hopping amplitude. Müller *et al.* studied one- and two-dimensional Hubbard models with nearly-flat bands that are not in the class of Mielke and Tasaki flat-band models, since they do not obey some connectivity conditions [57]. They found that small and moderate noninteracting band dispersion may stabilize a ferromagnetic phase for  $U \geq U_c$ , i.e., the ferromagnetic phase is driven by the kinetic energy. In particular, for a two-dimensional bilayer model,  $U_c(\delta_l)$  is a nonmonotonic function of the parameter  $\delta_l$  that controls the width of the band (see Fig. 7 from [57]), i.e., the ferromagnetic phase sets in only for a finite band dispersion. For rigorous results about the stability of a ferromagnetic phase on Hubbard models with nearly-flat bands, we refer the reader to the review by Tasaki [44].

The fact that a ferromagnetic phase is stable in Hubbard models with nearly-flat (noninteracting) bands only for  $U \geq U_c$  is related to the competition between the kinetic energy (dispersion of the noninteracting bands) and the (short-range) Coulomb interaction  $U$  [44]. The bosonization formalism [24] partially takes into account such a competition: although the explicitly contribution (4.21) of the dispersion of the noninteracting bands  $c$  is not included in the effective boson model (4.27), such kinetic effects are partially considered by the bosonization scheme, since the coefficients (4.25) and the boson-boson interaction (4.26) depend on the  $\hat{B}_{i,q}$  functions (3.10) that completely determines the

free-band structure (3.14). At the moment, it is not clear how to properly include in the effective boson model (4.27) the main effects related to the noninteracting band dispersion. Due to this limitation, we expected that the results derived within the bosonization scheme for flat-band Chern insulators get more accurate as the (lower) noninteracting bands gets less dispersive. One should recall that the bosonization scheme [24] is based on the formalism [25] that was proposed to describe the quantum Hall ferromagnet realized in a two-dimensional electron gas at filling factor  $\nu = 1$ : here, the noninteracting bands corresponds to (completely flat) Landau levels.

Finally, we should mention that the instability of the flat-band ferromagnetic ground state due to a finite on-site staggered energy  $M$  was also found for the square lattice  $\pi$ -flux model [24], see Fig. E.1 in Appendix E. Indeed, as discussed in details in Appendix E, we tried a different combination of the projected spin operators (4.14) to correct for imbalances in the  $A$  and  $B$  sublattices caused by a mass term in the square lattice. Such more elaborated description could be needed for the bosonization scheme to properly describe mass term perturbations. Unfortunately, we found that the Goldstone mode could only be restored if the off-diagonal coefficients  $\epsilon_{\mathbf{q}}^{01}$  and  $\epsilon_{\mathbf{q}}^{10}$  are neglected.

# Chapter 5

## Correlated $Z_2$ topological insulator

As done for the Chern insulator in the last chapter, we now consider a correlated  $Z_2$  topological insulator on a honeycomb lattice described by a time-reversal symmetric Haldane-Hubbard model. In this chapter, we also derive an effective bosonic Hamiltonian that describes the corresponding flat-band ferromagnetic phase of the model and briefly comment on the differences between the systems that preserves and brakes time-reversal symmetry. Following the same steps, we discuss the resulting spin-wave spectrum in both nearly flat-band limit and away from it, and the stability of the flat-band ferromagnetic ground state. By the end of the chapter, we also comment on the topological properties of the spin-wave bands. This chapter is based on Ref. [35].

### 5.1 Time-reversal-symmetric Haldane Hubbard model for the $Z_2$ topological insulator

In this section, the interacting fermionic model for the  $Z_2$  topological insulator on a honeycomb lattice is constructed following the same steps as done for the correlated Chern insulator in Sec.4.2.1. The process begins by adding the same Hubbard term (4.2) to the free time-reversal-symmetric Hamiltonian (3.23). The only care that should be taken is that now the canonical transformation (3.26) is different for each spin sector, in opposition to the one used for the Chern insulator (3.11). For this reason, the fermionic representation of the projected electron density operator (4.6) is now given by [compare with Eq. (4.7)]

$$\bar{\rho}_{a\sigma}(\mathbf{q}) = \sum_{\mathbf{p}} G_{a\sigma}(\mathbf{p}, \mathbf{q}) c_{\mathbf{p}-\mathbf{q}\sigma}^\dagger c_{\mathbf{p}\sigma}, \quad (5.1)$$

where the  $G_{a\sigma}(\mathbf{p}, \mathbf{q})$  function is now defined as [compare with Eq. (4.8)]

$$\begin{aligned} G_{a\sigma}(\mathbf{p}, \mathbf{q}) = & \delta_{a,A} (\delta_{\sigma,\uparrow} v_{\mathbf{p}-\mathbf{q}}^* v_{\mathbf{p}} + \delta_{\sigma,\downarrow} v_{-\mathbf{p}+\mathbf{q}} v_{-\mathbf{p}}^*) \\ & + \delta_{a,B} (\delta_{\sigma,\uparrow} u_{\mathbf{p}-\mathbf{q}}^* u_{\mathbf{p}} + \delta_{\sigma,\downarrow} u_{-\mathbf{p}+\mathbf{q}} u_{-\mathbf{p}}^*), \end{aligned} \quad (5.2)$$

with  $u_{\mathbf{k}}$  and  $v_{\mathbf{k}}$  being the coefficients (3.27) of the canonical transformation (3.26). In summary, the density operator preserves the general form (4.7), but now the  $G_{\alpha\sigma}(\mathbf{p}, \mathbf{q})$  function is a spin dependent quantity. The same will happen with all functions throughout the calculations for the  $Z_2$  topological insulator. Nonetheless, all the resulting expressions obtained in Sec.4.2.1 will have the same form as we are going to see below.

## 5.2 Bosonization scheme for the $Z_2$ topological insulator

The free Hamiltonian (3.23) for the  $Z_2$  topological insulator also supports flat bands and a spin-polarized ground state at 1/4-filling, since the electronic spectrum (3.29), without the inclusion of the mass term (3.19), is identical to the spectrum (3.14). Therefore, the reference state for the bosonization, Eq. (3.31), will be the same. The low energy excitations will also be spin flips within the lower band  $c$ , as represented in Fig. 4.1.

Following the description of the correlated  $Z_2$  topological insulator on a square lattice [24], we define the boson operators  $b_{\alpha, \mathbf{q}}$  as

$$\begin{aligned} b_{\alpha, \mathbf{q}} &= \frac{\bar{S}_{-\mathbf{q}, \alpha}^+}{F_{\alpha\alpha, \mathbf{q}}} = \frac{1}{F_{\alpha\alpha, \mathbf{q}}} \sum_{\mathbf{p}} g_{\alpha}^*(-\mathbf{p}, \mathbf{q}) c_{\mathbf{p}+\mathbf{q}\uparrow}^{\dagger} c_{\mathbf{p}\downarrow}, \\ b_{\alpha, \mathbf{q}}^{\dagger} &= \frac{\bar{S}_{\mathbf{q}, \alpha}^-}{F_{\alpha\alpha, \mathbf{q}}} = \frac{1}{F_{\alpha\alpha, \mathbf{q}}} \sum_{\mathbf{p}} g_{\alpha}(\mathbf{p}, \mathbf{q}) c_{\mathbf{p}-\mathbf{q}\downarrow}^{\dagger} c_{\mathbf{p}\uparrow}, \end{aligned} \quad (5.3)$$

with  $\alpha = 0, 1$  and obeying the canonical bosonic commutation relations (4.12). Here,  $\bar{S}_{\mathbf{q}, \alpha}^{\lambda}$  is a linear combination of the spin operator  $S_{\mathbf{q}, ab}^{\lambda}$  projected into the lower  $c$  bands, i.e.,

$$\bar{S}_{\mathbf{q}, \alpha}^{\lambda} = \bar{S}_{\mathbf{q}, AB}^{\lambda} + (-1)^{\alpha} \bar{S}_{\mathbf{q}, BA}^{\lambda}, \quad (5.4)$$

with  $\lambda = x, y, z$ . It is important to emphasize that the real space representation of  $S_{\mathbf{q}, ab}$  is

$$\mathbf{S}_{i, ab} = \sum_{\mu\nu} \frac{1}{2} c_{ia\mu}^{\dagger} \hat{\sigma}_{\mu\nu} c_{ib\nu}, \quad (5.5)$$

where the components of the vector  $\hat{\sigma} = (\sigma_x, \sigma_y, \sigma_z)$  are the Pauli matrices. Notice that the projected spin operators (5.4) are related to spin flips that also change the sublattice index. Due to such a feature, we denote the excitations associated with the boson operators (5.3) and (5.4) as **mixed lattice** (ML) excitations. The square of the normalization function  $F_{\alpha\beta}$  is given by (see also Appendix B)

$$F_{\alpha\beta, \mathbf{q}}^2 = \sum_{\mathbf{p}} g_{\alpha}(\mathbf{p}, \mathbf{q}) g_{\beta}^*(-\mathbf{p} + \mathbf{q}, \mathbf{q}), \quad (5.6)$$

where the  $g_\alpha(\mathbf{p}, \mathbf{q})$  function is now given by

$$g_\alpha(\mathbf{k}, \mathbf{q}) = -u_{\mathbf{k}}v_{-\mathbf{k}+\mathbf{q}} - (-1)^\alpha u_{-\mathbf{k}+\mathbf{q}}v_{\mathbf{k}}, \quad (5.7)$$

with  $u_{\mathbf{k}}$  and  $v_{\mathbf{k}}$  being the coefficients (3.27) of the canonical transformation (3.26). The function  $F_{\alpha\beta,\mathbf{q}}^2$  can be explicitly written in terms of  $B_{i,\mathbf{k}}$  functions (3.25) and their full expression can be found in Appendix D. One also notes that, again,

$$b_{\alpha,\mathbf{q}}|\text{FM}\rangle = 0, \quad (5.8)$$

meaning that the spin-polarized state (3.31) is indeed the vacuum for the bosons (5.3).

Surprisingly, there is another pair of independent boson operators that possesses an even lower energy than the ones defined by Eqs. (5.3) and (5.4), as showed bellow in Sec.5.4. The main difference between this second set of boson operators and the ones defined by Eq. (5.4) is the linear combination of the spin operators. Indeed, for the second set, we consider

$$\bar{S}_{\mathbf{q},\alpha} = \bar{S}_{\mathbf{q},A}^\lambda + (-1)^\alpha \bar{S}_{\mathbf{q},B}^\lambda, \quad (5.9)$$

again, with  $\lambda = x, y, z$  and  $\alpha = 0, 1$ . In contrast with Eq. (5.4),  $\bar{S}_{\mathbf{q},A}^\lambda$  is the Fourier transform of the spin operator (5.5) with the same lattice index, i.e., with  $a = b$ . Because of this difference, we will refer to the excitations defined by (5.9) as the **same lattice (SL)** excitations. Furthermore, the definition of the bosons operators for the SL excitations follow the same form as Eq. (5.3), but now the  $g_\alpha(\mathbf{p}, \mathbf{q})$  function is given by

$$g_\alpha(\mathbf{p}, \mathbf{q}) = -v_{-\mathbf{p}+\mathbf{q}}v_{\mathbf{p}} + (-1)^\alpha u_{-\mathbf{p}+\mathbf{q}}u_{\mathbf{p}}. \quad (5.10)$$

The square of the normalization function  $F_{\alpha\beta,\mathbf{q}}^2$  also keeps its form (5.6), but now Eq. (5.10) must be used instead of (5.7). It will also have a different representation in terms of the  $B_{i,\mathbf{k}}$  functions (3.25), see Eq. (D.8).

Again, any fermionic operator can be described in terms of the boson operators (5.3), if the correct fundamental functions  $F_{\alpha\beta,\mathbf{q}}^2$ ,  $g_\alpha(\mathbf{p}, \mathbf{q})$  and  $\mathcal{G}_{\alpha\beta a\sigma}(\mathbf{p}, \mathbf{q})$  are used. Therefore, the application of the bosonization scheme for the correlated  $Z_2$  topological insulator follows the same steps as the ones employed for the Chern insulator. In summary, we first define the interacting fermionic model

$$H^{Z_2} = H_0 + H_U, \quad (5.11)$$

where  $H_0$  is the time-reversal-symmetric Hamiltonian (3.23) and  $H_U$  is the Hubbard term (4.2). After, we project the interacting fermionic model (5.11) into the lower c bands, i.e.,

$$H^{Z_2} \rightarrow \bar{H}^{Z_2}. \quad (5.12)$$

The projected Hamiltonian  $\bar{H}^{Z_2}$  can then be mapped into an effective interacting bosonic Hamiltonian, i.e.,

$$\bar{H}_B^{Z_2} = \bar{H}_{0,B} + \bar{H}_{U,B}^{(2)} + \bar{H}_{U,B}^{(4)}. \quad (5.13)$$

One finds that the effective Hamiltonian (5.13) for the  $Z_2$  topological insulator has exactly the same form as the one encountered for the Chern insulator [Eq. (4.27)], with its terms  $\bar{H}_{0,B}$ ,  $\bar{H}_{U,B}^{(2)}$  and  $\bar{H}_{U,B}^{(4)}$  given by Eqs. (4.20), (4.23), and (4.24), respectively [see also Eqs. (4.25) and (4.26)]. The **major difference** being that for the desired excitations, ML or SL excitations, the appropriated fundamental functions  $F_{\alpha\beta,\mathbf{q}}^2$ ,  $g_\alpha(\mathbf{p}, \mathbf{q})$ , and  $\mathcal{G}_{\alpha\beta\alpha\sigma}(\mathbf{p}, \mathbf{q})$  should be properly used. We refer the reader to Appendix D for the complete expressions of the fundamental function  $F_{\alpha\beta,\mathbf{q}}^2$ ,  $g_\alpha(\mathbf{p}, \mathbf{q})$ , and  $\mathcal{G}_{\alpha\beta\alpha\sigma}(\mathbf{p}, \mathbf{q})$  in terms of the  $B_{i,\mathbf{k}}$  functions (3.25). Finally, the spin-wave excitation spectrum can be determined by treating the Hamiltonian (5.13) within a harmonic approximation, i.e.,

$$\bar{H}_B^{Z_2} \approx \bar{H}_{0,B} + \bar{H}_{U,B}^{(2)}, \quad (5.14)$$

where  $\bar{H}_{0,B}$  and  $\bar{H}_{U,B}^{(2)}$  are also given by Eqs. (4.20) and (4.23), respectively.

## 5.3 ML excitations

### 5.3.1 Spin waves at the flat band limit

The spin-wave spectrum for the correlated  $Z_2$  topological insulator follows from the diagonalization of the effective bosonic Hamiltonian (5.14). Using the same canonical transformation (4.30), we arrive at

$$\bar{H}_B^{Z_2} = E_0 + \sum_{\mu=\pm} \sum_{\mathbf{q} \in BZ} \Omega_{\mu,\mathbf{q}}^{Z_2} a_{\mu,\mathbf{q}}^\dagger a_{\mu,\mathbf{q}}, \quad (5.15)$$

where the constant  $E_0 = (-1.69 t_1)N$  and the dispersion relation of the bosons  $a_\pm$  reads

$$\Omega_{\pm,\mathbf{q}}^{Z_2} = \frac{1}{2} (\epsilon_{\mathbf{q}}^{00} + \epsilon_{\mathbf{q}}^{11}) \pm \frac{1}{2} \sqrt{(\epsilon_{\mathbf{q}}^{00} - \epsilon_{\mathbf{q}}^{11})^2 + 4\epsilon_{\mathbf{q}}^{01}\epsilon_{\mathbf{q}}^{10}}. \quad (5.16)$$

It is important to state again that Eqs. (5.15) and (5.16) that describe the spin-wave excitation spectrum for the  $Z_2$  topological insulator, have the same form as Eqs. (4.33) and (4.34) derived for the Chern insulator. Here, the appropriated fundamental functions  $F_{\alpha\beta,\mathbf{q}}^2$ ,  $g_\alpha(\mathbf{p}, \mathbf{q})$ , and  $\mathcal{G}_{\alpha\beta\alpha\sigma}(\mathbf{p}, \mathbf{q})$  for the ML excitations should be used [see Eqs. (5.6) and (5.7)].

As discussed in Sec.4.2.2, the effective bosonic Hamiltonian (4.28) for the correlated Chern insulator is non-Hermitian, with the functions  $\epsilon_{\mathbf{q}}^{01}$  and  $\epsilon_{\mathbf{q}}^{10}$  being complex quantities, but not complex conjugate to each other, a feature that was also found for ML excitations.

Now, the inclusion of such terms was fundamental to achieve the correct results for the Chern insulator as they yield the Dirac points at the  $K$  and  $K'$  points of the first Brillouin zone for the spin-wave spectrum, in agreement with the numerical calculations [29]. Therefore, we have used here the same methodology, i.e., we have included all quadratic coefficients  $\epsilon_{\mathbf{q}}^{\alpha\beta}$  [Eq. (4.25)] in the calculations. Moreover, the coefficients  $\bar{\omega}_{\mathbf{q}}^{\alpha\beta}$  [Eq. (4.21)],

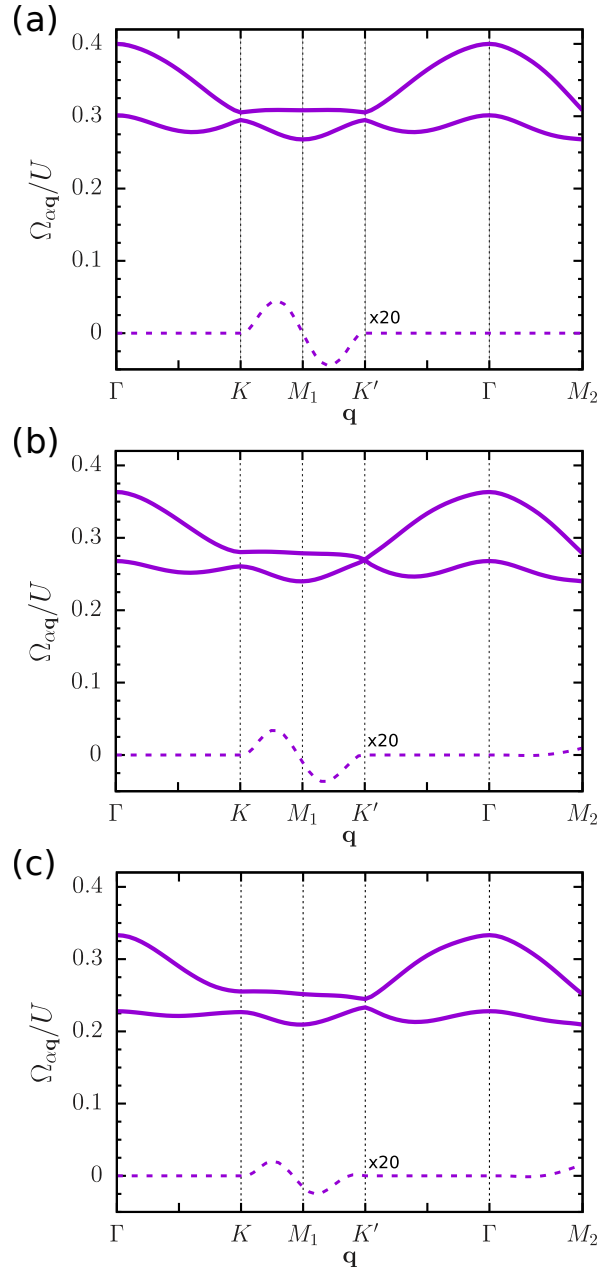


**Figure 5.1:** Spin-wave spectrum (5.16) of the **mixed lattice** excitations (5.4), calculated from the effective bosonic Hamiltonian within the harmonic approximation (5.14) and at the nearly flat band limit (3.18). Solid and dashed lines represent the spectrum real and imaginary parts, respectively, with a multiplicative factor 20 is employed for the imaginary part. The on-site repulsion energies are (a)  $U_A = U_B = U$ ; (b)  $U_B = 0.8 U_A = 0.8 U$  and (c)  $U_B = 0.6 U_A = 0.6 U$ . The path chosen in momentum space follows the highly symmetric points in the first Brillouin zone [Fig. 3.1(b)].

that come from the noninteracting Hamiltonian (4.20), are very small [see Figs. D.2(a) and (b)], thus we made the approximation  $\bar{\omega}_{\mathbf{q}}^{\alpha\beta} = 0$ , the same one used for the correlated Chern insulator calculations in Sec.3.1.1 and for the study of the square lattice  $\pi$ -flux model in Ref. [24] (further details can be found on Appendix D).

The spin-wave spectrum (5.16), at the nearly flat band limit (3.18), calculated for the ML excitations is shown in Fig. 5.1. In the first panel, where  $U_A = U_B$ , we can see that the real part of the spin-wave excitations (solid lines) is gapped and that the bands are separated from each other. This contrasts with the Haldane-Hubbard model for the Chern insulator discussed in Sec.4.2.2, where (i) a Goldstone mode is present [related to the fact that a SU(2) symmetry is broken], and (ii) there are Dirac points at the  $K$  and  $K'$  points connecting the upper and lower spin-wave bands. Fig. 5.1(b) and (c) show the behavior of the spin-wave spectrum when an imbalance in the on-site repulsion energies is considered. The used values are in order:  $U_B = 0.8U_A$  and  $U_B = 0.6U_A$ . Notice that, the higher the difference between the  $U_A$  and  $U_B$ , the lower the global energy is. Also, the energy gap at the  $K$  point increases with the imbalance. Making  $U_B > U_A$  (not shown here), we found that the energy gap at the  $K'$  point increases instead of the one at  $K$  point, but with the same overall intensity.

Additionally, the non-Hermiticity property of the Hamiltonian (5.14) implies that the spin-wave spectrum has also an imaginary part, although its contribution is rather small when compared to the real part, being evident only at the border of the Brillouin zone, as shown by the dashed lines in Figure 5.1. Such result can be interpreted as a magnon decay rate, although, as found for the Chern insulator in Sec. 3.1.1, it might be an artifact of the bosonization scheme. Concerning the contributions of the on-site energy imbalance for the imaginary part of the excitation spectrum (5.16), we found only a slight decrease in energy, matching the global decrease behavior of the real part. Although it appears that there is a gap closure at the  $K'$  point in Fig. 5.1(b), a small energy gap was found

$$\Delta^{(K)} = \Omega_{+,K} - \Omega_{-,K} = 1.04 \times 10^{-2} U. \quad (5.17)$$

Another interesting feature is that the upper band is almost flat at the border of the Brillouin zone ( $K \rightarrow M_1 \rightarrow K'$ ).

### 5.3.2 Spin waves away from the flat band limit

We also investigated how the spin waves alter when we move away from the nearly flat band limit. This was done by changing the values of the parameter  $t_2$  together with  $\phi$ . From Sec. 3.1.1, we know that the free-electronic spectrum becomes more dispersive when this perturbation is included and that the band gap between the upper and lower free-electronic bands vanishes at the  $K$  and  $K'$  points for  $\phi \rightarrow 0$ . We found very little changes in the spin-wave spectrum when increasing the absolute values of  $\phi$  with respect

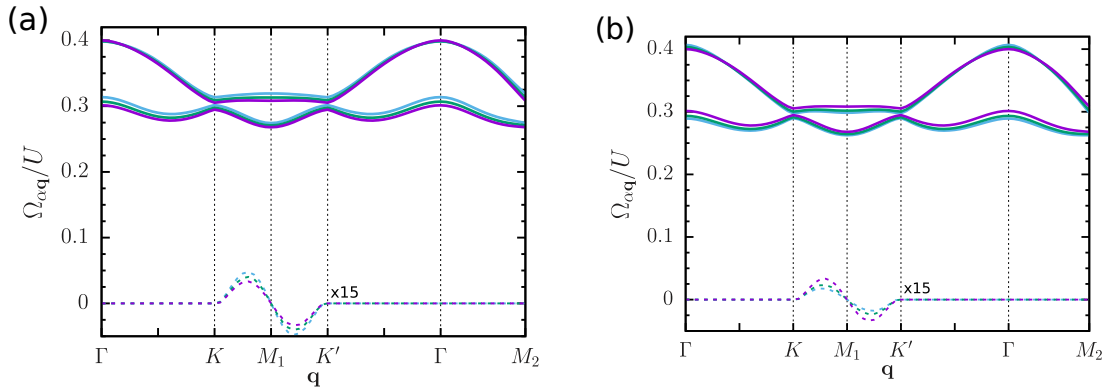


**Figure 5.2:** Spin-wave spectrum (5.16) of the **mixed lattice** excitations (5.4), calculated from the effective bosonic Hamiltonian at the harmonic approximation (5.14). Solid and dashed lines represent the spectrum real and imaginary parts, respectively, with a multiplicative factor 15 is present for the imaginary part. We have (a) descending and (b) ascending values of  $\phi$ , given by the sets  $\phi = 0.4, 0.5, 0.656$  and  $\phi = 0.656, 0.7, 0.8$ . The phase  $\phi = 0.655$  is represented by the solid magenta line in both panels, solid green line represents  $\phi = 0.5$  in panel (a) and  $\phi = 0.7$  in panel (b), and solid blue line represents  $\phi = 0.4$  in panel (a) and  $\phi = 0.8$  in panel (b), respectively. In both cases  $t_2$  is given by the relation  $\cos(\phi) = t_1/(4t_2)$ . The on-site repulsion energies is  $U_A = U_B = U$  in all cases and the path chosen in momentum space follows the highly symmetric points in the first Brillouin zone [Fig. 3.1(b)].

to the flat band limit  $\phi = 0.656$ , for fixed  $U_A = U_B = U$ , while maintaining the relation  $t_2 = t_1/\cos(\phi)$ , which was fixed by convenience. More notably, as can be seen in Fig. 5.2(a) for  $\phi = 0.7$  and  $0.8$ , there is a global positive shift for the lower band, while the upper band energy is increased only around the border of the first Brillouin zone. The imaginary part of the spectrum also slightly increases, following the same behavior of the real part. As shown in Fig. 5.2(b), a decreasing in the values of the phase  $\phi$  ( $\phi = 0.4$  and  $0.5$ ) yields an opposite effect, i.e, it adds a global negative shift to the lower band while the energies of the upper band decrease only around the first Brillouin zone border. Moreover, the decay rates also decrease with the decreasing of the phase  $\phi$ .

To conclude, we observed that the flat-band ferromagnetic phase of the  $Z_2$  topological insulator is stable when spin waves associated with the ML excitations (5.4) are considered. Such a feature is observed even when the system is slightly driven away from the nearly flat band limit.

## 5.4 SL excitations

### 5.4.1 Spin waves at the flat-band limit

As discussed in Sec. 5.2, a second set of boson operators can be defined for the correlated  $Z_2$  topological insulator. Such kind of excitations follow from the spin operators (5.9) that flip spins and preserve the sublattice index. In this case, the spin-wave spectrum can also be obtained from the effective bosonic Hamiltonian (5.14), but with the appropriate composing functions  $F_{\alpha\beta,\mathbf{q}}^2$ ,  $g_\alpha(\mathbf{p}, \mathbf{q})$ , and  $\mathcal{G}_{\alpha\beta a\sigma}(\mathbf{p}, \mathbf{q})$  that are given by Eqs. (5.6), (5.10), and (D.2), respectively. The full expression of the functions (5.6) and (D.2) in terms of the  $B_{i,\mathbf{k}}$  coefficients (3.25) of the canonical transformation (3.26) are given by Eqs. (D.8) and (D.9).

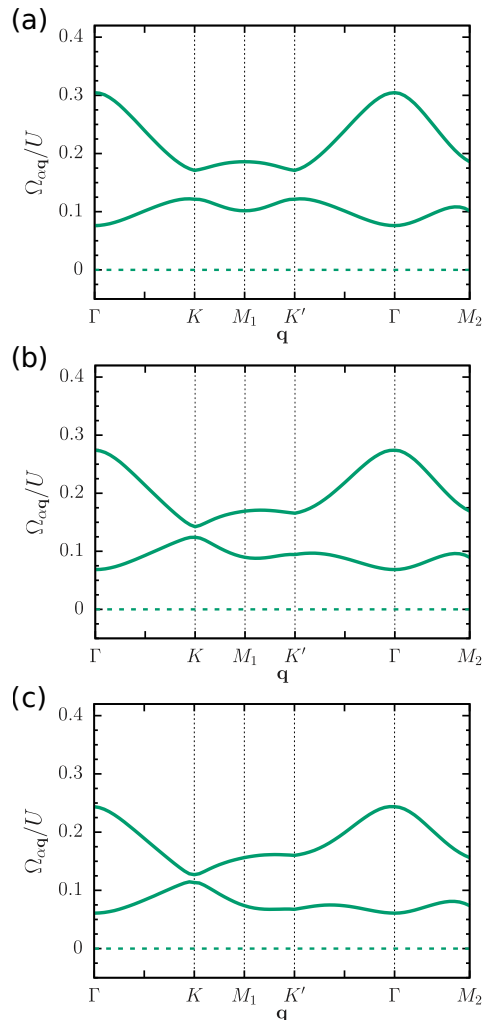


**Figure 5.3:** Spin-wave spectrum (5.16) of the **same lattice** excitations (5.9), calculated from the effective bosonic Hamiltonian harmonic approximation (5.14) at the nearly flat band limit (3.18). On-site repulsion energies (a)  $U_A = U_B = U$ ; (b)  $U_B = 0.8 U_A = 0.8 U$  and (c)  $U_B = 0.6 U_A = 0.6 U$ . The path chosen follows the highly symmetric points in the first Brillouin zone [Fig. 3.1(b)]. The imaginary part of the spectrum (dashed lines) is zero, but is shown for completeness.

Differently from the ML excitations discussed in the previous section, for the SL excitations, the kinetic coefficients (4.21) vanishes, i.e.,  $\bar{\omega}_{\mathbf{q}}^{\alpha\beta} = 0$ . Moreover, the quadratic term (4.23) of the effective boson model (5.14) is now Hermitian, since the coefficients  $\epsilon_{\mathbf{q}}^{\alpha\alpha}$  are real quantities while  $\epsilon_{\mathbf{q}}^{01}$  and  $\epsilon_{\mathbf{q}}^{10}$  are complex ones, but now  $\epsilon_{\mathbf{q}}^{01} = (\epsilon_{\mathbf{q}}^{10})^*$  [see Fig. D.3(c)]. Similarly to the ML excitations, for the SL excitations, the condition (4.29) is not fulfilled for all momenta within the first Brillouin zone as shown in Figs. D.3 (a) and (b).

After calculating the spin-wave spectrum (5.16) for the SL excitations (5.9) at the nearly flat band limit (3.18), we can see some distinct features as compared with the spin-wave spectrum of the ML excitations. As shown in the Fig. 5.3(a), the spin waves of the SL excitations have a lower energy and the bands are separated by a larger gap. In contrast, both ML and SL excitations have gapped spin-wave spectrum. Moreover, in the SL case, the Hamiltonian is Hermitian and, consequently, the energies of the spin waves are real, i.e., the imaginary part of the dispersion (5.16) vanishes.

When there is an imbalance on the Hubbard on-site repulsion energies  $U_A \neq U_B$ , the spin-wave spectrum modifies pretty much the same away as the ML excitation case, i.e., there is an increasing and decreasing of energy gaps between the lower and upper bands at the  $K$  and  $K'$  points, although here, the depreciation occurs at the  $K$  point instead of the  $K'$  one. Figures 5.3(b) and (c) shows this behavior for  $U_B = 0.8U_A$  and  $U_B = 0.6U_A$ , respectively. There is also a global energy shift in the spectrum, as can be seen by fixing the eye in a particular momentum, for example, the energy of the  $\Gamma$  point moves from around 0.1 to 0.07 in the lower band and from 0.3 to 0.26 in the upper band.

## 5.5 Spin waves away from the flat band limit

Again, to investigate the stability of the flat-band ferromagnetic phase, we pushed the system away from the flat band limit (3.18) by fixing the parameters  $U_A = U_B = U$  and  $t_2 = 4t_1/\cos(\phi)$  while varying  $\phi$ . The obtained results are shown in Fig. 5.4. In the first panel, Fig. 5.4(a), where the phase  $\phi$  is increased from  $\phi = 0.656$  to  $\phi = 0.7$  and  $0.8$ , we notice an increase in the energy around the  $\Gamma$  point of lower band. Another effect is that the energies around the  $K$  and  $K'$  points slightly decrease, with the energy gap between the lower and upper bands changing from  $\Delta^{(K)} = 4.96 \times 10^{-2}U$  for  $\phi = 0.656$  to  $\Delta^{(K)} = 5.34 \times 10^{-2}U$  with  $\phi = 0.8$ . The rest of the spin-wave spectrum retains its overall form when compared to the nearly flat limit (3.18), i.e.,  $\phi = 0.656$ . Interestingly, for  $\phi = 0.8$ , we note that the spin-wave spectrum becomes almost dispersionless, with the flatness ratio  $\sim 0.05/0.0125 = 4$ . Moreover, the minimum of the lower band changes from the  $\Gamma \rightarrow M$  point. Decreasing the values of the complex phase  $\phi$  from  $\phi = 0.656$  to  $\phi = 0.4$  and  $0.5$  [see Fig. 5.4(b)], we can see some effects in the upper and lower bands mostly around the  $\Gamma$  point of the first Brillouin zone, this time, making the bands repel each other. Moreover, the excitation energies around the  $K$  and  $K'$  points slightly increase

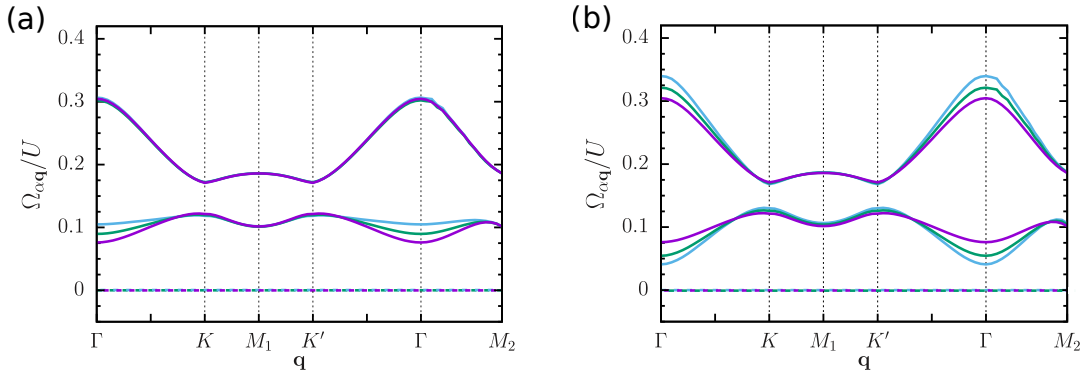


**Figure 5.4:** Spin wave spectrum (5.16) of the **same lattice** excitatons (5.9), calculated from the effective bosonic Hamiltonian harmonic approximation (5.14). We have (a) descending and (b) ascending values of  $\phi$ , given by the sets  $\phi = 0.4, 0.5, 0.656$  and  $\phi = 0.656, 0.7, 0.8$ . The phase  $\phi = 0.655$  is represented by the solid magenta line in both panels, solid green line represents  $\phi = 0.5$  in panel (a) and  $\phi = 0.7$  in panel (b), and solid blue lines represents  $\phi = 0.4$  in panel (a) and  $\phi = 0.8$  in panel (b), respectively. In both cases  $t_2$  is given by the relation  $\cos(\phi) = t_1/(4t_2)$ . The on-site repulsion energies is  $U_A = U_B = U$  in all cases and the path chosen in momentum space follows the highly symmetric points in the first Brillouin zone [Fig. 3.1(b)]. The imaginary part of the spectrum (dashed lines) is zero, but is shown for completeness.

changing the energy gap between the upper and lower bands to  $\Delta^{(K)} = 4.35 \times 10^{-2} U$  and  $\Delta^{(K)} = 3.81 \times 10^{-2} U$  for  $\phi = 0.4$  and  $0.5$ , respectively.

## 5.6 Mass term

Here, we briefly comment on the effects of a sublattice energy imbalance added to the system, a term that breaks lattice inversion symmetry. This can be done via the addition of the mass term (3.19) to the Hamiltonian (3.23). Its contribution can be easily treated as shown in Sec.4.2.3. The replacement (3.20) just slightly renormalizes the electronic spectrum, but has one major consequence that should be dealt with care, which is the splitting of the degeneracy between the spin- $\uparrow$  and the spin- $\downarrow$  free-electronic c bands. In principle, this asymmetry could destabilizes the ferromagnetic ground state. Nonetheless, as seen in Fig. 3.5, the electronic spectrum (3.14) with the modification (3.20) only mild violates the band degeneracy, specially when compared to the band width. Thus, for some small values of the parameter  $M$ , namely  $M = 0.05 t_1$  and  $M = 0.1 t_1$ , the free-electronic spectrum can still be within the bounds of the flat band limit. Therefore, we assumed that this difference would not affect the ferromagnetic ground state and we went on to calculated the spin-wave spectrum for both ML excitations (5.4) and SL excitations (5.9). For both types of excitations, the parameters  $\phi$  and  $t_2$  were set to their optimal flatness values (3.18), while the on-site repulsion energies were set to  $U_a = U_b = U$ . To analyze the effects on the spin-wave spectrum, the values of  $M$  were then slightly increased.

Firstly, for the ML excitation (5.4), increasing the on-site sublattice energy to  $M = 0.05 t_1$  implies a minor effect on the spin wave bands dispersion [calculated using (5.16)].

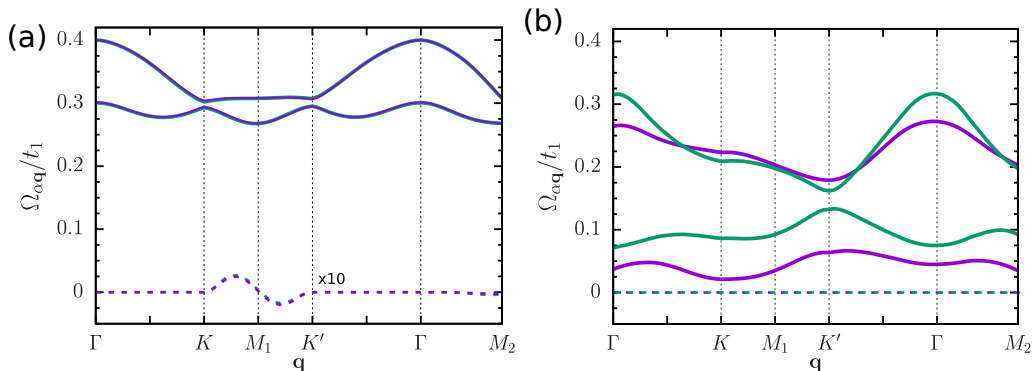


**Figure 5.5:** Spin-wave spectrum (5.16) of the (a) **mixed lattice** excitations (5.4) and of the (b) **same lattice** excitations (5.9), calculated from the effective bosonic Hamiltonian (4.28) at the harmonic approximation. With the parameters  $M = 0.05$  (solid green line) and  $M = 0.1$  (solid magenta line) and  $t_2$  and  $\phi$  given by the nearly-flat band limit (3.18). Solid and dashed lines represent the spectrum real and imaginary parts, respectively. The on-site repulsion energies are  $U_A = U_B = U$  in all cases and the path chosen in momentum space follows the highly symmetric points in the first Brillouin zone [Fig. 3.1(b)].

Even for  $M = 0.1 t_1$ , the effect remains small, with just a depreciation of the energy around the  $K$  point and an increase in the energy gap between the lower and upper bands at the  $K'$  point. Both cases are shown in Fig. 5.5(a). Also, rather small modifications were found for the imaginary part of the spectrum. Secondly, for the SL excitations (5.9) and for the same values of the parameter  $M$ , we obtained a very different result. As can be seen in Fig. 5.5(b), the spin-wave spectrum is highly sensible to this type of perturbation. Changing  $M$  just slightly increases the gap between the bands, which is made even larger for  $M = 0.1 t_1$ . We also note that, for the  $M = 0.1 t_1$  configuration, the cost of creating a particle with transfer momentum  $\mathbf{q} = K = (0, 4\pi/3\sqrt{3})$  is almost zero. This could indicate that the flat-band ferromagnetic ground state is only stable for tiny mass imbalances, since for large values of the mass an unrestrained number of excitations could proliferate in the system. If the parameter  $M$  is reversed into negative values, the effect is reversed between the  $K$  and  $K'$  points (not shown here). We point out that the changes caused by nonzero  $M$  are very similar to the ones caused by the imbalance between  $U_A$  and  $U_B$ . This signals that the sublattice characteristic are embedded in the  $K$  and  $K'$  points, and that inversion symmetry plays a major role in the gap closing mechanism.

## 5.7 Chern numbers of the spin-wave bands

Finally, we want to discuss the topological properties of the spin-wave excitations. In principle, one would expect that the nontrivial topological properties of the noninteracting electronic bands of the Haldane-Hubbard model may yield a flat-band ferromagnetic phase with topologically nontrivial spin-wave excitation bands. Indeed, topological magnons in

Heisenberg ferromagnets [58, 59, 60, 61, 62, 63] and, in particular, magnets on a honeycomb lattice [60, 61, 62, 63] have been studied. An important ingredient for such topological magnon insulators is the Dzyaloshinskii-Moriya interaction that may open energy gaps in the magnon spectrum and yields magnon bands with nonzero Chern numbers.

For the correlated Chern insulator described by the Haldane-Hubbard model (3.1) at the nearly flat-band limit (3.18), it was shown that the spin-wave excitation bands have nonzero Chern numbers only when the dispersion of the noninteracting electronic bands is explicitly taking into account (see Figs. 2(a<sub>1</sub>), (a<sub>2</sub>) and (d) from [29]). In this work, we have calculate the Chern numbers of the spin-wave bands for configurations of the Haldane-Hubbard model whose spin-wave spectrum displays an energy gap at the  $K$  and  $K'$  points, i.e., for configurations whose on-site repulsion energies  $U_A \neq U_B$ , see Figs. 4.3(b) and (c). To do so, we expand the Hamiltonian (4.28) in terms of Pauli matrices as done in Eq. (3.9), determine the corresponding  $B_{i,\mathbf{q}}$  coefficients assuming that

$$\epsilon_{\mathbf{q}}^{01} = (\epsilon_{\mathbf{q}}^{10})^*, \quad (5.18)$$

and calculate the Chern numbers using Eq. (3.15) (see Appendix F for details). In agreement with the exact diagonalization results [29], we find that the Chern numbers of the spin-wave bands vanish for the flat band limit.

For the  $Z_2$  topological insulator, the Chern numbers were calculated using the same procedure, i.e., by casting the effective bosonic Hamiltonian (5.14) into an expansion in terms of Pauli matrices, and then numerically evaluating Eq. (3.15) to finding the Chern number (see Appendix F for details). As stated above, such procedure involves making the assumption (5.18), which holds true for the SL excitations, but does not for the ML excitations. Nevertheless, numerically calculated Chern numbers for the lower and upper spin-wave bands are given in Table 5.1. There, we can see that, for the SL type of excitation, the numerically calculated values are close to one, for both homogeneous ( $U_A = U_B = U$ ) and imbalanced ( $U_A \neq U_B$ ) Hubbard interactions. Indeed, this could indicates that the spin-wave bands (5.16) of the SL excitations (5.9), at the nearly flat band limit, are topological in nature. A finite Chern number for the spin-wave bands implies that, at appropriate filling, a thermal Hall effect might be observed in the system [64]. For the ML excitations (5.4), the calculated number are neither close to 0 nor 1, therefore, leaving the value of the Chern number inconclusive. We believe that this

**Table 5.1:** Chern numbers of the lower and upper spin-wave bands (5.16) for both the ML ( $C_{ML}$ ) and the SL ( $C_{SL}$ ) excitations at the nearly flat band limit (3.18).

	$U_A = U_B = U$	$U_B = 0.8 U_A = 0.8 U$
$C_{ML}$	$\pm 0.29$	$\pm 0.18$
$C_{SL}$	$\pm 1.17$	$\pm 1.08$

uncertainty might be related to the fact that the approximation (5.18) had to be made, leading to an imprecise Berry curvature (3.16), and therefore, affecting our numerical calculations.

# Chapter 6

## Summary and conclusion

To summarize, we investigated a flat-band ferromagnetic phase of a correlated Chern and  $Z_2$  topological insulators on a honeycomb lattice, using a bosonization scheme procedure that was used to describe a correlated Chern insulator and a correlated  $Z_2$  topological insulator on a square lattice [24]. Here we considered a spinfull Haldane-Hubbard model to describe both Chern and  $Z_2$  topological insulators. In the noninteracting limit, the model presents two doubly spin-degenerated electronic bands and, by fine tuning the model parameters, we were able to show that the two lower bands become almost flat, which we refer in the main text as the nearly flat band limit (3.18). At the nearly flat band limit (3.18) and at half filling of the lower free-electronic bands (quarter filling of all bands), the ground state of the system is spin polarized. We used this spin-polarized ground state as a reference state to the bosonization scheme and then defined boson operators that represent the low energy spin-wave excitations above such spin-polarized ground state. To define the boson operators for both the Chern insulator and the  $Z_2$  topological insulators, we used the same definition as done for the  $\pi$ -flux model on a square lattice [24]. Surprisingly, for the honeycomb lattice, another set of bosons were found for the  $Z_2$  topological insulator. The appearance of these two types of excitations [the ML excitations (5.4) and the SL excitations (5.9)] is one of the major differences between the application of the bosonization formalism for the Haldane-Hubbard model and for the  $\pi$ -flux model on the square lattice [24]. Here in this thesis, the two types of excitations were treated separately, but a more elaborate approach treating both set of bosons simultaneously would be desired. Of course, the bosonization scheme would need adaptations to support such treatment. As far as we know, our method is the first one to address the spin-wave spectrum for a correlated  $Z_2$  topological insulator on a honeycomb lattice described by a Haldane-Hubbard model [35].

Furthermore, another adaptations were need to properly apply the bosonization scheme for the Haldane-Hubbard model on the honeycomb lattice. For example, the condition (4.29), that is fully satisfied for the  $\pi$ -flux model on a square lattice [24], is violated for

some momenta on the honeycomb lattice [see Fig. C.1(b)]. This implies that the two sets of bosons operators (4.11) and (5.3), respectively defined for the Chern and  $Z_2$  topological insulators, are only approximately independent [see also Eq. (B.3)]. Nevertheless, we assumed that the defined boson operators indeed obey the usual bosonic canonical commutation relations [see Eq. (4.12)] and proceeded with the bosonization scheme, adding electron-electron interactions via a Hubbard term, and then, mapping the projected interacting fermionic Hamiltonian into an effective interacting bosonic one. At the harmonic approximation [Eqs. (4.28) and (5.14)] of the effective bosonic Hamiltonian [Eqs. (4.27) and (5.13)], the spin-wave spectrum was determined. At the nearly flat-band limit, the calculated spin-wave spectrum for the Chern insulator (Fig. 4.3) yields results that qualitatively agreed with the ones calculated via the exactly diagonalization technique [29], i.e., the presence of Dirac points (for the homogeneous on-site repulsion energies  $U_A = U_B$ ) and a Goldstone mode, being the second feature a characteristic of a (flat-band) ferromagnetic phase [see also Fig. 4.4].

Also, at the nearly flat band limit (3.18), we considered the effects of different Hubbard repulsion energies for two triangular sublattices. This breaks the lattice inversion symmetry and, for the correlated Chern insulator, gaps out the Dirac cones of the spin-wave spectrum, which also qualitatively agrees with literature results [29]. One difference though, was that a finite decay rate was found in our spectrum, a feature not presented in the exact diagonalization results [29] [compare Figs. 4.3 and 4.4]. For now, we are not sure if this is an artifact of the bosonization scheme for the Haldane-Hubbard model on a honeycomb lattice. One possibility is due to the fact that condition (4.29) is not satisfied, some errors are introduced into the calculations. Nonetheless, this signals that, although some considerations have to be made for the bosonization scheme to be applied to Haldane-Hubbard model on the honeycomb lattice, reasonable results can be extracted at this level of approximation. We also probed the stability of the flat-band ferromagnetic ground state by slightly modifying the model parameters, so that the noninteracting lower  $c$  bands become more dispersive. In most of the modifications, the ferromagnetic ground state seemed to be stable, becoming unstable only when a sublattice dependent on-site energy (mass term) was added.

For the correlated  $Z_2$  topological insulator, we have calculated the spin-wave for both the ML and SL excitations. In contrast with the correlated Chern insulator, we found that the spin-wave spectrum does not have Dirac points. Moreover, all the excitations are gapped, with no Goldstone mode present, a feature that reflects the symmetries preserved by the  $Z_2$  topological insulator (compare Figs. 4.3, 5.1, and 5.3). The flat-band ferromagnetic ground state seemed to be stable even when the system was driven away from the flat band limit. Therefore, the results for the  $Z_2$  topological insulator indicate that the ferromagnetism should be stable in the vicinity of the nearly flat band limit (3.18). The same conclusion can be made for the Chern insulator if the mass term (3.19)

is not included.

Another result that should be pointed out is the topological properties of the spin-wave spectrum. Reference [29] has showed that topological magnon bands could exist in a Chern insulator described by the Haldane-Hubbard model when the dispersion of the noninteracting bands is taken into account. They also showed that, for the flat-band limit (3.18), the Chern numbers of the spin-wave bands vanish, and this is exactly what we found within our calculations. We believe that the dispersion of the noninteracting electronic bands is only partially taken into account within the bosonization scheme, and some modifications should be need to account for this fact. Even though the mapping of the free Hamiltonian to its bosonic version (4.20) yield nonzero values for the coefficients (4.21), they were very small when compared to the contribution (4.25) coming from the Hubbard interaction [see Figs. 4.2 and D.2]. A proper modification of the bosonization scheme is needed in order to include the explicit contributions of the dispersion of the free-electronic bands. In contrast with the results for the correlated Chern insulator, we found indications that the spin-wave bands of the correlated  $Z_2$  topological insulator might be topologically nontrivial even at the nearly flat-band limit. Although the results for the Chern numbers of the spin-wave bands of the ML excitations were inconclusive, for the SL excitations, we found that the spin-wave bands have Chern numbers  $C_{SL} \approx 1$ .

We believe that the bosonization scheme discussed in this thesis could be used to describe other lattice models and, in particular, can be used to treat correlated flat band topological systems. As commented on Chapter 2, tight-binding models on the square, kagome, and honeycomb lattices, different from the one presented here, can host topological flat bands and, at an appropriate filling and sufficient strong  $U$  interaction, may host a stable flat-band ferromagnetic ground state. It would also be interesting to see whether the bosonization formalism [24], eventually combined with the approximations discussed for the Chern insulator honeycomb lattice [34], can also be employed to study twisted bilayer graphene near a magic angle [65, 66, 67, 68, 69, 70, 71, 72]. Here the resulting moiré pattern induces an effective superlattice and a set of flat-minibands in the moiré Brillouin zone. In addition to a superconducting phase [65, 66], evidences for a ferromagnetic phase at 3/4-filling of the conduction miniband are also found [67]. In principle, a possible flat-band ferromagnetic phase of the effective lattice model introduced in Ref. [71] for twisted bilayer graphene could be studied within the bosonization scheme.

To conclude, this work showed that the study of topological models with different band fillings could lead to more distinct topological phases. Although it is difficult to create materials with fine tuned parameters to further investigate these phases, cold atom systems on optical lattices could be a good approach to test these results.

# Bibliography

- [1] König, M. *et al.* Quantum spin Hall insulator state in HgTe quantum wells. *Science* **318**, 766–770 (2007).
- [2] Hasan, M. Z. & Kane, C. L. Colloquium: topological insulators. *Reviews of Modern Physics* **82**, 3045 (2010).
- [3] Kane, C. L. & Mele, E. J. Quantum spin Hall effect in graphene. *Physical Review Letters* **95**, 226801 (2005).
- [4] v. Klitzing, K., Dorda, G. & Pepper, M. New Method for High-Accuracy Determination of the Fine-Structure Constant Based on Quantized Hall Resistance. *Physical Review Letters* **45**, 494–497 (1980).
- [5] Haldane, F. D. M. Model for a quantum Hall effect without Landau levels: Condensed-matter realization of the "parity anomaly". *Physical Review Letters* **61**, 2015 (1988).
- [6] Qi, X.-L. & Zhang, S.-C. Topological insulators and superconductors. *Reviews of Modern Physics* **83**, 1057–1110 (2011).
- [7] Marcel Franz, L. M. C. L. K. (ed.) *Topological Insulators: Contemporary Concepts of Condensed Matter Science* (Elsevier Science and Techn., 2013).
- [8] Rachel, S. Interacting topological insulators: a review. *Reports on Progress in Physics* **81**, 116501 (2018).
- [9] Thouless, D. J., Kohmoto, M., Nightingale, M. P. & den Nijs, M. Quantized Hall Conductance in a Two-Dimensional Periodic Potential. *Physical Review Letters* **49**, 405–408 (1982).
- [10] Kohmoto, M. Topological invariant and the quantization of the Hall conductance. *Annals of Physics* **160**, 343–354 (1985).

- [11] Jotzu, G. *et al.* Experimental realization of the topological Haldane model with ultracold fermions. *Nature* **515**, 237–240 (2014).
- [12] Goldman, N., Budich, J. C. & Zoller, P. Topological quantum matter with ultracold gases in optical lattices. *Nature Physics* **12**, 639–645 (2016).
- [13] Cooper, N., Dalibard, J. & Spielman, I. Topological bands for ultracold atoms. *Reviews of Modern Physics* **91**, 015005 (2019).
- [14] Fu, L. & Kane, C. L. Topological insulators with inversion symmetry. *Physical Review B* **76**, 045302 (2007).
- [15] Liu, C., Hughes, T. L., Qi, X.-L., Wang, K. & Zhang, S.-C. Quantum spin hall effect in inverted type-ii semiconductors. *Physical review letters* **100**, 236601 (2008).
- [16] Roth, A. *et al.* Nonlocal transport in the quantum spin hall state. *Science* **325**, 294–297 (2009).
- [17] Chiu, C.-K., Yao, H. & Ryu, S. Classification of topological insulators and superconductors in the presence of reflection symmetry. *Physical Review B* **88**, 075142 (2013).
- [18] Neupert, T., Santos, L., Chamon, C. & Mudry, C. Fractional quantum Hall states at zero magnetic field. *Physical Review Letters* **106**, 236804 (2011).
- [19] Sun, K., Gu, Z., Katsura, H. & Sarma, S. D. Nearly flatbands with nontrivial topology. *Physical Review Letters* **106**, 236803 (2011).
- [20] Tang, E., Mei, J.-W. & Wen, X.-G. High-temperature fractional quantum Hall states. *Physical Review Letters* **106**, 236802 (2011).
- [21] Neupert, T., Santos, L., Ryu, S., Chamon, C. & Mudry, C. Topological Hubbard model and its high-temperature quantum Hall effect. *Physical Review Letters* **108**, 046806 (2012).
- [22] Neupert, T., Chamon, C., Iadecola, T., Santos, L. H. & Mudry, C. Fractional (Chern and topological) insulators. *Physica Scripta* **2015**, 014005 (2015).
- [23] Hohenadler, M. & Assaad, F. F. Correlation effects in two-dimensional topological insulators. *Journal of Physics: Condensed Matter* **25**, 143201 (2013).
- [24] Doretto, R. & Goerbig, M. Flat-band ferromagnetism and spin waves in topological Hubbard models. *Physical Review B* **92**, 245124 (2015).
- [25] Doretto, R., Caldeira, A. & Girvin, S. Lowest Landau level bosonization. *Physical Review B* **71**, 045339 (2005).

- [26] Doretto, R. & Smith, C. M. Quantum Hall ferromagnetism in graphene: SU (4) bosonization approach. *Physical Review B* **76**, 195431 (2007).
- [27] Doretto, R., Smith, C. M. & Caldeira, A. Finite-momentum condensate of magnetic excitons in a bilayer quantum Hall system. *Physical Review B* **86**, 035326 (2012).
- [28] Su, X.-F., Gu, Z.-L., Dong, Z.-Y., Yu, S.-L. & Li, J.-X. Ferromagnetism and spin excitations in topological Hubbard models with a flat band. *Physical Review B* **99**, 014407 (2019).
- [29] Gu, Z.-L., Dong, Z.-Y., Yu, S.-L. & Li, J.-X. Itinerant topological magnons in Haldane Hubbard model with a nearly-flat electron band. *arXiv preprint arXiv:1908.09255* (2019).
- [30] Gu, Z.-L. & Li, J.-X. Itinerant Topological Magnons in SU(2) Symmetric Topological Hubbard Models with Nearly Flat Electronic Bands. *Chinese Physics Letters* **38**, 057501 (2021).
- [31] Rachel, S. & Le Hur, K. Topological insulators and Mott physics from the Hubbard interaction. *Physical Review B* **82**, 075106 (2010).
- [32] Zheng, D., Zhang, G.-M. & Wu, C. Particle-hole symmetry and interaction effects in the Kane-Mele-Hubbard model. *Physical Review B* **84**, 205121 (2011).
- [33] Hohenadler, M. *et al.* Quantum phase transitions in the Kane-Mele-Hubbard model. *Physical Review B* **85**, 115132 (2012).
- [34] Leonardo S. G. Leite and R. L. Doretto. Flat-band ferromagnetism and spin waves in the Haldane-Hubbard model. *Physical Review B* **104**, 155129 (2021).
- [35] Leonardo S. G. Leite and R. L. Doretto. Flat-band ferromagnetism in a correlated topological insulator on a honeycomb lattice. *In preparation* (2022).
- [36] Young, H. D., Freedman, R. A. & Ford, A. L. *Sears and Zemansky's university physics*, vol. 1 (Pearson education, 2006).
- [37] Kittel, C. & McEuen, P. *Kittel's Introduction to Solid State Physics* (John Wiley & Sons, 2018).
- [38] Vanderbilt, D. *Berry Phases in Electronic Structure Theory* (Cambridge University Press, 2019).
- [39] Tong, D. Lectures on the quantum Hall effect. *arXiv preprint arXiv:1606.06687* (2016).

- [40] Xiao, D., Chang, M.-C. & Niu, Q. Berry phase effects on electronic properties. *Reviews of Modern Physics* **82**, 1959–2007 (2010).
- [41] Qi, X.-L. & Zhang, S.-C. The quantum spin Hall effect and topological insulators. *arXiv preprint arXiv:1001.1602* (2010).
- [42] Aharonov, Y. & Bohm, D. Significance of Electromagnetic Potentials in the Quantum Theory. *Physical Review* **115**, 485–491 (1959).
- [43] Hickey, C., Rath, P. & Paramakanti, A. Competing chiral orders in the topological Haldane-Hubbard model of spin-1/2 fermions and bosons. *Physical Review B* **91**, 134414 (2015).
- [44] Tasaki, H. Stability of ferromagnetism in Hubbard models with nearly flat bands. *Journal of Statistical Physics* **84**, 535–653 (1996).
- [45] Mielke, A. & Tasaki, H. Ferromagnetism in the Hubbard model. *Communications in Mathematical Physics* **158**, 341–371 (1993).
- [46] He, J., Kou, S.-P., Liang, Y. & Feng, S. Chiral spin liquid in a correlated topological insulator. *Physical Review B* **83**, 205116 (2011).
- [47] He, J., Zong, Y.-H., Kou, S.-P., Liang, Y. & Feng, S. Topological spin density waves in the Hubbard model on a honeycomb lattice. *Physical Review B* **84**, 035127 (2011).
- [48] Maciejko, J. & Rüegg, A. Topological order in a correlated Chern insulator. *Physical Review B* **88**, 241101 (2013).
- [49] Hickey, C., Cincio, L., Papić, Z. & Paramakanti, A. Haldane-Hubbard Mott insulator: From tetrahedral spin crystal to chiral spin liquid. *Physical Review Letters* **116**, 137202 (2016).
- [50] Zheng, W., Shen, H., Wang, Z. & Zhai, H. Magnetic-order-driven topological transition in the Haldane-Hubbard model. *Physical Review B* **91**, 161107 (2015).
- [51] Vanhala, T. I. *et al.* Topological Phase Transitions in the Repulsively Interacting Haldane-Hubbard Model. *Physical Review Letters* **116**, 225305 (2016).
- [52] Wu, J., Faye, J. P. L., Sénéchal, D. & Maciejko, J. Quantum cluster approach to the spinful Haldane-Hubbard model. *Physical Review B* **93**, 075131 (2016).
- [53] Arun, V. S., Sohal, R., Hickey, C. & Paramakanti, A. Mean field study of the topological Haldane-Hubbard model of spin-1/2 fermions. *Physical Review B* **93**, 115110 (2016).

- [54] Imriška, J., Wang, L. & Troyer, M. First-order topological phase transition of the Haldane-Hubbard model. *Physical Review B* **94**, 035109 (2016).
- [55] Kusakabe, K. & Aoki, H. Ferromagnetic spin-wave theory in the multiband Hubbard model having a flat band. *Physical Review Letters* **72**, 144 (1994).
- [56] Kusakabe, K. & Aoki, H. Robustness of the ferromagnetism in flat bands. *Physica B: Condensed Matter* **194-196**, 215–216 (1994).
- [57] Müller, P., Richter, J. & Derzhko, O. Hubbard models with nearly flat bands: Ground-state ferromagnetism driven by kinetic energy. *Physical Review B* **93**, 144418 (2016).
- [58] Zhang, L., Ren, J., Wang, J.-S. & Li, B. Topological magnon insulator in insulating ferromagnet. *Physical Review B* **87**, 144101 (2013).
- [59] Malki, M. & Uhrig, G. Topological magnon bands for magnonics. *Physical Review B* **99**, 174412 (2019).
- [60] Owerre, S. A first theoretical realization of honeycomb topological magnon insulator. *Journal of Physics: Condensed Matter* **28**, 386001 (2016).
- [61] Owerre, S. Topological honeycomb magnon Hall effect: A calculation of thermal Hall conductivity of magnetic spin excitations. *Journal of Applied Physics* **120**, 043903 (2016).
- [62] Chen, L. *et al.* Topological Spin Excitations in Honeycomb Ferromagnet CrI<sub>3</sub>. *Physical Review X* **8**, 041028 (2018).
- [63] Mook, A., Plekhanov, K., Klinovaja, J. & Loss, D. Interaction-Stabilized Topological Magnon Insulator in Ferromagnets. *Physical Review X* **11**, 021061 (2021).
- [64] Murakami, S. & Okamoto, A. Thermal Hall effect of magnons. *Journal of the Physical Society of Japan* **86**, 011010 (2017).
- [65] Cao, Y. *et al.* Unconventional superconductivity in magic-angle graphene superlattices. *Nature* **556**, 43–50 (2018).
- [66] Lu, X. *et al.* Superconductors, orbital magnets and correlated states in magic-angle bilayer graphene. *Nature* **574**, 653–657 (2019).
- [67] Sharpe, A. L. *et al.* Emergent ferromagnetism near three-quarters filling in twisted bilayer graphene. *Science* **365**, 605–608 (2019).

- [68] Morell, E. S., Correa, J. D., Vargas, P., Pacheco, M. & Barticevic, Z. Flat bands in slightly twisted bilayer graphene: Tight-binding calculations. *Physical Review B* **82**, 121407 (2010).
- [69] Xu, C. & Balents, L. Topological Superconductivity in Twisted Multilayer Graphene. *Physical Review Letters* **121**, 087001 (2018).
- [70] Wu, F., MacDonald, A. & Martin, I. Theory of Phonon-Mediated Superconductivity in Twisted Bilayer Graphene. *Physical Review Letters* **121**, 257001 (2018).
- [71] Seo, K., Kotov, V. N. & Uchoa, B. Ferromagnetic Mott state in Twisted Graphene Bilayers at the Magic Angle. *Physical Review Letters* **122**, 246402 (2019).
- [72] Chen, B.-B. *et al.* Realization of topological Mott insulator in a twisted bilayer graphene lattice model. *Nature Communications* **12** (2021).

# Appendix

# Appendix A

## Spin symmetry of the noninteracting topological model

The presence of the Goldstone mode in the spin-wave spectrum for the Chern insulator [see Fig.4.3] is directly related to the fact the spin polarized ground state breaks a continuous spin symmetry present in the Hamiltonian. Here, we apply the same steps used by Doretto and Goerbig [24] to calculate the spin symmetry of the model Hamiltonians (3.1) and (3.23) that describe the Chern and the  $Z_2$  topological insulators, respectively.

First, we note that both Hamiltonians (3.1) and (3.23) can be written as

$$\mathcal{H}_0 = \sum_{\mathbf{k}\sigma} \sum_{a,b} E_{ab}^\sigma(\mathbf{k}) c_{\mathbf{k}a\sigma}^\dagger c_{\mathbf{k}b\sigma}. \quad (\text{A.1})$$

By comparing Eq.(A.1) with Eqs.(3.5)-(3.7) for the Chern insulator (broken time-reversal symmetry), we see that the relation  $h_{\mathbf{k}}^\uparrow = h_{\mathbf{k}}^\downarrow$  implies that the coefficients in (A.1) obey the following relations

$$E_{aa}^\uparrow(\mathbf{k}) = E_{aa}^\downarrow(\mathbf{k}) \quad \text{and} \quad E_{ab}^\uparrow(\mathbf{k}) = E_{ab}^\downarrow(\mathbf{k}), \quad (\text{A.2})$$

that will be useful in the calculation of the commutator  $[\mathcal{H}_0, \mathbf{S}]$ . When time-reversal symmetry is preserved, i.e., for the  $Z_2$  topological insulator, the relation  $h_{\mathbf{k}}^\uparrow = (h_{-\mathbf{k}}^\downarrow)^*$  implies that

$$E_{aa}^\uparrow(\mathbf{k}) = E_{aa}^\downarrow(\mathbf{k}) \quad \text{and} \quad E_{ab}^\uparrow(\mathbf{k}) \neq E_{ab}^\downarrow(\mathbf{k}). \quad (\text{A.3})$$

The usual total spin operator can be written in terms of the Abrikosov fermions (5.5) (with  $a = b$ ) as

$$\mathbf{S} = \sum_{i,a} S_{i,a}^j \hat{e}_j = \frac{1}{2} \sum_{k,a} \sum_{\sigma\sigma'} c_{\mathbf{k}a\sigma}^\dagger \hat{\sigma}_{\sigma,\sigma'} c_{\mathbf{k}a\sigma'}, \quad (\text{A.4})$$

where  $S_{i,a}^j$  is the  $j$ -th component of the spin operator in the site  $i$  of the sublattice  $a$ ,  $\hat{e}_j$  is the unitary Cartesian direction and  $\hat{\sigma}$  is the Pauli matrices vector. With the aid of (A.1)

and (A.4), it is easy to show that

$$[\mathcal{H}_0, S^z] = 0, \quad (\text{A.5})$$

and

$$\begin{aligned} [\mathcal{H}_0, S^+] = \sum_k \sum_a [E_{\uparrow}^{aa}(\mathbf{k}) - E_{\downarrow}^{aa}(\mathbf{k})] c_{\mathbf{k}a\uparrow}^{\dagger} c_{\mathbf{k}a\downarrow} + [E_{\uparrow}^{AB}(\mathbf{k}) - E_{\downarrow}^{AB}(\mathbf{k})] c_{\mathbf{k}A\uparrow}^{\dagger} c_{\mathbf{k}B\downarrow} \\ + [E_{\uparrow}^{BA}(\mathbf{k}) - E_{\downarrow}^{BA}(\mathbf{k})] c_{\mathbf{k}B\uparrow}^{\dagger} c_{\mathbf{k}A\downarrow}. \end{aligned} \quad (\text{A.6})$$

Substituting Eq.(A.2) in (A.6), one notices that the Hamiltonian that describes the Chern insulator [Eq.(3.1)] commutes with all components of the total spin operator. Physically, this means that the Hamiltonian (3.1) is invariant with respect to the direction that the spins are pointing, i.e., it possesses  $SU(2)$  rotation symmetry. Again, as the ground state is spin polarized, the  $SU(2)$  symmetry is then reduced and a Goldstone mode (zero energy mode) is expected to occur at the spin wave spectrum (see Fig.4.3).

In contrast, (A.2), (A.5), and (A.6) imply that the  $Z_2$  topological insulator Hamiltonian (3.23) does not commute with the  $S^x$  and  $S^y$  components of spin. Therefore, the Hamiltonian is only symmetric with respect to the  $S^z$  component, i.e., possesses an  $U(1)$  rotation symmetry. This is the same symmetry of the spin polarized ground state (3.31), and therefore, the spin-wave excitations are expected to be gapped (see Fig.5.1 and 5.3).

# Appendix B

## Details about the bosonization scheme

In this Appendix, we provide some details about the definition of the boson operators (4.11) and discuss the differences between the application of the bosonization formalism for the Haldane model and the square lattice  $\pi$ -flux model [24]. Indeed, the application of the bosonization scheme [24] for the Haldane model on a honeycomb lattice requires further approximations as compare to the case of the square lattice  $\pi$ -flux model. We concentrate on the bozonization scheme for the Chern insulator. This Appendix is based on Ref. [24]

### B.1 About the condition (4.29)

As mentioned in Sec. 4.2, the boson operators (4.11) are defined in terms of projected spin operators in momentum space:

$$b_{\alpha,\mathbf{q}} \propto \bar{S}_{-\mathbf{q},\alpha}^+ \quad \text{and} \quad b_{\alpha,\mathbf{q}}^\dagger \propto \bar{S}_{\mathbf{q},\alpha}^-.$$

In terms of the fermion operators  $c_{\mathbf{k}\sigma}^\dagger$  and  $c_{\mathbf{k}\sigma}$  (associated with the lower noninteracting band  $c$ ), the commutator between the projected spin operators  $\bar{S}_{-\mathbf{q},\alpha}^+$  and  $\bar{S}_{\mathbf{q},\alpha}^-$  reads

$$[\bar{S}_{\mathbf{q},\alpha}^+, \bar{S}_{\mathbf{q}',\beta}^-] = \sum_{\mathbf{p}} \left[ g_\alpha(\mathbf{p} - \mathbf{q}', \mathbf{q}) g_\beta(\mathbf{p}, \mathbf{q}') c_{\mathbf{p}-\mathbf{q}-\mathbf{q}'\uparrow}^\dagger c_{\mathbf{p}\uparrow} - g_\alpha(\mathbf{p}, \mathbf{q}) g_\beta(\mathbf{p} - \mathbf{q}, \mathbf{q}') c_{\mathbf{p}-\mathbf{q}-\mathbf{q}'\downarrow}^\dagger c_{\mathbf{p}\downarrow} \right], \quad (\text{B.1})$$

with the  $g_\alpha(\mathbf{p}, \mathbf{q})$  function giving by Eq. (4.16). One sees that Eq. (B.1) is different from the canonical commutation relation (4.12) for boson operators. However, as long as we are close to the ferromagnetic state (3.31), i.e., the number of particle-hole pair excitations is

small, one can assume that

$$\begin{aligned} c_{\mathbf{p}-\mathbf{q}\uparrow}^\dagger c_{\mathbf{p}\uparrow} &\approx \langle \text{FM} | c_{\mathbf{p}-\mathbf{q}\uparrow}^\dagger c_{\mathbf{p}\uparrow} | \text{FM} \rangle = \delta_{\mathbf{q},0}, \\ c_{\mathbf{p}-\mathbf{q}\downarrow}^\dagger c_{\mathbf{p}\downarrow} &\approx \langle \text{FM} | c_{\mathbf{p}-\mathbf{q}\downarrow}^\dagger c_{\mathbf{p}\downarrow} | \text{FM} \rangle = 0, \end{aligned} \quad (\text{B.2})$$

and therefore, the commutator (B.1) now reads

$$[\bar{\mathbf{S}}_{\mathbf{q},\alpha}^+, \bar{\mathbf{S}}_{\mathbf{q}',\beta}^-] \approx \delta_{\mathbf{q},-\mathbf{q}'} F_{\alpha\beta,\mathbf{q}}^2, \quad (\text{B.3})$$

where the  $F_{\alpha\beta,\mathbf{q}}$  function is defined by Eq. (4.15). The commutator (B.3) indicates that the particle-hole pair excitations (4.10) can be treated approximated as bosons. The bosonization formalism for flat-band Chern insulators [24] is indeed based on the assumption (B.2).

For the square lattice  $\pi$ -flux model [24], it was found that the condition (4.29) holds, and therefore, Eq. (B.3) allows us to define two sets of *independent* boson operators  $b_0$  and  $b_1$  as done in Eq. (4.11). On the other hand, for the Haldane model on the honeycomb lattice, the condition (4.29) is not fulfilled for all momenta, as exemplified in Figs. C.1(a) and (b) for the Chern insulator at the nearly-flat band limit (3.18). Since  $F_{\alpha\alpha,\mathbf{q}}^2$  are real quantities, the imaginary parts of  $F_{01,\mathbf{q}}^2$  and  $F_{10,\mathbf{q}}^2$  are finite only in the vicinity of the  $M_1$  and  $M_2$  points, and  $|F_{01,\mathbf{q}}^2|, |F_{10,\mathbf{q}}^2| < |F_{\alpha\alpha,\mathbf{q}}^2|$ , we assume that, for the Haldane model, bosons operators  $b_0$  and  $b_1$  can still be defined by Eq. (4.11) and that they constitute two sets of independent boson operators.

A second important distinction between the Haldane and square lattice  $\pi$ -flux models is associated with the determination of the bosonic representation of operators written in terms of the fermion operators  $c_{\mathbf{q}\sigma}$ , such as the projected electron density operator  $\bar{\rho}_{a\sigma}(\mathbf{k})$  [Eq. (4.17)]. As discussed in Sec. III.B from Ref. [24], such a procedure is based on the fact that one can *define* the product of fermion operators  $c_{\mathbf{p}-\mathbf{q}\downarrow}^\dagger c_{\mathbf{p}\uparrow}$  in terms of the boson operators  $b_\alpha$ , i.e.,

$$c_{\mathbf{p}-\mathbf{q}\downarrow}^\dagger c_{\mathbf{p}\uparrow} \equiv \sum_{\beta} h_{\beta}(\mathbf{p}, \mathbf{q}) b_{\beta,\mathbf{q}}^\dagger. \quad (\text{B.4})$$

For the square lattice  $\pi$ -flux model, where the condition (4.29) holds, it is easy to see that the  $h_{\beta}(\mathbf{p}, \mathbf{q})$  function is given by

$$h_{\beta}(\mathbf{p}, \mathbf{q}) = \frac{1}{F_{\beta\beta,\mathbf{q}}} g_{\beta}^*(\mathbf{p}, \mathbf{q}), \quad (\text{B.5})$$

since the substitution of Eqs. (B.4) and (B.5) into (4.11) yields

$$\begin{aligned} b_{\alpha,\mathbf{q}}^\dagger &= \frac{1}{F_{\alpha\alpha,\mathbf{q}}} \sum_{\beta} \left[ \sum_{\mathbf{p}} h_{\beta}(\mathbf{p}, \mathbf{q}) g_{\alpha}(\mathbf{p}, \mathbf{q}) \right] b_{\beta,\mathbf{q}}^\dagger \\ &= \frac{1}{F_{\alpha\alpha,\mathbf{q}}} \sum_{\beta} \frac{\delta_{\alpha,\beta} F_{\alpha\beta,\mathbf{q}}^2}{F_{\beta\beta,\mathbf{q}}} b_{\beta,\mathbf{q}}^\dagger = b_{\alpha,\mathbf{q}}^\dagger, \end{aligned} \quad (\text{B.6})$$

see also Eq. (4.15). For the Haldane model on the honeycomb lattice, the choice (B.5) for the  $h_{\beta}(\mathbf{p}, \mathbf{q})$  function seems to be not appropriated, since the condition (4.29) is no longer valid. Due to the involved expansion of the  $g_{\alpha}(\mathbf{p}, \mathbf{q})$  function in terms of the coefficients (3.10) (not shown here), it is difficult to determine an  $h_{\beta}(\mathbf{p}, \mathbf{q})$  function such that the identity (B.6) is satisfied. Therefore, based on the same assumptions considered in the definition of the boson operators  $b_{\alpha}$  and discussed in the previous paragraph, we also assume that Eq. (B.5) [and consequently Eq. (4.17)] holds for the Haldane model.

As discussed in Sec. 4.2.2, one important consequence of the fact that the condition (4.29) is not fulfilled for the Haldane model is that the coefficients  $\bar{\omega}_{\mathbf{q}}^{01}$  and  $\bar{\omega}_{\mathbf{q}}^{10}$  [Eq. (4.21)] are finite and the coefficients (4.25) obey the relation  $\epsilon_{\mathbf{q}}^{01} = -\epsilon_{\mathbf{q}}^{10}$ , yielding a non-Hermitian quadratic boson Hamiltonian (4.23). It is indeed easy to understand the relation between these results once we compare the integrand of Eq. (4.15) with the ones of Eqs. (4.21), (B.24), and (B.23): Notice that all of them depend on the product  $g_{\alpha}(x, y)g_{\beta}^*(x', y')$ ; for  $\alpha \neq \beta$ , additional terms might be included in the  $\mathcal{G}_{\alpha\beta a\sigma}(\mathbf{k}, \mathbf{q})$  function, yielding  $\epsilon_{\mathbf{q}}^{01} = -\epsilon_{\mathbf{q}}^{10}$ . In principle, the condition  $\epsilon_{\mathbf{q}}^{01} = (\epsilon_{\mathbf{q}}^{10})^*$  could be restored, once an appropriated choice for the  $h_{\beta}(\mathbf{p}, \mathbf{q})$  function were done such that the identity (B.6) is now verified.

## B.2 The bosonic representation of the fermionic operators

Here we will comment on how fermionic operators can be mapped into bosonic operators using the bosonization scheme [24, 25]. The first thing that should be noticed is that the ferromagnetic ground state (3.31) is the vacuum of the bosonic operators as stated in Eqs (4.13) and (5.8). It follows that the many body Hilbert space is generated by the application of the bosonic creation operator over the reference state, that is

$$|\{n_{\alpha,\mathbf{q}}\}\rangle = \prod_{\mathbf{q} \in \{n_{\alpha,\mathbf{q}}\}} \frac{(b_{\alpha,\mathbf{q}}^\dagger)^{n_{\alpha,\mathbf{q}}}}{\sqrt{n_{\alpha,\mathbf{q}}!}} |0\rangle = \prod_{\mathbf{q}} \frac{(b_{\alpha,\mathbf{q}}^\dagger)^{n_{\alpha,\mathbf{q}}}}{\sqrt{n_{\alpha,\mathbf{q}}!}} |FM\rangle, \quad (\text{B.7})$$

where  $|\{n_{\alpha,\mathbf{q}}\}\rangle$  is the many body state. Now, we can obtain the bosonic representation of any operator  $\mathcal{O} = \mathcal{O}(c_{\mathbf{k}\sigma}^\dagger, c_{\mathbf{k}\sigma})$  by looking at its action on the many body state, i.e.,

$$\begin{aligned} \mathcal{O}|\{n_{\alpha,\mathbf{q}}\}\rangle &= \mathcal{O} \prod_{\mathbf{q}} \frac{(b_{\alpha,\mathbf{q}}^\dagger)^{n_{\alpha,\mathbf{q}}}}{\sqrt{n_{\alpha,\mathbf{q}}!}} |FM\rangle \\ &= \left[ \mathcal{O}, \prod_{\mathbf{q}} \frac{(b_{\alpha,\mathbf{q}}^\dagger)^{n_{\alpha,\mathbf{q}}}}{\sqrt{n_{\alpha,\mathbf{q}}!}} \right] |FM\rangle + \prod_{\mathbf{q}} \frac{(b_{\alpha,\mathbf{q}}^\dagger)^{n_{\alpha,\mathbf{q}}}}{\sqrt{n_{\alpha,\mathbf{q}}!}} \mathcal{O} |FM\rangle. \end{aligned} \quad (\text{B.8})$$

Therefore, the mapping from the fermionic to the bosonic representations reduces to the calculation of the action of the operator  $\mathcal{O}$  upon the ferromagnetic state and its commutator with  $(b_{\alpha,\mathbf{q}}^\dagger)^{n_{\alpha,\mathbf{q}}}$ .

To exemplify the use of (B.8), we will calculate the bosonic representation of some operators used for the **Chern insulator** in Sec. 4.2. First, we begin the calculation of the bosonic representation of the projected noninteracting Hamiltonian (4.19). Its action upon the ferromagnetic state is

$$\bar{H}_0 |FM\rangle = \sum_{\mathbf{q}\sigma} \omega_{c,\mathbf{q}} c_{\mathbf{q}\sigma}^\dagger c_{\mathbf{q}\sigma} |FM\rangle = \sum_{\mathbf{q}} \omega_{c,\mathbf{q}} |FM\rangle = E_0 |FM\rangle, \quad (\text{B.9})$$

where  $E_0$  is a constant value that can be calculated from  $\sum_{\mathbf{q}} \omega_{c,\mathbf{q}} \rightarrow \frac{N}{(2\pi)^2} \int_{BZ} \omega_{c,\mathbf{q}} d^2q$  and is found to be  $E_0 = (-1.69t_1)N$  for the nearly flat-band limit. For the commutator, we need a little bit more algebra, but we can start from the commutator  $[\bar{H}_0, b_{\alpha,\mathbf{q}}^\dagger]$ , which can be easily calculated using all operators in fermionic representation [see (4.11)], i.e.,

$$[\bar{H}_0, b_{\alpha,\mathbf{q}}^\dagger] = \sum_{\mathbf{p}} (\omega_{c,\mathbf{p}-\mathbf{q}} - \omega_{c,\mathbf{p}}) \frac{g_\alpha(\mathbf{p}, \mathbf{q})}{F_{\alpha\alpha,\mathbf{q}}} c_{\mathbf{p}-\mathbf{q}\downarrow} c_{\mathbf{p}\uparrow} \quad (\text{B.10})$$

$$= \sum_{\beta} \sum_{\mathbf{p}} (\omega_{c,\mathbf{p}-\mathbf{q}} - \omega_{c,\mathbf{p}}) \frac{g_\alpha(\mathbf{p}, \mathbf{q})}{F_{\alpha\alpha,\mathbf{q}} F_{\beta\beta,\mathbf{q}}} g_\beta(\mathbf{p} - \mathbf{q}, -\mathbf{q}) b_{\beta,\mathbf{q}}^\dagger, \quad (\text{B.11})$$

where in the last term we have identified that everything could be rewritten back in terms of the bosonic operators using Eq. (4.11). Now, looking at the structure of (B.11), we can infer that the bosonic version of  $\bar{H}_0$  should be composed of two bosonic operators. For instance, compare (B.11) to the following comutator

$$[b_{\beta,\mathbf{q}}^\dagger b_{\alpha,\mathbf{q}}, b_{\lambda,\mathbf{p}'}^\dagger] = b_{\beta,\mathbf{q}}^\dagger \delta_{\mathbf{q},\mathbf{p}'} \delta_{\alpha,\lambda}. \quad (\text{B.12})$$

Therefore, we find that

$$\bar{H}_0 = \sum_{\mathbf{p}\mathbf{q}\alpha\beta} (\omega_{c,\mathbf{p}-\mathbf{q}} - \omega_{c,\mathbf{p}}) \frac{g_\alpha(\mathbf{p}, \mathbf{q})}{F_{\alpha\alpha,\mathbf{q}} F_{\beta\beta,\mathbf{q}}} g_\beta(\mathbf{p} - \mathbf{q}, -\mathbf{q}) b_{\beta,\mathbf{q}}^\dagger b_{\alpha,\mathbf{q}} + \text{const.} \quad (\text{B.13})$$

To conclude, the general commutator (B.8) reads

$$\begin{aligned}
[\bar{H}_0, (b_{\alpha, \mathbf{q}}^\dagger)^{n_{\alpha, \mathbf{q}}}] &= \sum_{\mathbf{p}\mathbf{q}\alpha\beta} (\omega_{c, \mathbf{p}-\mathbf{q}} - \omega_{c, \mathbf{p}}) \frac{g_\alpha(\mathbf{p}, \mathbf{q})}{F_{\alpha\alpha, \mathbf{q}} F_{\beta\beta, \mathbf{q}}} g_\beta(\mathbf{p} - \mathbf{q}, -\mathbf{q}) [b_{\beta, \mathbf{q}}^\dagger b_{\alpha, \mathbf{q}} (b_{\alpha, \mathbf{q}}^\dagger)^{n_{\alpha, \mathbf{q}}}] \\
&= \sum_{\mathbf{p}\mathbf{q}\alpha\beta} (\omega_{c, \mathbf{p}-\mathbf{q}} - \omega_{c, \mathbf{p}}) \frac{g_\alpha(\mathbf{p}, \mathbf{q})}{F_{\alpha\alpha, \mathbf{q}} F_{\beta\beta, \mathbf{q}}} g_\beta(\mathbf{p} - \mathbf{q}, -\mathbf{q}) \left\{ b_{\beta, \mathbf{q}}^\dagger b_{\alpha, \mathbf{q}} (b_{\alpha, \mathbf{q}}^\dagger)^{n_{\alpha, \mathbf{q}}} - b_{\beta, \mathbf{q}}^\dagger (b_{\alpha, \mathbf{q}}^\dagger)^{n_{\alpha, \mathbf{q}}} b_{\alpha, \mathbf{q}} \right\}.
\end{aligned} \tag{B.14}$$

Thus, using (B.9) and (B.14), we compose

$$\begin{aligned}
\bar{H}_0 | \{n_{\alpha, \mathbf{q}}\} \rangle &= \left( \sum_{\mathbf{p}\mathbf{q}\alpha\beta} (\omega_{c, \mathbf{p}-\mathbf{q}} - \omega_{c, \mathbf{p}}) \frac{g_\alpha(\mathbf{p}, \mathbf{q})}{F_{\alpha\alpha, \mathbf{q}} F_{\beta\beta, \mathbf{q}}} g_\beta(\mathbf{p} - \mathbf{q}, -\mathbf{q}) b_{\beta, \mathbf{q}}^\dagger b_{\alpha, \mathbf{q}} + E_0 \right) \\
&\quad \times \prod_{\mathbf{q}} \frac{(b_{\alpha, \mathbf{q}}^\dagger)^{n_{\alpha, \mathbf{q}}}}{\sqrt{n_{\alpha, \mathbf{q}}!}} |FM\rangle,
\end{aligned} \tag{B.15}$$

which enables us to read the bosonic representation of  $\bar{H}_0$  as the term in parenthesis. For convenience, we can write it in a compact form,

$$\bar{H}_0 = E_0 + \sum_{\mathbf{q}\alpha\beta} \bar{\omega}_{\alpha\beta, \mathbf{q}} b_{\beta, \mathbf{q}}^\dagger b_{\alpha, \mathbf{q}}, \tag{B.16}$$

where

$$\bar{\omega}_{\alpha\beta, \mathbf{q}} = \frac{1}{F_{\alpha\alpha, \mathbf{q}} F_{\beta\beta, \mathbf{q}}} \sum_{\mathbf{p}} (\omega_{c, \mathbf{p}-\mathbf{q}} - \omega_{c, \mathbf{p}}) g_\alpha(\mathbf{p}, \mathbf{q}) g_\beta(\mathbf{p} - \mathbf{q}, -\mathbf{q}). \tag{B.17}$$

The same procedure is also used to find the bosonic representation of the projected Hubbard term  $\bar{H}_U$  (4.9) (**Chern insulator**). Here we will give just the main steps, starting from the projected density operator (4.7)

$$[\bar{\rho}_{a\uparrow}(\mathbf{k}), b_{\alpha, \mathbf{q}}^\dagger] = -\frac{1}{F_{\alpha\alpha, \mathbf{q}}} \sum_{\mathbf{p}} G_a(\mathbf{p}, \mathbf{k}) g_\alpha(\mathbf{p} - \mathbf{k}, \mathbf{q}) c_{\mathbf{p}-\mathbf{q}-\mathbf{k}\downarrow}^\dagger c_{\mathbf{p}\uparrow}. \tag{B.18}$$

Differently from Eq. (B.11), there is no direct expression to translate the result (B.18) to a bosonic form. Nevertheless, we can use the approximations discussed in Sec. B.1, i.e., the definitions (B.4) and (B.5). Therefore, the commutator (B.18) becomes

$$[\bar{\rho}_{a\uparrow}(\mathbf{k}), b_{\alpha, \mathbf{q}}^\dagger] = -\frac{1}{F_{\alpha\alpha, \mathbf{q}}} \sum_{\mathbf{p}} G_a(\mathbf{p}, \mathbf{k}) g_\alpha(\mathbf{p} - \mathbf{k}, \mathbf{q}) \left( \sum_{\beta} \frac{1}{F_{\beta\beta, \mathbf{q}+\mathbf{k}}} g_\beta(\mathbf{p} - \mathbf{q} - \mathbf{k}, -\mathbf{q} - \mathbf{k}) b_{\beta, \mathbf{q}+\mathbf{k}}^\dagger \right), \tag{B.19}$$

where, again, due to the structure of (B.19), we can infer the form of the bosonic representation of the projected electron density operator,

$$\bar{\rho}_{a\uparrow}(\mathbf{k}) = - \sum_{\mathbf{p}\mathbf{q}\alpha\beta} \frac{G_a(\mathbf{p}, \mathbf{k})}{F_{\alpha\alpha, \mathbf{q}} F_{\beta\beta, \mathbf{q}+\mathbf{k}}} g_\alpha(\mathbf{p} - \mathbf{k}, \mathbf{q}) g_\beta(\mathbf{p} - \mathbf{q} - \mathbf{k}, -\mathbf{q} - \mathbf{k}) b_{\beta, \mathbf{q}+\mathbf{k}}^\dagger b_{\alpha, \mathbf{q}} + \text{const.} \tag{B.20}$$

The commutator needed in (B.8) can be straightforwardly calculated in the same way it was done in (B.14), and the constant in (B.20) is just the action of the operator  $\bar{\rho}_{a\uparrow}(\mathbf{k})$  in the ferromagnetic ground state, that is,

$$\begin{aligned}\bar{\rho}_{a\uparrow}(\mathbf{k})|FM\rangle &= \sum_{\mathbf{p}} G_a(\mathbf{p}, \mathbf{k}) c_{\mathbf{p}-\mathbf{k}\uparrow}^\dagger c_{\mathbf{p}\uparrow} |FM\rangle = \sum_{\mathbf{p}} G_a(\mathbf{p}, \mathbf{k}) \delta_{\sigma,\uparrow} \delta_{\mathbf{q},0} |FM\rangle \\ &= \frac{N}{2} \delta_{\sigma,\uparrow} \delta_{\mathbf{q},0} |FM\rangle,\end{aligned}\quad (\text{B.21})$$

where the sum can be easily determined with the aid of Eqs. (4.8) and (3.12). Gathering all together, furnishes the final expression

$$\bar{\rho}_{a\uparrow}(\mathbf{k}) = \frac{N}{2} \delta_{\sigma,\uparrow} \delta_{\mathbf{k},0} + \sum_{\mathbf{q}\alpha\beta} \mathcal{G}_{\alpha\beta a\sigma}(\mathbf{k}, \mathbf{q}) b_{\beta, \mathbf{k}+\mathbf{q}}^\dagger b_{\alpha, \mathbf{q}}, \quad (\text{B.22})$$

where  $\mathcal{G}_{\alpha\beta a\sigma}(\mathbf{k}, \mathbf{q})$  function used in the Chern insulator calculations is given by

$$\mathcal{G}_{\alpha\beta a\uparrow}(\mathbf{k}, \mathbf{q}) = \frac{-1}{F_{\alpha\alpha, \mathbf{q}} F_{\beta\beta, \mathbf{q}+\mathbf{k}}} \sum_{\mathbf{p}} G_a(\mathbf{p}, \mathbf{k}) g_\alpha(\mathbf{p} - \mathbf{k}, \mathbf{q}) g_\beta(\mathbf{p} - \mathbf{q} - \mathbf{k}, -\mathbf{q} - \mathbf{k}), \quad (\text{B.23})$$

$$\mathcal{G}_{\alpha\beta a\downarrow}(\mathbf{k}, \mathbf{q}) = \frac{1}{F_{\alpha\alpha, \mathbf{q}} F_{\beta\beta, \mathbf{q}+\mathbf{k}}} \sum_{\mathbf{p}} G_a(\mathbf{p} - \mathbf{q}, \mathbf{k}) g_\alpha(\mathbf{p}, \mathbf{q}) g_\beta(\mathbf{p} - \mathbf{q} - \mathbf{k}, -\mathbf{q} - \mathbf{k}). \quad (\text{B.24})$$

# Appendix C

## Details of the bosonization scheme: Chern insulator

### C.1 Function definitions : $F_{\alpha\beta,\mathbf{q}}$ and $\mathcal{G}_{\alpha\beta a\sigma}(\mathbf{k}, \mathbf{q})$

In this Appendix, which is based on the Appendix A from Ref. [34], we quote the expansions of the  $F_{\alpha\beta,\mathbf{q}}$  and  $\mathcal{G}_{\alpha\beta a\sigma}(\mathbf{k}, \mathbf{q})$  functions in terms of the coefficients (3.10). As discussed in Appendix B, the  $F_{\alpha\beta,\mathbf{q}}$  function originates from the commutator (B.3) between the operators  $\bar{S}_{\mathbf{q},\alpha}^+$  and  $\bar{S}_{\mathbf{q},\beta}^-$ , while  $\mathcal{G}_{\alpha\beta a\sigma}(\mathbf{k}, \mathbf{q})$  comes from the determination of the bosonic representation of the projected density operator  $\bar{\rho}_{a\sigma}(\mathbf{k})$ , see Eq.(B.22). For the Chern insulator, both functions are fundamental for the calculation of the spin-wave spectrum through the effective bosonic Hamiltonian (4.27) [see also Eqs. (4.23) and (4.25)].

The  $F_{\alpha\beta,\mathbf{q}}$  function (4.15) is defined in terms of the appropriated  $g_\alpha(\mathbf{p}, \mathbf{q})$  function (4.16), which is written in terms of the coefficients  $u_{\mathbf{k}}$  and  $v_{\mathbf{k}}$  of the canonical transformation (3.11). Therefore, substituting (4.16) in (4.15) and using (3.11), one shows that

$$\begin{aligned}
 F_{\alpha\beta,\mathbf{q}}^2 = & \frac{1}{4} \sum_{\mathbf{p}} [1 + (-1)^{\alpha+\beta}] \left( 1 + \hat{B}_{3,\mathbf{p}} \hat{B}_{3,\mathbf{p}-\mathbf{q}} \right) \\
 & - [1 - (-1)^{\alpha+\beta}] \left( \hat{B}_{3,\mathbf{p}} + \hat{B}_{3,\mathbf{p}-\mathbf{p}} \right) \\
 & + [(-1)^\alpha + (-1)^\beta] \left( \hat{B}_{1,\mathbf{p}} \hat{B}_{1,\mathbf{p}-\mathbf{q}} + \hat{B}_{2,\mathbf{p}} \hat{B}_{2,\mathbf{p}-\mathbf{q}} \right) \\
 & + i [(-1)^\alpha - (-1)^\beta] \left( \hat{B}_{1,\mathbf{p}} \hat{B}_{2,\mathbf{p}-\mathbf{q}} - \hat{B}_{2,\mathbf{p}} \hat{B}_{1,\mathbf{p}-\mathbf{q}} \right), \quad (\text{C.1})
 \end{aligned}$$

with  $\alpha, \beta = 0, 1$  and  $\hat{B}_{i,\mathbf{k}} = B_{i,\mathbf{k}}/|\mathbf{B}_{\mathbf{k}}|$ . Figure C.1 shows the function (C.1) along paths in first Brillouin zone for the nearly flat band limit. In Fig. C.1(a), we can see that  $F_{\alpha\beta,\mathbf{q}}^2$  is purely real for  $\alpha = \beta$  while it has some finite imaginary contributions for  $\alpha \neq \beta$ , as shown in Fig. C.1(b). Figure C.1(c) shows how the real part of  $F_{01,\mathbf{q}}^2$  is affected when a mass term (3.19) is nonzero.

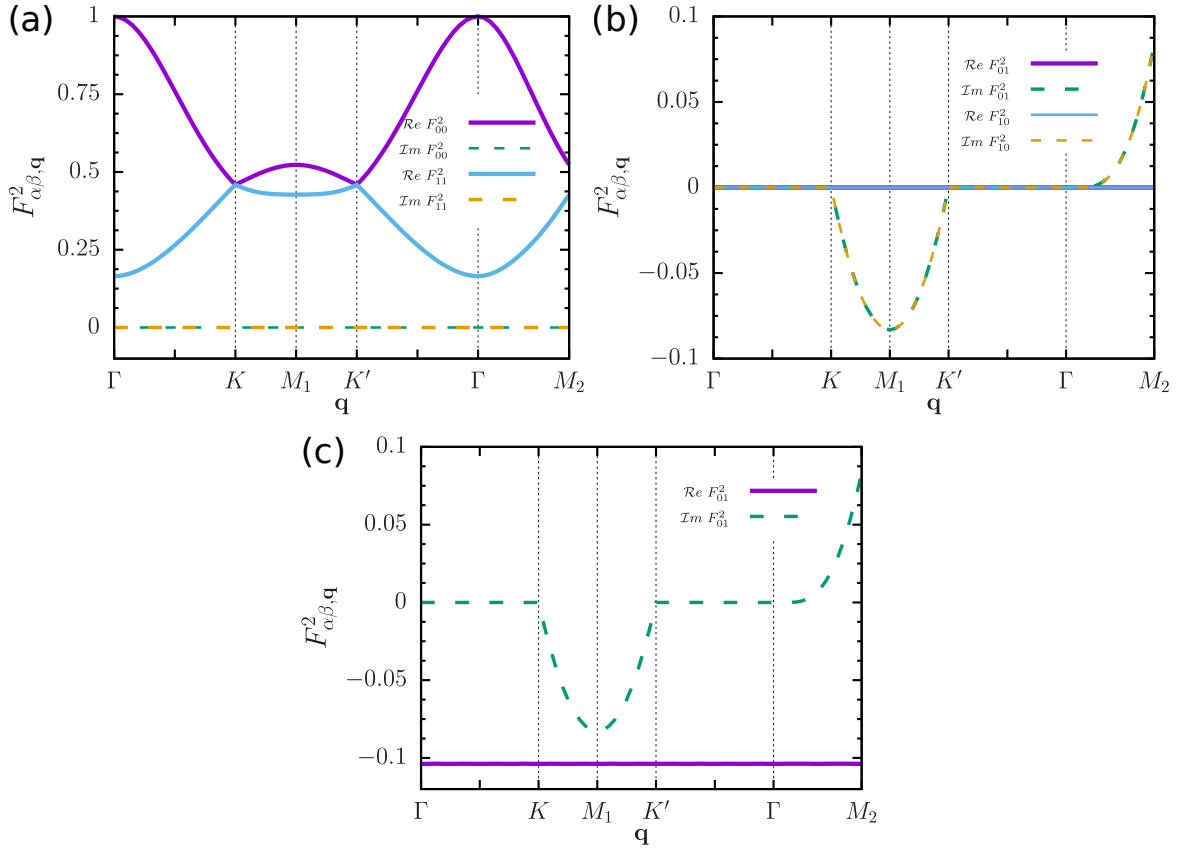


**Figure C.1:** The real (solid line) and imaginary (dashed line) parts of the  $F_{\alpha\beta, \mathbf{q}}^2$  function [Eq. (4.15)] for the Haldane-Hubbard model (4.1) in the nearly-flat band limit (3.18): (a)  $F_{00, \mathbf{q}}^2$  and  $F_{11, \mathbf{q}}^2$  (b)  $F_{01, \mathbf{q}}^2$  and  $F_{10, \mathbf{q}}^2$  for staggered on-site energy  $M = 0$ ; (c)  $F_{01, \mathbf{q}}^2$  for staggered on-site energy  $M = 0.2 t_1$ .

The  $\mathcal{G}_{\alpha\beta a\sigma}(\mathbf{k}, \mathbf{q})$  function, which determines the bosonic expression (4.17) of the projected density operator  $\bar{\rho}_{a\sigma}(\mathbf{k})$ , have different representations for spin- $\uparrow$  and spin- $\downarrow$  as defined in Eqs. (B.23) and (B.24), respectively. Using the  $u_{\mathbf{k}}$  and  $v_{\mathbf{k}}$  coefficients of the canonical transformation (3.11) and the relations (3.12) into Eqs. (B.23) and (B.24), it is possible to express the  $\mathcal{G}_{\alpha\beta a\sigma}(\mathbf{k}, \mathbf{q})$  function entirely in terms of the  $\hat{B}_{i, \mathbf{k}} = B_{i, \mathbf{k}}/|\mathbf{B}_{\mathbf{k}}|$ , i.e.,

$$\begin{aligned}
\mathcal{G}_{\alpha\beta a\sigma}(\mathbf{k}, \mathbf{q}) &= -\gamma_{\sigma} \frac{1}{8} [\delta_{a,A} + \delta_{a,B} (-1)^{\alpha+\beta}] \frac{1}{F_{\alpha\alpha, \mathbf{q}} F_{\beta\beta, \mathbf{k}+\mathbf{q}}} \\
&\times \sum_{\mathbf{p}} [1 + \hat{B}_3(1)\hat{B}_3(2) + \hat{B}_3(1)\hat{B}_3(3) + \hat{B}_3(2)\hat{B}_3(3) \\
&- (-1)^a (\hat{B}_3(1) + \hat{B}_3(2) + \hat{B}_3(3) + \hat{B}_3(1)\hat{B}_3(2)\hat{B}_3(3))] \\
&+ \zeta_1(\sigma) [\hat{B}_1(2)\hat{B}_1(3) + \hat{B}_2(2)\hat{B}_2(3) + i(-1)^a (\hat{B}_2(2)\hat{B}_1(3) - \hat{B}_1(2)\hat{B}_2(3))] [1 + \gamma_{\sigma} (-1)^a \hat{B}_3(1)] \\
&+ \zeta_2(\sigma) [\hat{B}_1(1)\hat{B}_1(3) + \hat{B}_2(1)\hat{B}_2(3) + i(-1)^a (\hat{B}_2(1)\hat{B}_1(3) - \hat{B}_1(1)\hat{B}_2(3))] [1 - \gamma_{\sigma} (-1)^a \hat{B}_3(2)] \\
&+ \zeta_3(\sigma) [\hat{B}_1(1)\hat{B}_1(2) + \hat{B}_2(1)\hat{B}_2(2) + i\gamma_{\sigma} (-1)^a (\hat{B}_1(1)\hat{B}_2(2) - \hat{B}_2(1)\hat{B}_1(2))] [1 - (-1)^a \hat{B}_3(3)],
\end{aligned} \tag{C.2}$$

where the coefficient  $\gamma_\uparrow = -\gamma_\downarrow = 1$ , the coefficients  $\zeta_i(\sigma)$  read

$$\begin{aligned}\zeta_1(\uparrow) &= (-1)^{\alpha+\beta}, & \zeta_2(\uparrow) &= (-1)^\beta, & \zeta_3(\uparrow) &= (-1)^\alpha, \\ \zeta_1(\downarrow) &= (-1)^\alpha, & \zeta_2(\downarrow) &= (-1)^{\alpha+\beta}, & \zeta_3(\downarrow) &= (-1)^\beta,\end{aligned}\tag{C.3}$$

and the  $\hat{B}_i(j)$  functions, with  $i, j = 1, 2, 3$ , are given by

$$\hat{B}_i(1) = \hat{B}_{i, \mathbf{p}-\mathbf{k}-\mathbf{q}}, \quad \hat{B}_i(2) = \hat{B}_{i, \mathbf{p}-\mathbf{k}}, \quad \hat{B}_i(3) = \hat{B}_{i, \mathbf{p}},\tag{C.4}$$

for  $\sigma = \uparrow$ , and

$$\hat{B}_i(1) = \hat{B}_{i, \mathbf{p}}, \quad \hat{B}_i(2) = \hat{B}_{i, \mathbf{p}+\mathbf{k}+\mathbf{q}}, \quad \hat{B}_i(3) = \hat{B}_{i, \mathbf{p}+\mathbf{k}},\tag{C.5}$$

for  $\sigma = \downarrow$ .

# Appendix D

## Details of the bosonization scheme: $Z_2$ topological insulator

Here we present the extended form of the functions  $F_{\alpha\beta,\mathbf{q}}^2$  and  $\mathcal{G}_{\alpha\beta a\uparrow}(\mathbf{k}, \mathbf{q})$  in terms of the coefficients  $B_{i,\mathbf{k}}$  defined in Eq. (3.25). This Appendix is based on the Appendices A and B from Ref. [35].

### D.1 Function definitions for the ML excitations

First, we recall the expression (5.7) of the  $g_\alpha(\mathbf{p}, \mathbf{q})$  function, that follows from the definition of the boson operators (5.3) of the ML excitations (5.4), that is,

$$g_\alpha(\mathbf{k}, \mathbf{q}) = -u_{\mathbf{k}}v_{-\mathbf{k}+\mathbf{q}} - (-1)^\alpha u_{-\mathbf{k}+\mathbf{q}}v_{\mathbf{k}}.$$

By the use of Eq. (5.7) with the aid of the coefficients  $u_{\mathbf{k}}$  and  $v_{\mathbf{k}}$  of the canonical transformation (3.26) and the relations (3.27), it is possible to express the function  $F_{\alpha\beta,\mathbf{q}}^2$  [Eq. (5.6)] in terms of the model coefficients (3.25) for spin  $\sigma = \uparrow$ , i.e.,

$$\begin{aligned} F_{\alpha\beta,\mathbf{q}}^2 = & \frac{1}{4} \sum_{\mathbf{p}} [(-1)^\alpha + (-1)^\beta] \left( 1 - \hat{B}_{3,\mathbf{p}}\hat{B}_{3,-\mathbf{p}+\mathbf{q}} \right) \\ & - [(-1)^\alpha - (-1)^\beta] \left( \hat{B}_{3,\mathbf{p}} - \hat{B}_{3,-\mathbf{p}+\mathbf{p}} \right) \\ & + [1 + (-1)^{\alpha+\beta}] \left( \hat{B}_{1,\mathbf{p}}\hat{B}_{1,-\mathbf{p}+\mathbf{q}} + \hat{B}_{2,\mathbf{p}}\hat{B}_{2,-\mathbf{p}+\mathbf{q}} \right) \\ & - i [1 - (-1)^{\alpha+\beta}] \left( \hat{B}_{1,\mathbf{p}}\hat{B}_{2,-\mathbf{p}+\mathbf{q}} - \hat{B}_{2,\mathbf{p}}\hat{B}_{1,-\mathbf{p}+\mathbf{q}} \right), \end{aligned} \quad (\text{D.1})$$

where  $\hat{B}_{i,\mathbf{k}} = B_{i,\mathbf{k}}/|\mathbf{B}_{\mathbf{k}}|$ . A plot of the function (D.1) for the nearly flat band limit (3.18) can be seen in Fig. D.1, where we can see that it is purely real when  $\alpha = \beta$  while a small purely imaginary contribution appears for  $\alpha \neq \beta$ . The imaginary contribution shows us that, analogously to the description of the correlated Chern insulator on the honeycomb

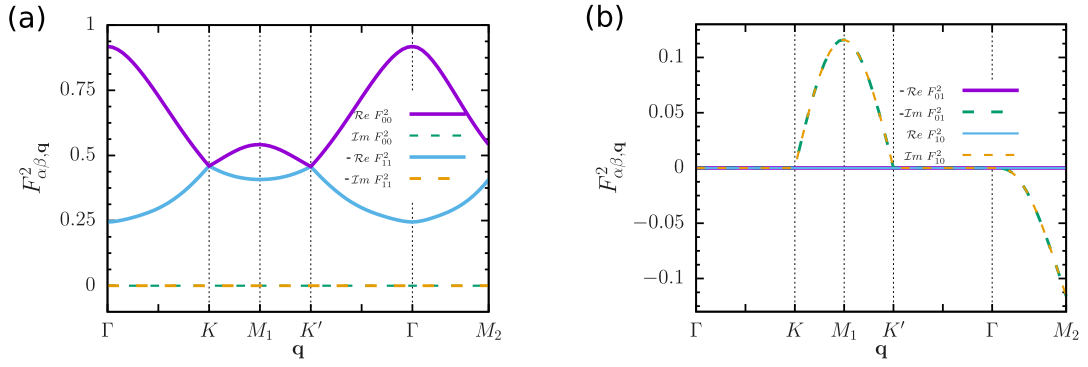


**Figure D.1:** The real (solid line) and imaginary (dashed line) parts of the  $F_{\alpha\beta,\mathbf{q}}^2$  function [Eq. (5.6), ML excitations] for the Haldane model (3.1) in the nearly-flat band limit (3.18) along paths in the first Brillouin zone: (a)  $F_{00,\mathbf{q}}^2$  and  $F_{11,\mathbf{q}}^2$  and (b)  $F_{01,\mathbf{q}}^2$  and  $F_{10,\mathbf{q}}^2$ .

lattice (see discussion in Appendix C), the condition (4.29) is not completely fulfilled for the ML excitations of the correlated  $Z_2$  topological insulator.

Finally, the  $\mathcal{G}_{\alpha\beta a\uparrow}(\mathbf{k}, \mathbf{q})$  function is an essential quantity used in the calculation of spin-wave spectrum (5.16), more specifically, it appear in Eq. (4.25), and has the following expression [the analogous of Eq. (B.23) and (B.24) for the Chern insulator]

$$\begin{aligned}\mathcal{G}_{\alpha\beta a\uparrow}(\mathbf{k}, \mathbf{q}) &= - \sum_{\mathbf{p}} \frac{G_{a\uparrow}(\mathbf{p}, \mathbf{k})}{F_{\alpha\alpha,\mathbf{q}} F_{\beta\beta,\mathbf{k}+\mathbf{q}}} g_{\alpha}(\mathbf{p} - \mathbf{k}, \mathbf{q}) g_{\beta}^*(-\mathbf{p} + \mathbf{k} + \mathbf{q}, \mathbf{k} + \mathbf{q}), \\ \mathcal{G}_{\alpha\beta a\downarrow}(\mathbf{k}, \mathbf{q}) &= + \sum_{\mathbf{p}} \frac{G_{a\downarrow}(\mathbf{p} - \mathbf{q}, \mathbf{k})}{F_{\alpha\alpha,\mathbf{q}} F_{\beta\beta,\mathbf{k}+\mathbf{q}}} g_{\alpha}(\mathbf{p}, \mathbf{q}) g_{\beta}^*(-\mathbf{p} + \mathbf{k} + \mathbf{q}, \mathbf{k} + \mathbf{q}),\end{aligned}\tag{D.2}$$

where the  $G_{a\sigma}(\mathbf{p}, \mathbf{q})$  function is given by Eq. (5.2). Again, with the aid of Eq. (3.27), which provides the expressions of the coefficients  $u_{\mathbf{k}}$  and  $v_{\mathbf{k}}$  of the canonical transformation (3.26) in terms of the coefficients (3.25) for  $\sigma = \uparrow$ , one finds that

$$\begin{aligned}\mathcal{G}_{\alpha\beta a\sigma}(\mathbf{k}, \mathbf{q}) &= -\gamma_{\sigma} \frac{1}{8} [\delta_{a,A} + \delta_{a,B} (-1)^{\alpha+\beta}] \frac{1}{F_{\alpha\alpha,\mathbf{q}} F_{\beta\beta,\mathbf{k}+\mathbf{q}}} \\ &\times \sum_{\mathbf{p}} \zeta_1(\sigma) \left[ 1 + \gamma_{\sigma} (-1)^a \hat{B}_3(1) \right] \left[ 1 - \gamma_{\sigma} (-1)^a \hat{B}_3(2) \right] \left[ 1 - (-1)^a \hat{B}_3(3) \right] \\ &+ \zeta_2(\sigma) \left[ \hat{B}_1(2) \hat{B}_1(3) + \hat{B}_2(2) \hat{B}_2(3) + i(-1)^a \left( \hat{B}_1(2) \hat{B}_2(3) - \hat{B}_2(2) \hat{B}_1(3) \right) \right] \left[ 1 - (-1)^a \hat{B}_3(1) \right] \\ &+ \zeta_3(\sigma) \left[ \hat{B}_1(1) \hat{B}_1(3) + \hat{B}_2(1) \hat{B}_2(3) + i(-1)^a \left( \hat{B}_1(1) \hat{B}_2(3) - \hat{B}_2(1) \hat{B}_1(3) \right) \right] \left[ 1 - (-1)^a \hat{B}_3(2) \right] \\ &+ \zeta_4(\sigma) \left[ \hat{B}_1(1) \hat{B}_1(2) + \hat{B}_2(1) \hat{B}_2(2) + i\gamma_{\sigma} (-1)^a \left( \hat{B}_2(1) \hat{B}_1(2) - \hat{B}_1(1) \hat{B}_2(2) \right) \right] \left[ 1 - (-1)^a \hat{B}_3(3) \right],\end{aligned}\tag{D.3}$$

where the coefficient  $\gamma_{\uparrow} = -\gamma_{\downarrow} = 1$ , the coefficients  $\zeta_i(\sigma)$  read

$$\begin{aligned}\zeta_1(\uparrow) &= (-1)^{\alpha}, & \zeta_2(\uparrow) &= (-1)^{\beta}, & \zeta_3(\uparrow) &= 1, & \zeta_4(\uparrow) &= (-1)^{\alpha+\beta}, \\ \zeta_1(\downarrow) &= (-1)^{\beta}, & \zeta_2(\downarrow) &= (-1)^{\alpha+\beta}, & \zeta_3(\downarrow) &= (-1)^{\alpha}, & \zeta_4(\downarrow) &= 1,\end{aligned}\tag{D.4}$$

and the  $\hat{B}_i(j)$  functions, with  $i, j = 1, 2, 3$ , are given by

$$\hat{B}_i(1) = \hat{B}_{i,-\mathbf{p}+\mathbf{k}+\mathbf{q}}, \quad \hat{B}_i(2) = \hat{B}_{i,\mathbf{p}}, \quad \hat{B}_i(3) = \hat{B}_{i,\mathbf{p}-\mathbf{k}}, \quad (\text{D.5})$$

for  $\sigma = \uparrow$ , and

$$\hat{B}_i(1) = \hat{B}_{i,-\mathbf{p}+\mathbf{k}+\mathbf{q}}, \quad \hat{B}_i(2) = \hat{B}_{i,\mathbf{p}}, \quad \hat{B}_i(3) = \hat{B}_{i,-\mathbf{p}+\mathbf{q}}, \quad (\text{D.6})$$

for  $\sigma = \downarrow$ . There is a useful property satisfied by Eq. (D.3), namely,

$$\mathcal{G}_{\alpha\beta a\uparrow}^*(\mathbf{k}, \mathbf{q}) = \mathcal{G}_{\beta\alpha a\uparrow}(-\mathbf{k}, \mathbf{k} + \mathbf{q}), \quad (\text{D.7})$$

which is necessary for the calculation of the coefficients (4.25).

Lastly, we want to explicitly show the values of the coefficients  $\bar{\omega}_{\mathbf{q}}^{\alpha\beta}$  [Eq. (4.21)] and  $\epsilon_{\mathbf{q}}^{\alpha\beta}$  [Eq. (4.25)]. The kinetic coefficients  $\bar{\omega}_{\mathbf{q}}^{\alpha\beta}$  are plotted in Fig. D.2(a) and (b), where we can see a finite but small contribution in units of  $t_1$ . Figure D.2(c) shows the off-diagonal elements of  $\epsilon_{\mathbf{q}}^{\alpha\beta}$ , showing the non-Hermitian behavior of the effective bosonic Hamiltonian (5.14).

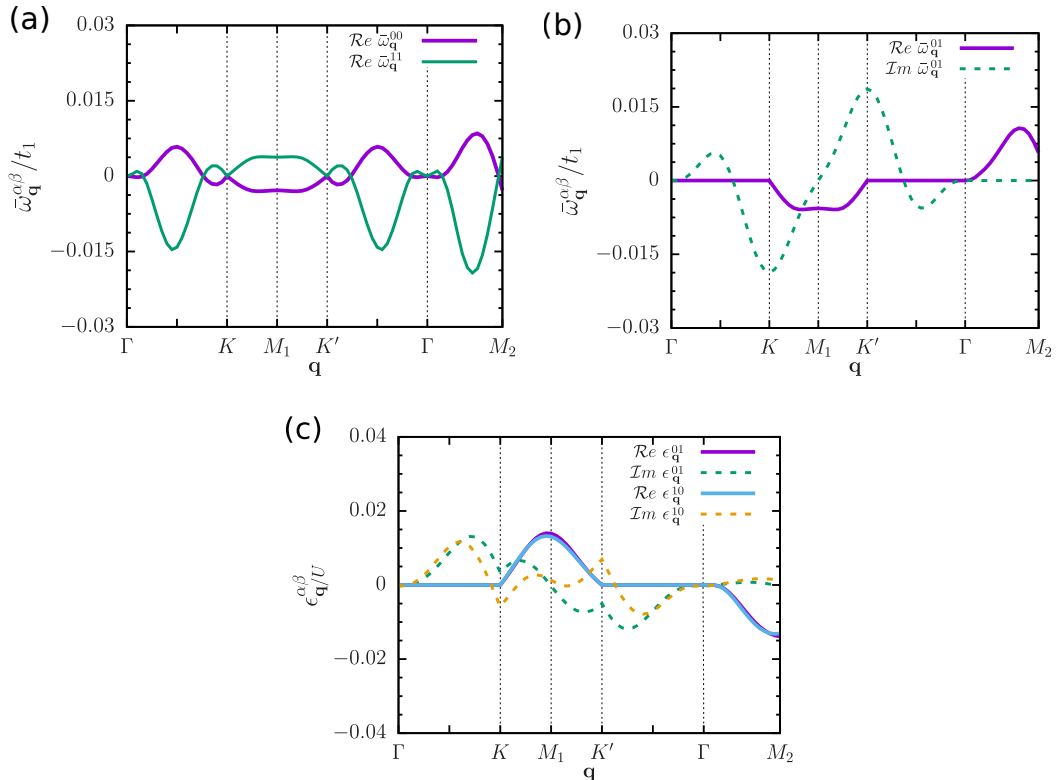


**Figure D.2:** The real (solid magenta line) and imaginary (dashed green line) parts of the kinetic coefficients (a)  $\bar{\omega}_{\mathbf{q}}^{00}$  and (b)  $\bar{\omega}_{\mathbf{q}}^{11}$  [Eq. (4.21), ML excitations] along paths in the first Brillouin zone for the Haldane model (3.1) in the nearly-flat band limit (3.18). (c) The real (solid line) and imaginary (dashed line) parts of the coefficients  $\epsilon_{\mathbf{q}}^{01}$  and  $\epsilon_{\mathbf{q}}^{10}$  [Eq. (4.25), ML excitations] for the topological Hubbard model in the nearly-flat band limit (3.18) and on-site repulsion energies  $U_A = U_B = U$ .

## D.2 Function definitions for the SL excitations

We start recalling that the  $g_\alpha(\mathbf{p}, \mathbf{q})$  function, defined in Eq. (5.7) for the ML excitations (5.4), is now given by Eq. (5.10) for the SL excitations (5.9). Although  $F_{\alpha\beta, \mathbf{q}}^2$  is given by Eq. (5.6) for both ML and SL excitations, its representation in terms of the  $B_{i, \mathbf{k}}$  coefficients (3.25) for the SL excitation is given by

$$\begin{aligned}
 F_{\alpha\beta, \mathbf{q}}^2 = & \frac{1}{4} \sum_{\mathbf{p}} [1 + (-1)^{\alpha+\beta}] \left( 1 + \hat{B}_{3, \mathbf{p}} \hat{B}_{3, -\mathbf{p}+\mathbf{q}} \right) \\
 & - [1 - (-1)^{\alpha+\beta}] \left( \hat{B}_{3, \mathbf{p}} + \hat{B}_{3, -\mathbf{p}+\mathbf{q}} \right) \\
 & + [(-1)^\alpha + (-1)^\beta] \left( \hat{B}_{1, \mathbf{p}} \hat{B}_{1, -\mathbf{p}+\mathbf{q}} - \hat{B}_{2, \mathbf{p}} \hat{B}_{2, -\mathbf{p}+\mathbf{q}} \right) \\
 & - i [(-1)^\alpha - (-1)^\beta] \left( \hat{B}_{1, \mathbf{p}} \hat{B}_{2, -\mathbf{p}+\mathbf{q}} + \hat{B}_{2, \mathbf{p}} \hat{B}_{1, -\mathbf{p}+\mathbf{q}} \right). \quad (\text{D.8})
 \end{aligned}$$

The corresponding plots for the function (D.8) at the nearly flat band limit can be seen in Figs. D.3(a) and (b), which shows that Eq. (D.8) is purely real for  $\alpha = \beta$  and has a small imaginary contribution for  $\alpha \neq \beta$ , again, violating condition (4.29). In Fig. D.3(c), we show the real (solid lines) and imaginary (dashed lines) parts of the coefficients  $\epsilon_{\mathbf{q}}^{\alpha\beta}$ , where we can see that, exclusively for the SL excitations,  $\epsilon_{\mathbf{q}}^{01}$  is the complex conjugate of  $\epsilon_{\mathbf{q}}^{10}$ .

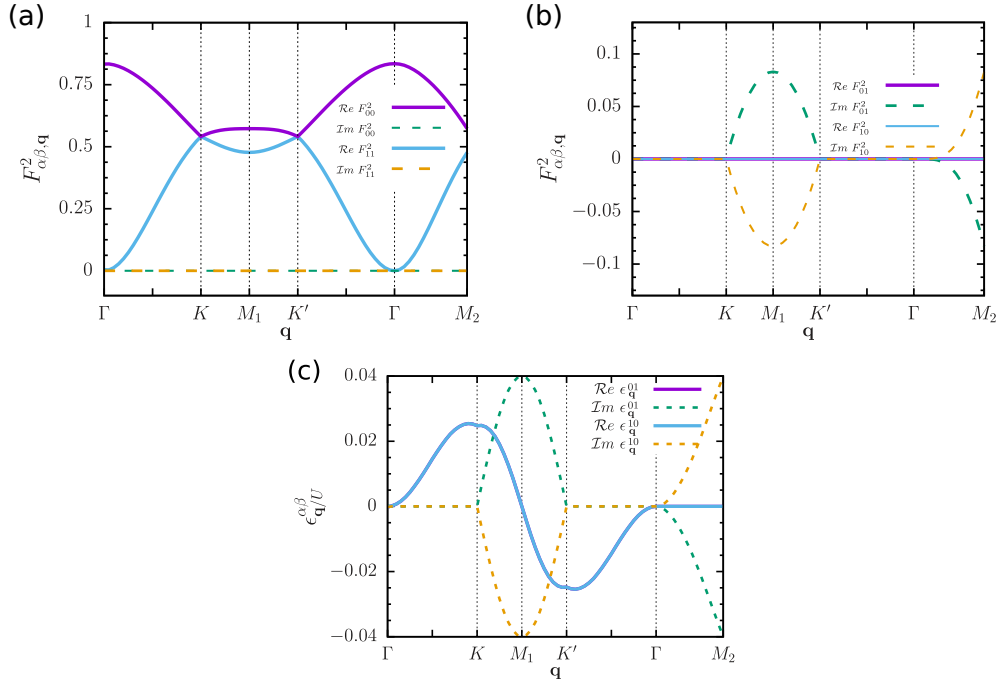


**Figure D.3:** SL excitations (5.9). The real (solid line) and imaginary (dashed line) parts of the  $F_{\alpha\beta, \mathbf{q}}^2$  function [Eq. (D.8)] for the Haldane model (3.1) in the nearly-flat band limit (3.18) along paths in the first Brillouin zone: (a)  $F_{00, \mathbf{q}}^2$  and  $F_{11, \mathbf{q}}^2$  and (b)  $F_{01, \mathbf{q}}^2$  and  $F_{10, \mathbf{q}}^2$ . (c) The real (solid line) and imaginary (dashed line) parts of the coefficients  $\epsilon_{\mathbf{q}}^{\alpha\beta}$  and  $\epsilon_{\mathbf{q}}^{\alpha\beta}$  [Eq. (4.25)] for the topological Hubbard model in the nearly-flat band limit (3.18) and on-site repulsion energies  $U_A = U_B = U$ .

Finally, the function  $\mathcal{G}_{\alpha\beta a\sigma}(\mathbf{k}, \mathbf{q})$ , which is given by the expression (D.2) for both SL and ML excitations, has the following representation in terms of the  $B_{i,\mathbf{k}}$  coefficients (3.25) for the SL excitation

$$\begin{aligned}
\mathcal{G}_{\alpha\beta a\sigma}(\mathbf{k}, \mathbf{q}) &= -\gamma_\sigma \frac{1}{8} [\delta_{a,A} + \delta_{a,B}(-1)^{\alpha+\beta}] \frac{1}{F_{\alpha\alpha,\mathbf{q}} F_{\beta\beta,\mathbf{k}+\mathbf{q}}} \\
&\times \sum_{\mathbf{p}} \left[ 1 - (-1)^a \hat{B}_3(1) \right] \left[ 1 - (-1)^a \hat{B}_3(2) \right] \left[ 1 - (-1)^a \hat{B}_3(3) \right] \\
&+ \zeta_1(\sigma) \left[ \hat{B}_1(2)\hat{B}_1(3) + \gamma_\sigma \hat{B}_2(2)\hat{B}_2(3) + i(-1)^a \left( \hat{B}_1(2)\hat{B}_2(3) - \gamma_\sigma \hat{B}_2(2)\hat{B}_1(3) \right) \right] \left[ 1 + \gamma_\sigma (-1)^a \hat{B}_3(1) \right] \\
&+ \zeta_2(\sigma) \left[ \hat{B}_1(1)\hat{B}_1(3) - \gamma_\sigma \hat{B}_2(1)\hat{B}_2(3) + i(-1)^a \left( \hat{B}_1(1)\hat{B}_2(3) + \gamma_\sigma \hat{B}_2(1)\hat{B}_1(3) \right) \right] \left[ 1 - \gamma_\sigma (-1)^a \hat{B}_3(2) \right] \\
&+ \zeta_3(\sigma) \left[ \hat{B}_1(1)\hat{B}_1(2) - \hat{B}_2(1)\hat{B}_2(2) - i(-1)^a \left( \hat{B}_1(1)\hat{B}_2(2) + \hat{B}_2(1)\hat{B}_1(2) \right) \right] \left[ 1 - (-1)^a \hat{B}_3(3) \right],
\end{aligned} \tag{D.9}$$

where the coefficient  $\gamma_\uparrow = -\gamma_\downarrow = 1$ , the coefficients  $\zeta_i(\sigma)$  are now given by

$$\begin{aligned}
\zeta_1(\uparrow) &= (-1)^{\alpha+\beta}, & \zeta_2(\uparrow) &= (-1)^\alpha, & \zeta_3(\uparrow) &= (-1)^\beta, \\
\zeta_1(\downarrow) &= (-1)^\alpha, & \zeta_2(\downarrow) &= (-1)^{\alpha+\beta}, & \zeta_3(\downarrow) &= (-1)^\beta,
\end{aligned} \tag{D.10}$$

and the  $\hat{B}_i(j)$  functions, with  $i, j = 1, 2, 3$ , are defined as

$$\hat{B}_i(1) = \hat{B}_{i,-\mathbf{p}+\mathbf{k}+\mathbf{q}}, \quad \hat{B}_i(2) = \hat{B}_{i,\mathbf{p}}, \quad \hat{B}_i(3) = \hat{B}_{i,\mathbf{p}-\mathbf{k}}, \tag{D.11}$$

for  $\sigma = \uparrow$ , and

$$\hat{B}_i(1) = \hat{B}_{i,-\mathbf{p}+\mathbf{k}+\mathbf{q}}, \quad \hat{B}_i(2) = \hat{B}_{i,\mathbf{p}}, \quad \hat{B}_i(3) = \hat{B}_{i,-\mathbf{p}+\mathbf{q}}, \tag{D.12}$$

for  $\sigma = \downarrow$ . The property (D.7) is also satisfied by Eq. (D.9).

# Appendix E

## Square lattice $\pi$ -flux model

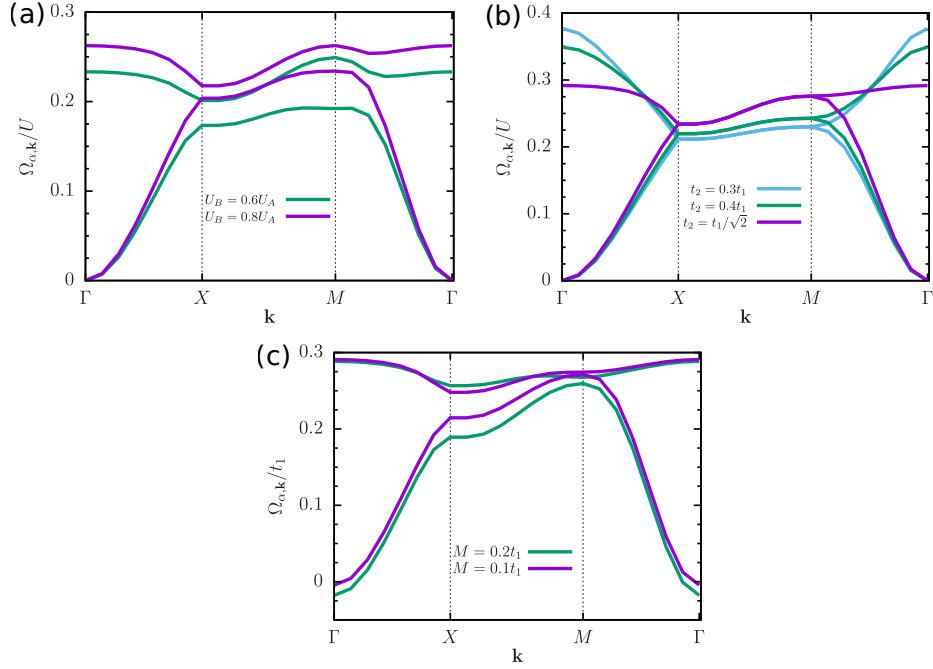
In this Appendix, we present additional results derived within the bosonization formalism for Chern insulators for the flat-band ferromagnetic phase of the topological Hubbard model on a square lattice, whose noninteracting limit is given by the  $\pi$ -flux model, previously studied in Ref. [24]. We follow the lines of Secs. 4.2.2 and 4.2.3 and find that the spin-wave spectra of both square lattice  $\pi$ -flux and Haldane models display the same features. This Appendix is based on Appendix C from Ref. [34].

Figure E.1(a) shows the spin-wave spectrum (4.34) for the nearly flat-band limit of the square lattice  $\pi$ -flux model (which corresponds to the configuration with the next-nearest-neighbor hopping amplitude  $t_2 = t_1/\sqrt{2}$ ) and on-site repulsion energies  $U_B = 0.8 U_A = 0.8 U$  and  $U_B = 0.6 U_A = 0.6 U$ . A comparison with the spin-wave spectrum obtained for the homogeneous case  $U_B = U_A = U$  (see Fig. 4 from Ref. [24] and Fig. E.1(b)) indicates that the energies of the excitations decrease with  $\Delta U$  and an energy gap opens at the border of the first Brillouin zone (the  $X$ - $M$  line). Such features were also found for the Haldane-Hubbard model, see Fig. 4.3. Importantly, for the square lattice  $\pi$ -flux model, the decay rates of the spin-wave excitations vanish.

The effects of a decreasing of the flatness ratio of the noninteracting bands due to the variation of the next-nearest-neighbor hopping amplitude  $t_2$  (see Fig. 3 from Ref. [24] for details) are shown in Fig. E.1(b). Apart from a renormalization of the excitation energies, the spin-wave spectrum (4.34) displays the same features of the nearly flat band limit, similar to the behavior found for the Haldane-Hubbard model, see Fig. 4.5.

Finally, the effects of a finite staggered on-site energy  $M$  are presented in Fig. E.1(c). Since the kinetic contribution  $\bar{\omega}_{\mathbf{q}}^{\alpha,\alpha}$  is quite small, it is not considered. In addition to open an energy gap at the first Brillouin zone border, a finite  $M$  also decreases the lower branch energies in the vicinity of the  $\Gamma$  point, which indicates an instability of the flat-band ferromagnetic phase, see also Fig. 4.6(a).

As discussed in Sec. 6, the instability of the flat-band ferromagnetic phase in the presence of a finite staggered on-site energy  $M$  might be an artifact of the bosonization



**Figure E.1:** Spin-wave excitation spectra (4.34) for the flat-band ferromagnetic phase of the square lattice  $\pi$ -flux model (see Ref. [24] for details): (a) Next-nearest-neighbor hopping amplitudes  $t_2 = 1/\sqrt{2}$  and on-site repulsion energy  $U_B = 0.8U_A = 0.8U$  (magenta) and  $U_B = 0.6U_A = 0.6U$  (green); (b)  $U_A = U_B = U$  and  $t_2 = 1/\sqrt{2}$  (magenta), 0.4 (green), and  $0.3t_1$  (blue); (c)  $t_2 = 1/\sqrt{2}$ ,  $U_A = U_B = U$ , and staggered on-site energy  $M = 0.1$  (magenta) and  $0.2t_1$  (green).

formalism related to the kinetic contribution (4.21). Although it is not clear yet how to properly include in the effective boson model (4.27) the explicitly effects of the dispersion of the noninteracting bands, we check whether a modification of the boson operators (4.11) definition could restore the Goldstone mode. In the following, we briefly summarize such a possible procedure and apply it for the square lattice  $\pi$ -flux model.

The definition of the boson operators (4.11) is based on the linear combination (4.14) of the projected spin operators  $\bar{S}_{\mathbf{q}, A/B}$ . Since a finite  $M$  introduces an offset in the energies of the sites associated with the sublattices  $A$  and  $B$ , instead of Eq. (4.14), one should consider the generalized form

$$\bar{S}_{\mathbf{q}, 0}^{\pm} = \frac{\sqrt{2}}{2} (\cos(\eta)\bar{S}_{\mathbf{q}, A}^{\pm} + \sin(\eta)\bar{S}_{\mathbf{q}, B}^{\pm}), \quad (\text{E.1})$$

$$\bar{S}_{\mathbf{q}, 1}^{\pm} = \frac{\sqrt{2}}{2} (\sin(\eta)\bar{S}_{\mathbf{q}, A}^{\pm} - \cos(\eta)\bar{S}_{\mathbf{q}, B}^{\pm}),$$

where the linear combination (4.14) can be obtained by choosing the parameter  $\eta = \pi/4$ . In this case, the expansion of the  $F_{\alpha\beta, \mathbf{q}}^2$  function (4.15) in terms of the coefficients (3.10)

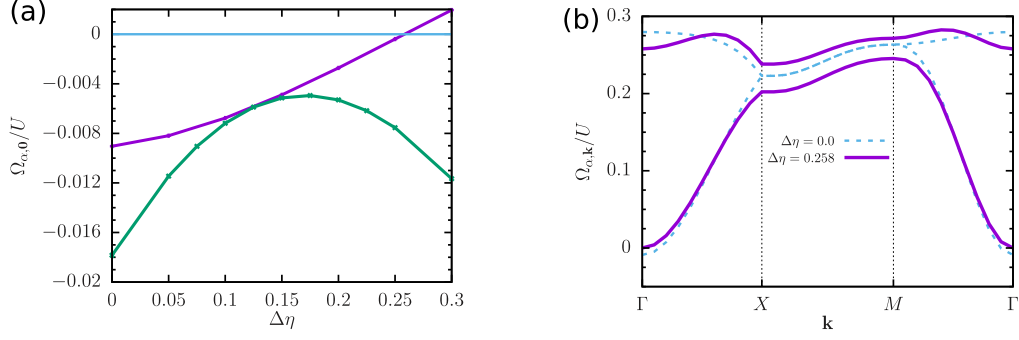


**Figure E.2:** (a) The energy of the Goldstone mode for the square lattice  $\pi$ -flux model with one-site staggered energy  $M = 0.2 t_1$  in terms of  $\Delta\eta = \eta - \pi/4$  determined with the dispersion relations (4.34) (solid green line) and (4.35) (solid magenta line). (b) Dispersion relation (4.35) for  $\Delta\eta = 0$  (dashed blue line) and  $\Delta\eta = 0.258$  (solid magenta line).

now reads

$$F_{\alpha\alpha,\mathbf{q}}^2 = \frac{1}{4} \sum_{\mathbf{k}} [1 + \hat{B}_{3\mathbf{k}} \hat{B}_{3\mathbf{k}-\mathbf{q}}] - (-1)^\alpha \frac{\cos(2\eta)}{4} [\hat{B}_{3\mathbf{k}} + \hat{B}_{3\mathbf{k}-\mathbf{q}}] + (-1)^\alpha \frac{\sin(2\eta)}{4} [\hat{B}_{1\mathbf{k}} \hat{B}_{1\mathbf{k}-\mathbf{q}} + \hat{B}_{2\mathbf{k}} \hat{B}_{2\mathbf{k}-\mathbf{q}}], \quad (\text{E.2})$$

$$F_{\alpha\beta,\mathbf{q}}^2 = \sum_{\mathbf{k}} -\frac{\sin(2\eta)}{4} [\hat{B}_{3\mathbf{k}} + \hat{B}_{3\mathbf{k}-\mathbf{q}}] - \frac{\cos(2\eta)}{4} [\hat{B}_{1\mathbf{k}} \hat{B}_{1\mathbf{k}-\mathbf{q}} + \hat{B}_{2\mathbf{k}} \hat{B}_{2\mathbf{k}-\mathbf{q}}] - (-1)^\alpha \frac{i}{4} [\hat{B}_{2\mathbf{k}} \hat{B}_{1\mathbf{k}-\mathbf{q}} - \hat{B}_{1\mathbf{k}} \hat{B}_{2\mathbf{k}-\mathbf{q}}], \quad (\text{E.3})$$

with  $\alpha \neq \beta$ , and the  $g_\alpha(\mathbf{p}, \mathbf{q})$  function (4.16) is now given by

$$g_\alpha(\mathbf{p}, \mathbf{q}) = G_A(\mathbf{p}, \mathbf{q}) [\cos(\eta)(1 - \alpha) + \alpha \sin(\eta)] + G_B(\mathbf{p}, \mathbf{q}) [\sin(\eta)(1 - \alpha) - \alpha \cos(\eta)], \quad (\text{E.4})$$

with the  $G_a(\mathbf{p}, \mathbf{q})$  function defined by Eq. (4.8). Eqs. (E.2) and (E.4) imply that the expansion (B.23) and (B.24) of the  $\mathcal{G}_{\alpha\beta\alpha\sigma}(\mathbf{k}, \mathbf{q})$  function in terms of the coefficients (3.10) is also modified. Importantly, the modified  $F_{\alpha\beta,\mathbf{q}}^2$  function (E.2) with  $\eta \neq \pi/4$  implies that the condition (4.29) is no longer valid for the square lattice  $\pi$ -flux model. Figure E.2(a) shows the energy of the Goldstone mode in terms of  $\Delta\eta = \eta - \pi/4$  determined with both dispersion relations (4.34) and (4.35) for on-site staggered energy  $M = 0.2 t_1$ . One notices that it is possible to find a parameter  $\eta$  such that the Goldstone mode is restored only if the coefficients  $\epsilon_{\mathbf{q}}^{01}$  and  $\epsilon_{\mathbf{q}}^{10}$  [Eq. (4.25)] are neglected. The spin-wave spectrum (4.35) for optimal  $\Delta\eta = 0.258$  is display in Fig. E.2(b).

# Appendix F

## Chern number of the magnon bands

Here, we briefly describe how we calculated the Chern numbers for the spin-wave bands. This Appendix is based on the Appendix C from Ref. [35].

The procedure consists in casting the effective bosonic Hamiltonian, either Eq. (4.28) or Eq. (5.14), into the Pauli Matrix representation (see Sec.3.1.1), that is,

$$\bar{H}_{U,B}^{(2)} = \sum_{\mathbf{q}} \Phi_{\mathbf{q}}^\dagger \tilde{h}_{\mathbf{q}} \Phi_{\mathbf{q}}, \quad (\text{F.1})$$

where the two-component spinor  $\Phi_{\mathbf{k}}$  is defined as

$$\Phi_{\mathbf{q}} = (b_{0,\mathbf{q}} \ b_{1,\mathbf{q}})^T \quad (\text{F.2})$$

and the  $2 \times 2$  matrix  $\tilde{h}_{\mathbf{q}}$  assumes the form

$$\tilde{h}_{\mathbf{q}} = \tilde{B}_{0,\mathbf{q}} \tau_0 + \sum_{\mu=1}^3 \tilde{B}_{\mu,\mathbf{q}} \tau_{\mu}, \quad (\text{F.3})$$

with  $\tau_0$  being the identity matrix and  $\tau_{\mu}$  being a Pauli matrix. In this form, the coefficients

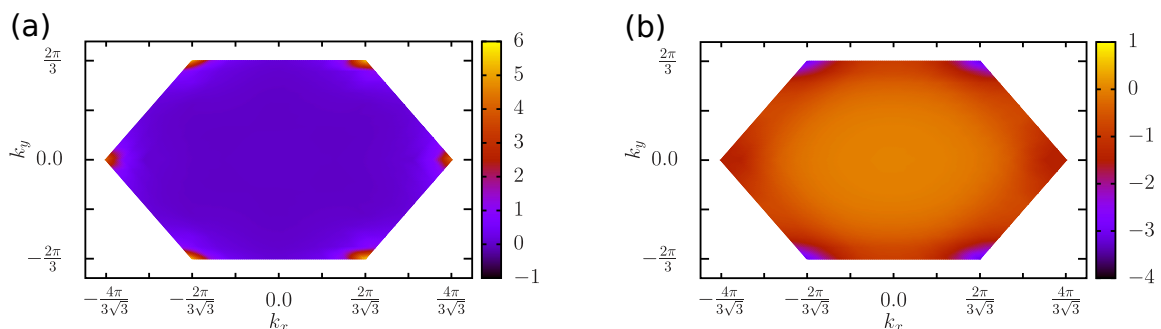


**Figure F.1:** Contour plot of the Berry curvature functions of the lower spin-wave band for the (a) ML and (b) SL excitations, at nearly flat-band limit and on-site Hubbard repulsion energies  $U = U_A = U_B$ .

$\tilde{B}_{\mu,\mathbf{q}}$  are related to the coefficients  $\epsilon_{\mathbf{q}}^{\alpha\beta}$  of Eqs. (4.28) or (5.14), i.e.,

$$\begin{aligned}\tilde{B}_{0,\mathbf{q}} &= \frac{1}{2}(\epsilon_{\mathbf{q}}^{00} + \epsilon_{\mathbf{q}}^{11}) & \tilde{B}_{1,\mathbf{q}} &= \frac{1}{2}(\epsilon_{\mathbf{q}}^{01} + \epsilon_{\mathbf{q}}^{10}) \\ \tilde{B}_{2,\mathbf{q}} &= \frac{1}{2i}(\epsilon_{\mathbf{q}}^{01} - \epsilon_{\mathbf{q}}^{10}) & \tilde{B}_{3,\mathbf{q}} &= \frac{1}{2}(\epsilon_{\mathbf{q}}^{00} - \epsilon_{\mathbf{q}}^{11}).\end{aligned}\tag{F.4}$$

An important point here is that the assumption  $\epsilon_{\mathbf{q}}^{01} = (\epsilon_{\mathbf{q}}^{10})^*$  had to be made. This holds true only for the SL excitations (5.4), but **not** for the ML excitations (5.9) or for the correlated Chern insulator. This fact might have consequences on the results found below. The Chern numbers follow from the use of Eq.(3.15), with the appropriate normalized coefficients  $\hat{\mathbf{B}}_{\mathbf{k}} \rightarrow \tilde{\mathbf{B}}_{\mathbf{k}}/|\tilde{\mathbf{B}}_{\mathbf{k}}|$ , and disconsidering the spin degree of freedom. The Berry curvature, which is defined as one-half of the integrand of Eq. (3.15), for the lower spin-wave bands of the correlated  $Z_2$  topological insulator at the nearly flat band limit (3.18) with  $U = U_A = U_B$  is plotted in Figure F.1. We show the Berry curvature for both ML and SL excitations. For the Chern insulator, the Berry curvature vanishes for any configuration of  $U_A \neq U_B$  at the flat band limit (not shown), thus, yielding  $C_n = 0$  for both upper and lower bands.